12-2012

Carbon nanomaterial based vapor sensors.

Silpa Kona
University of Louisville

CARBON NANOMATERIAL BASED VAPOR SENSORS

By

Silpa Kona
B.Tech., Gokaraju Rangaraju Institute of Engineering and Technology, 2005
M.S., University of Louisville, 2007

A Dissertation
Submitted to the Faculty of the
J.B.Speed School of Engineering of the University of Louisville
in Partial Fulfillment of the Requirements
for the Degree of

Doctor of Philosophy

Department of Electrical and Computer Engineering
University of Louisville
Louisville, Kentucky

December 2012

CARBON NANOMATERIAL BASED VAPOR SENSORS

By

Silpa Kona
M.S. Electrical and Computer Engineering, University of Louisville
Louisville, Kentucky, 40208

A Dissertation Approved on

November 28, 2012

by the following Dissertation Committee:

Dr. Cindy K. Harnett (Dissertation Director)

Dr. John Naber

Dr. Shamus McNamara

Dr. Palaniappan Sethu

Dr. Frank Zamborini

DEDICATED TO

KIRAN

ACKNOWLEDGEMENTS

I would like to acknowledge all of those people who helped make this dissertation possible.

First, I wish to thank my advisor, Dr. Cindy K Harnett, for all her guidance, encouragement and infinite patience and for going above and beyond an advisor's ability to provide emotional support during my PhD. Dr C, I cannot thank you enough.

I would like to acknowledge and thank my committee members Dr. John Naber, Dr.Shamus McNamara, Dr. Palaniappan Sethu and Dr. Frank Zamborini for their very helpful insights, comments and suggestions at my proposal meeting.

I thank from the bottom of my heart, my parents Sasi Kumar and Sarala, for their thoroughly biased opinion that I truly am the best. This stage in my life would not have been possible without their being my pillars of support all through.

Collaboration is the root of success in any research environment and there have been several colleagues who have been amazing at discussing ideas and sharing their knowledge during the course of my PhD. Dr.Tanesh Bansal, Dr.Kapila Hewaparakrama, Thomas J Roussel, Kasun Fernando and Cory Franklin have all been extremely helpful. I thank them and appreciate the time they spent discussing their ideas with me. I also thank Dr.Jacek Jasinski and the Conn Center for Renewable Energy for their help in characterizing my graphene samples.

I would also like to acknowledge and thank University of Louisville for awarding me the Grosscurth fellowship during my PhD and the Dissertation completion award for doctoral students. I also acknowledge and thank the National Science Foundation for the funding they have provided for my research.

ABSTRACT

CARBON NANOMATERIAL BASED VAPOR SENSORS

Silpa Kona

November 28, 2012

The discovery of carbon nanotubes and subsequently graphene has led to an interest in carbon materials as sensing elements due to their unique properties. Graphene is a 2-dimensional material that has a large surface area that can be exposed to surface adsorbates from a target gas. This enables studies on the interaction of gas molecules with the graphene surface and subsequent changes in its properties. Graphene also exhibits high conductivity and low noise and has low crystal defects. Due to its high electron mobility at room temperature, graphene exhibits high sensitivity (in tune of detecting ppm) which is a required trait in environmental and industrial sensing applications, making graphene a good candidate for sensors.

Several models of sensors based on graphene as sensing element have been put forth previously based on high-resolution lithographic techniques and for individual electrode attachment to the sensing film with e-beam lithography. These techniques can produce small numbers of devices that explore the limits of molecular scale sensing, but the methods are currently impractical for large scale production of low cost sensors. The work presented here counters this labor-intensive process and puts forth a practical low-cost sensor. Graphene sheets grown using chemical vapor deposition are transferred onto

an acrylic chip designed for gas sensing. The working principle of the sensor is the electrical conductivity change exhibited by the graphene when molecules adsorb onto the material while the sensor chip is exposed to the target gas in a controlled environment. We present our graphene based sensor with the focus on designing small, cost effective and reliable sensors with high sensitivity towards the target gas, detailing the assembly of graphene/acrylic based devices, their characterization and investigation of their performance as resistive chemical sensors using different substrates as graphene supports.

TABLE OF CONTENTS

PAGE

LIST OF FIGURES

FIGURE PAGE

CHAPTER I

INTRODUCTION

1.1 Outline

The discovery of carbon nanotubes and subsequently graphene has led to an interest in carbon materials as sensing elements due to their unique properties. These nanomaterials have a large surface area that can be exposed to surface adsorbates from a target gas. This enables studies on the interaction of gas molecules with their surface and the subsequent changes in their properties. Among the carbon nanomaterials, Graphene is especially attractive as it exhibits high conductivity and low noise and has low crystal defects. Due to its high electron mobility at room temperature, it has high sensitivity (in tune of detecting ppm) which is a required trait in environmental and industrial sensing applications, making graphene a good candidate for sensors. In spite of several models of sensors based on graphene as sensing element have been put forth previously, they adopt manufacturing techniques using high-resolution lithography and individual electrode attachment to the sensing film with e-beam lithography. These techniques can produce small numbers of devices that explore the limits of molecular scale sensing, but the methods are currently impractical for large scale production of low cost sensors. This dissertation seeks to address some of these limitations and presents carbon based nanomaterials (prominently graphene) as an efficient sensing element. An introduction to

gas sensors in general, the current trends and advances in gas sensor technology, the limitations of existing manufacturing techniques are discussed in the current Chapter (I). The succeeding Chapter (II) discusses an approach to grow carbon nanomaterials in-situ for on-device integration of vapor sensors, and the limitations encountered by such an approach. It also lays a background for graphene as a sensing element. Chapter III discusses the synthesis and characterization of graphene. It describes graphene synthesis using chemical vapor deposition and the transfer technique designed for the gas sensing device. Chapter IV discusses the device design, cost calculation and the experiment setup. The working principle of the sensor is discussed – change in the electrical conductivity of graphene when molecules adsorb onto the material while the sensor chip is exposed to the target gas in a controlled environment. Results from this research work are discussed in Chapter V with the conclusions and future directions for the research laid out in Chapter VI

1.2 Introduction to sensors

The International Union of Pure and Applied Chemistry defines a chemical sensor as (1) -

> *"A device that transforms chemical information, ranging from the concentration of a specific sample component to total composition analysis, into an analytically useful signal. The chemical information, mentioned above, may originate from a chemical reaction of the analyte or from a physical property of the system investigated"*

Chemical sensors are primarily used for controlling/monitoring of pollutant levels in the atmosphere, for monitoring and process control (safety) in the industrial sector, to track hazardous materials and more recently to improve diagnostics in medical applications. The composition of clean dry air near sea level consists mostly of Nitrogen (78.09%),

Oxygen (20.94%), Argon (0.93%) and miniscule amounts of Carbon Dioxide, Helium, Hydrogen, Methane, and Nitrous Oxide among others (2). Any change in the composition of air, or an increase in toxic/harmful gases affects the quality of life and also trips the ecological balance in the environment at the extreme end of the scale, making a system with efficient gas sensing capability a much required entity. A survey carried out in 2002 estimated the global sensor market to reach an estimated $44.46 billion by the year 2006 (3). Of this estimate, a reported $ 2.24 billion is taken up by gas sensor systems which include both gas metering and gas sensors. From this data, an estimated growth rate of 4-6% was projected and met by the year 2010. Figure 1.1 shows a pie chart depicting the global sensor sale market based on the actual sales figures from the year 2010. Owing to the tremendous interest in incorporating new and emerging materials into the existing technology, and the steady growth of gross domestic product (GDP) in developing countries, and to an invariable increase in safety consciousness globally, the gas sensor market is estimated to grow steadily into the next decade (4).

Sensors or sensing apparatus play a major part in enriching and also filling in a protective role in our day to day life (5) (6). A list of applications that sensors find in our everyday life is shown in Table 1 (7). The current work deals with the very pertinent field of gas sensing, with this chapter giving a brief history of sensors and progressing to the existing sensor technology and current and emerging markets with a focus on nanomaterials as the sensing element.

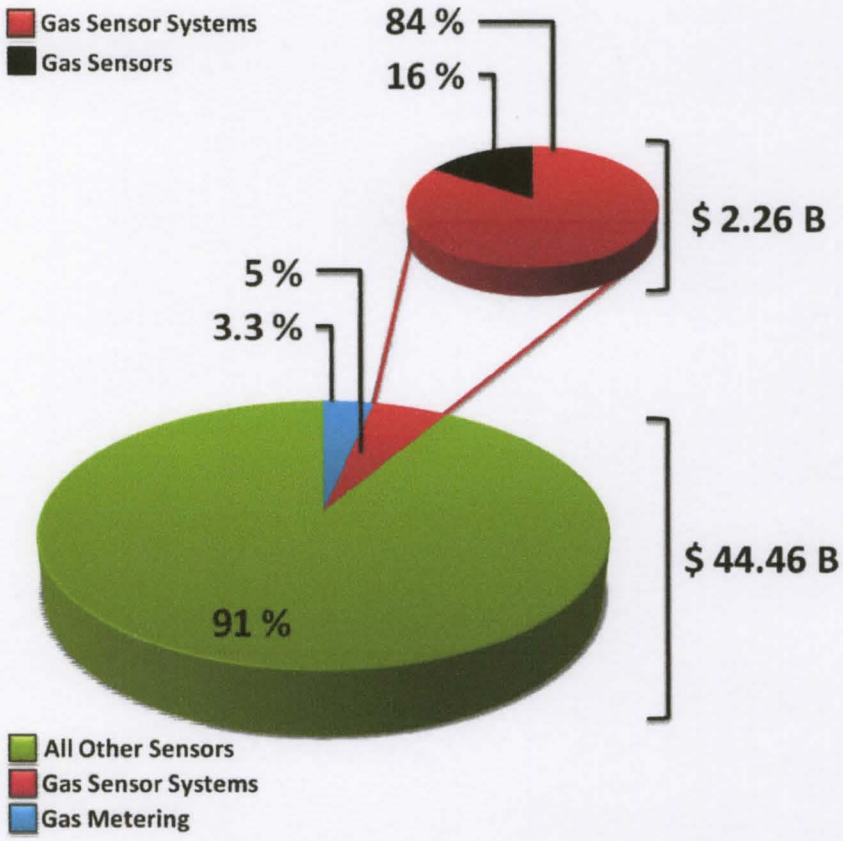

Figure 1.1: Pie chart depicting global sensor sale

One of the earliest gas detectors (Davy Lamp) was introduced in 1816 at a Royal Society meeting by Sir Humphry Davy (8), which was capable of detecting carbon dioxide, oxygen and methane. The years between 1925-1927 at The Institute of Physical and Chemical Research in Japan saw the conception of an interferometer that was capable of detecting the presence of methane and other combustible vapors using the principle of light diffraction in air, giving a range of the gas concentrations present in the air (9).

APPLICATIONS
Automobiles ▪ Car ventilation control ▪ Filter control ▪ Gasoline vapor detection ▪ Alcohol breath tests
Safety ▪ Fire detection ▪ Leak detection ▪ Toxic / flammable / explosive gas detectors ▪ Boiler control ▪ Personal gas monitor
Indoor air quality ▪ Air purifiers ▪ Ventilation control ▪ Cooking control
Environmental control ▪ Weather stations ▪ Pollution monitoring
Food ▪ Food quality control ▪ Process control ▪ Packaging quality control (off-odors)
Industrial production ▪ Fermentation control ▪ Process control
Medicine ▪ Breath analysis ▪ Disease detection

Table 1: Examples of sensors in everyday life

1926 saw the emergence of a catalytic combustion sensor which employs a hot wire catalytic platinum filament that oxidizes any flammable gas vapors that it comes in contact with, leading to an increase in the temperature of the filament. This temperature increase leads to an increase in the electrical resistance of the wire, which is detected by a Wheatstone bridge (10) (11). This concept is still relevant in the present day and age of resistive chemical sensors where, this technology is being used to detect combustible

gases. The schematics and the prototypes of these early gas sensing devices are shown in Figure 1.2, with Figure 2(a) showing a Davy safety lamp (12) .

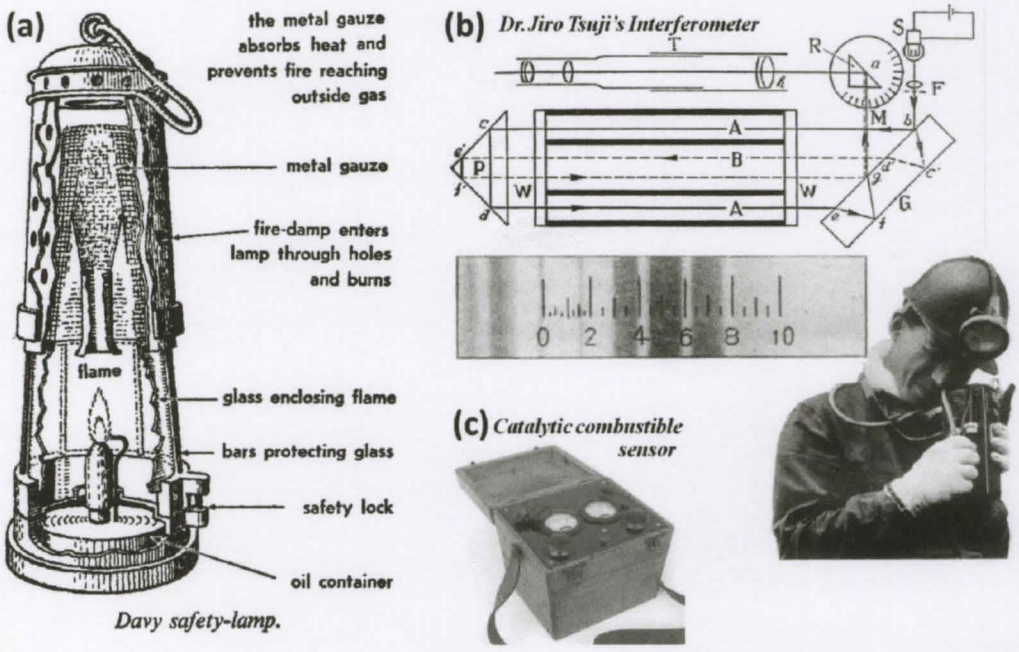

Figure 1.2: (a) A schematic showing the working of a Davy safety-lamp (12) (b) Dr.Tsuji's Interferometer (9) (c) An early prototype of a catalytic combustible

The area of resistive electrochemical sensors counts metal oxide sensors among its most successful progeny, as they have been in use in for the past 60 years for industrial safety and monitoring. The first reports on the adsorption/desorption of gas molecules on the surface of a zinc oxide film changing its conductivity appeared in 1962 (13).Since then, it has been clearly shown that this materials sensitivity to the presence of gas can be as low as parts per billion (ppb) (14) (15), thus cementing metal oxide semiconductor based gas sensing as inexpensive, robust technology. In spite of their overwhelming success, metal oxide sensors have several drawbacks and limitations. Their non-linear logarithmic response to a linear increase in gas concentration is an undesirable trait when being used

in sensitive environments. Also, they have been known to be non-specific, leading to an inaccurate data pertaining to the type of gas being detected. In spite of their robustness and durability, their disadvantages include their inability to provide reliable data, limitations in their manufacturing techniques, noisy signal outputs and sensitivity issues which are being addressed by nano-engineering the sensing materials.

A sensor has to meet certain important measurement criteria like stability, sensitivity, cross sensitivity and acceptable sensor response times for its performance to be characterized. These are defined in (16) as

Sensitivity is a change of measured signal per analyte concentration unit i.e., the slope of the calibration graph where, this parameter is sometimes confused with the detection limit.

Selectivity: Refers to characteristics that determine whether a sensor can respond selectively to a group of analytes or even specifically to a single analyte.

Detection limit: The lowest concentration of the analyte that can be detected by the sensor under given conditions, particularly at a given temperature.

Dynamic Range: The analyte concentration range between the detection limit and the highest limiting concentration.

Linearity: The relative deviation of an experimentally determined calibration graph from an ideal straight line.

Resolution: The lowest concentration difference that can be distinguished by a sensor

Response time: The time required by a sensor to respond to a step concentration change from zero to a certain concentration value

Recovery time: The time it takes for a sensor signal to return to its initial value after a step concentration change from a certain value to zero

Working temperature: Usually the temperature that corresponds to maximum sensitivity

Hysterisis: The maximum difference in output when the value is approached with an increasing and a decreasing analyte concentration range

Life cycle: The period of time over which the sensor will continually operate

Stability: The ability of a sensor to provide reproducible results for a certain period of time. This includes retaining the sensitivity, selectivity, response and recovery time.

A chemical sensor should ideally have a high dynamic range, sensitivity, selectivity and stability while showing a low detection limit and small response times. But, as in the real world dealing with physical sensing elements that are prone to chemical degradation and/or mechanical failures, a sensor meeting all of the above standards is extremely rare. Depending on the specific application, sensors are designed and engineered to meet the criteria that the situation dictates-are a priority. For example, when detecting highly flammable materials or explosives, the most important features of the sensor being used are to be low detection limits (ppb) and low response times. Whereas, in slightly less-risk applications like sensors that monitor the pollutant levels in air (environmental sensors) during say, rush hour in a major city, it is acceptable to have sensors that have slightly slower response times.

1.3 Nanomaterials for resistive chemical sensing

The past few decades has seen an increasing rise in demand for sensors that are accurate, portable, inexpensive to manufacture and are reliable in the long run. Nanomaterials are gaining ground as the most attractive sensing elements owing to their high-surface area to volume ratio that leads to smaller sensor footprints and faster response times. Nanomaterial based gas sensors are also known to operate at lower temperatures. Taking advantage of newer nanofabrication/engineering techniques has opened up new avenues for sensor manufacturing.

1.3.1 Resistive carbon based nanomaterials for electrochemical gas sensing

Among the current carbon based nanomaterials, the most commonly used chemically sensitive materials are carbon black, carbon nanotubes and graphene. Where, most prominently, a polymer-carbon black composite has garnered immense interest as an electronic nose. The e-nose attempts to mimic the mammalian olfactory sense in its response to odors or vapors. Polymer-carbon black composites in these e-noses are essentially a mix of carbon black and polymer in a volatile solvent which is deposited on a substrate. Once the composite film forms between the metal electrodes, arrays are built from these chemi-resistors which serve as the electronic nose, sampling a variety of vapors or odors (17). Sensors built from these carbon black arrays have shown good sensitivity to a large number of vapors (18). Among the most important applications that such gas sensors find, sensing of organic vapors like methanol, ethanol, toluene and

benzene for industrial or laboratory safety is on the rise. Figure 1.3(a) shows an e-nose based on a carbon black-polymer composite (19).

In the recent past, carbon nanotubes that are a class of one-dimensional carbon based nanomaterial have also found to be efficient as sensing elements. Their dimensionality and high surface area to volume ratio facilitates greater adsorption of gas molecules and therefore a greater modulation of their conductance (resistance) in the presence of these adsorbates. Carbon nanotubes are extremely sensitive to adsorbates or dopants from either electron-donating or electron-accepting gas molecules. When exposed to these gases, the generally p-type carbon nanotubes exhibit a change in the density of their bulk charge carriers (holes – in ptype) which translates into a change in the conductance or resistance of the nanotubes. Figure 1.3(b) shows a carbon nanotube based field effect transistor- gas sensing device (20).

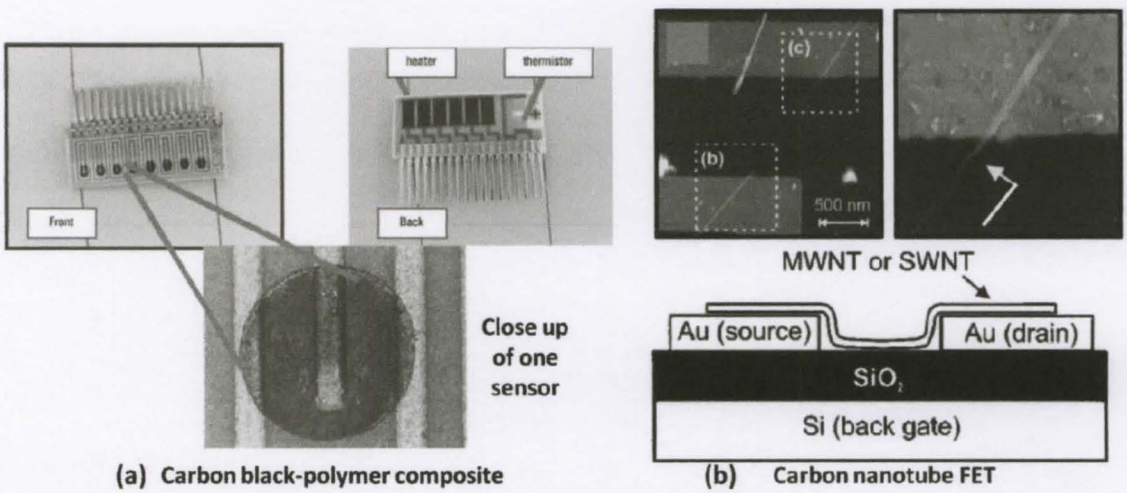

Figure 1.3: (a) An electronic nose comprising of carbon black-polymer composite array (20) (b) Multi-single walled carbon nanotube based field effect transistor

1.3.2 Limitations in current technology

Existing sensor designs, which show high performance characteristics (utilizing both traditional and nontraditional sensing elements), have several limitations that prevent them from being successful. Most of the designs involve high-resolution lithographic techniques which are expensive and tedious. Also, to be considered is the delicate process of individual attachment of electrodes to the sensing material using e-beam lithography. Also, the difficulty encountered in maneuvering a single carbon nanotube onto the desired location (FET) (20) is high, bringing the throughput for sensor manufacturing down drastically. These sensor manufacturing processes are therefore impractical for large scale production of low cost sensors. Additionally, most existing sensors (if not all) are designed to operate at elevated temperatures, thus limiting their practicality. Some of these limitations in sensor manufacturing techniques can be overcome by introducing graphene as the resistive chemical sensing element.

CHAPTER II

INCORPORATING NANOMATERIALS INTO DEVICES AS SENSOR ELEMENTS

2.1 In-device growth of nanomaterials

In spite of current literature expounding on using carbon based nanomaterials for resistive chemical sensing, there are certain limitations in their current manufacturing techniques. They involve high resolution lithographic techniques that are expensive and produce only a small number of devices that explore the limits of molecular scale sensing (21), making them impractical for large scale production of low cost sensors. One possible approach would be to synthesize the nanomaterial in-device, using a small scale microreactor (as opposed to macro scale reactors), thus cutting down the large overhead costs involved in running these equipment – and essentially bringing down the production cost of each individual sensor device.

2.1.1 Introduction to carbon nanotubes

Carbon nanotubes (CNTs) and graphene are very closely related in structure, where, a CNT can be considered to be a seamlessly rolled up sheet of graphene. Figure 2.1 shows the electronic structure of a CNT that is dependent on the chirality of the tube. Here, armchair, zigzag and chiral formats are seen as a function of the tube axis. Carbon

nanotubes are extremely sensitive to any changes in the environment they are exposed to, and hence are ideal as nanoscale sensing elements.

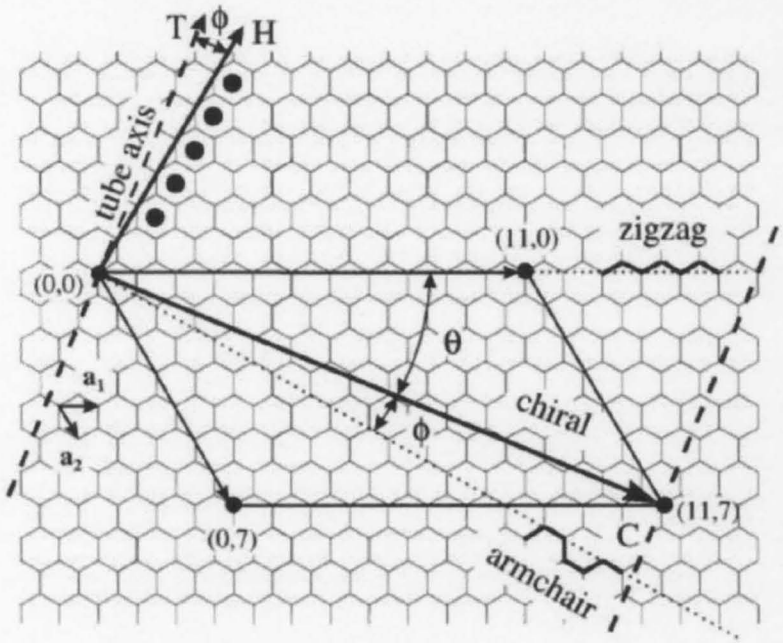

Figure 2.1: Electronic structure of carbon nanotubes (159)

Incorporating carbon nanotubes inside a sensor device by synthesizing them in-situ the device channels at a micro-scale, would greatly reduce the over-head costs involved in running a macro-scale reactor. This approach is described in the next section.

2.2 Microreactor Approach

The last decade has seen an accelerated interest in developing lab-on-chip, μTAS (Micro Total Analysis Systems) that provide a complete platform for material analysis. The most precise definition of microreactors is given as (22):

> "Components and systems that exploit engineered structures, surface features or dimensions that are typically measured in terms of microns (one millionth of a meter) to hundreds or thousands of microns, and that may include microelectronic components as an integral part of the system."

In current day technology, this has metamorphosed to include a wider range of applications and interests. One such being, a scaled down chemical vapor deposition (CVD) process – both for thermal and plasma CVD. Using this approach, controlled growth of carbon nanotubes and carbon thin film deposition inside the micro-channel of fused silica chips to build a gas sensing device has been carried and is described in the succeeding sections

2.2.1 In-device growth of carbon nanomaterial in fused silica chips

Carbon nanotube synthesis at the micro-scale is a very attractive option for in-device growth, as it involves lower precursor volumes and lower overhead costs in running the reactor. The microreactor chamber is essentially a device with micro-scale channels, through which precursor gases flow and undergo decomposition (in excess of 700 ^{o}C for thermal CVD) in the presence of a catalyst. This leads to the growth of carbon nanomaterial lining the walls of the microcapillary channels, essentially forming a film of sensing material.

Thermal chemical vapor deposition is a high temperature process and therefore, for in-device growth of carbon nanotubes/thin films, the substrate material has to be able to withstand high temperatures. Fused silica wafers (Corning 7890 from Sensor Prep Inc.,) are chosen as the substrate material in the work being described currently. Fused

silica is a result of melting synthetically derived SiO_2 and is used in many of the same applications as fused quartz. Fused silica has many attractive properties - high purity (leading to less contamination during catalytic growth of nanomaterial), high chemical resistance, good thermal shock resistance and low thermal expansion coefficient. Their annealing point is 1042 °C and softening point is 1585 °C, both of which are much lower than the thermal decomposition of hydrocarbon gases. Owing to its higher working and melting temperatures, the sensor device is constructed by bonding two fused silica plates, a top plate (with ports) and a base plate (with micro channels), essentially forming an enclosed device for nanomaterial growth. Figure 2.2 shows a schematic of a cross sectional view of a fused silica device with nanomaterial coating the micro-channel surfaces.

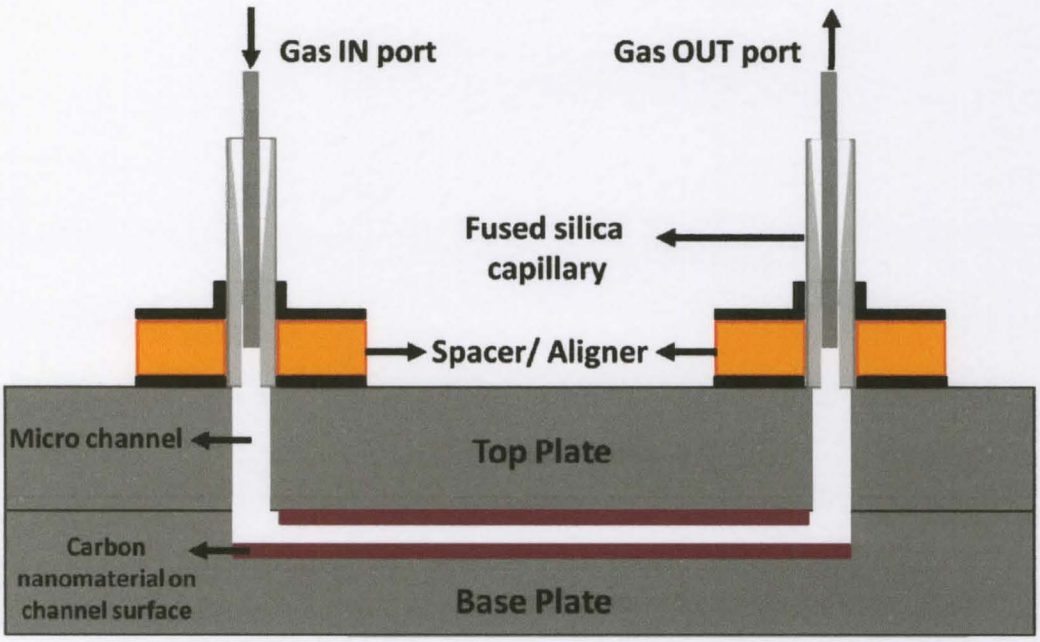

Figure 2.2 Schematic of a cross sectional view of a fused silica chip

The following section describes the etch and bond processes involved in creating these fused silica chips.

2.2.2 Fused silica etch and bond process

Etch Process: Fused silica wafers (Corning 7890 from Sensor Prep Inc.,) are initially cleaned using the glass clean process. This involves immersing them in fresh Nanostrip solution for 10 minutes at 100 ^{o}C in a clean room environment. These wafers are then cascade rinsed for 10 minutes in de-ionized water and spin-rinse dried. The wafers are next transferred to a fused silica boat and a silicon CVD hardmask is applied: with 150nm amorphous Si (LPCVD at 540 ^{o}C) and oven dried at 125 ^{o}C for 10 minutes. Photoresist (S-1827) is applied to the center of the wafer and spun at 3000 rpm for a film thickness of 3 μm. This step is followed by a softbake at 1 minute at 115 ^{o}C on a hotplate. A photomask exposure is carried out and is followed by a developing in MF-312 dish at room temperature for 1 minute with agitation. The wafer is then rinsed in water and run through the spin-rinse dryer. A hard bake resist is carried out next for 30 minutes at 125 ^{o}C in oven.

The hardmask etch is carried out for amorphous silicon in a plasma etching machine. The fused silica HF etch involves immersing the wafer in 49% HF at room temperature. At a typical etch rate of 1.18 microns/minute for the Corning 7890 wafers and an amorphous silicon mask, depths of up to 40 μm can be carried out before mask degradation sets in. The excess etchant can be removed by immersing in water for 1 minute, followed by cascade rinse in DI water for 10 minutes. The wafers are then put in

spin-rinse dryer. The photoresist on the wafer are stripped off using acetone for 30 seconds at room temperature, followed by an Isopropyl alcohol and water rinse.

Organic residue on the cleaned wafer is removed by a glass clean process, followed by a cascade rinse for 5 minutes and running through the spin rinse dryer. In case of amorphous silicon masks, the silicon hardmask is stripped away using 40% NaOH bath at 75 ^{o}C for 30 seconds and cascade rinsed for 10 minutes and then run through the spin-rinse dryer. The wafers at this stage are ready for the prebond clean described below.

Prebond clean: The wafers are put into a fresh bath of Nanostrip for for 15 minutes at 100 ^{o}C, followed by immersing them into a fresh bath of NaOH (40% by weight) for 15 minutes at 75 ^{o}C. These are then sent through a cascade rinse for 10 minutes with deionized water followed by a cycle in the spin rinse dryer.

Cover plates for devices: The wafers are drilled using high-speed (20000-50000 rom) diamond tipped bit and water stream for cooling. The typical diameter for the bores obtained range between 15 mil–1 mm. To remove the debris, the wafers are degreased using a solution of 1 mg/L micro-soap in an ultrasonic bath for 4 hours following which, they are spray rinsed with water and run through the spin-rinse dryer. The wafers at this stage are again subjected to the glass clean process and cascade rinsed with de-ionized water for 10 minutes. A stress relief etch is carried out for 90 seconds in 1% HF at room temperature followed by a cascade rinse for 10 minutes and a cycle through the spin-rinse dryer. This step is followed by a pre-bond clean (described above) following which, they are bonded together.

Chip Bonding: The cleaned wafers are aligned and pre-sealed by pressing them together. A silicon wafer anneal is carried out where, the pre-sealed wafers are subjected to 875 °C temperature for 1 hour and at a ramp rate of 3C/minute, the temperature is raised to 1150 °C and held for 5 hours. A gradual ramp down is carried out to 875 °C and a second cooling down step at -3 °C/ minute to room temperature. Individual chips or devices are then cut apart using a dicing saw. Figure 2.3 shows a schematic of the microfabrication process flow described so far.

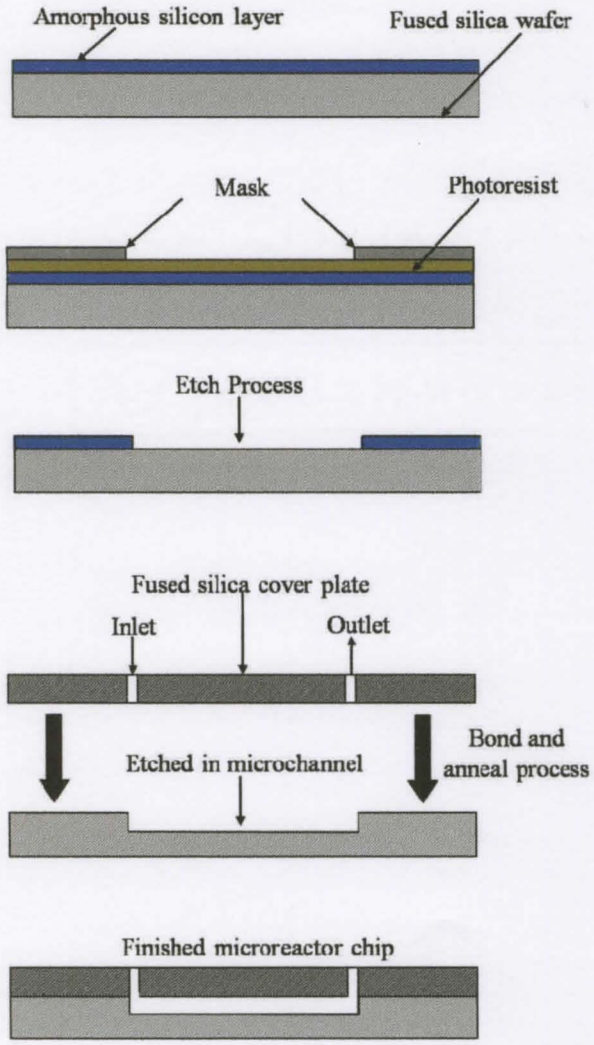

Figure 2.3. Microfabrications process flow for fused silica chip fabrication

Port Bonding: Gas flow channels to the device are fused silica capillary tubing of inner diameters ranging from 150 to 720μm. These micro capillary fused silica tubings are coupled to the fused silica chip using Inner-loks (Polymicro technologies). These are designed for quick contamination free coupling of gas chromatography colums and polyimide coated fused silica tubings. These inner-loks have an excellent thermal expansion match with the gas flow tubing and hence are ideal for the current application of high temperature CVD process on the device.

The gas flow tubing is inserted into the innerlok using a friction fit and is secured using a thin film of epoxy (if needed). The inner-lok is then bonded to the fused silica chip using Aremco 617 cement. This cement is a high temperature, single part water based glass coating and is used to seal porosity in ceramics and in applications to 1450 ^{o}C where hermeticity is required. This cement bonds the innerlok to the fused silica chip and provides a leak proff environment for the nanomaterial synthesis in the micro channels. Figure 2.4 shows a bonded fused silica device with inner-loks.

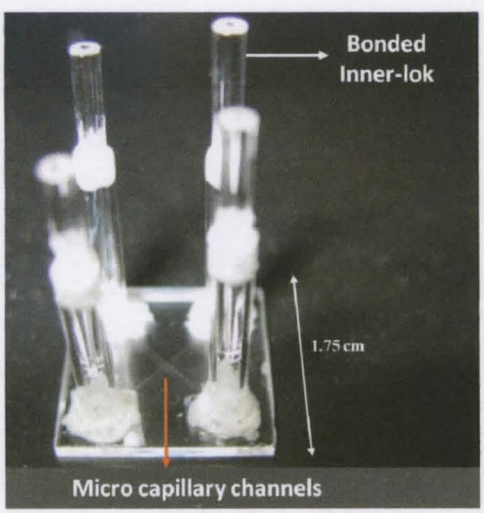

Figure 2.4. Bonded fused silica chip with inner-loks and gas ports

2.2.3 Chemical Vapor Deposition inside fused silica chips

Catalyst for CVD: Using microcapillary tubing that is inserted into the ports bonded on the chip, a catalyst solution is introduced in to the micro channels of the device. This involves mixing Iron (III) nitrate or ferrice nitrate - $Fe(NO_3)_3$ with 2-propanol in a 1:20 ratio and mixing in 5 ml of n-hexane (for a 20 ml catalyst solution). This solution is ultra-sonicated for 3 hours and leads to the formation of iron nanoparticles in the size range of 2-10 nm. This catalyst particle dispersion is piped into the micro channels of the device and set to dry in a nitrogen environment at room temperature.

Experiment setup: Thermal CVD involves high temperatures in excess of 700 ^{o}C to facilitate thermal decomposition of hydrocarbon gases. To radiatively heat the chip, a Senty express kiln capable of reaching temperatures as high 1300 ^{o}C is chosen. Initial experiments using the kiln failed to show carbon deposition on a substrate. As the carbon feedstock in these experiments is gaseous in nature, and has to be supplied with sufficient thermal energy facilitating breakdown, a temperature optimization process was carried out. Figure 2.5 shows a temperature plot showing the Kiln temperature versus a thermocouple that was placed in close proximity to the fused silica device in the kiln.

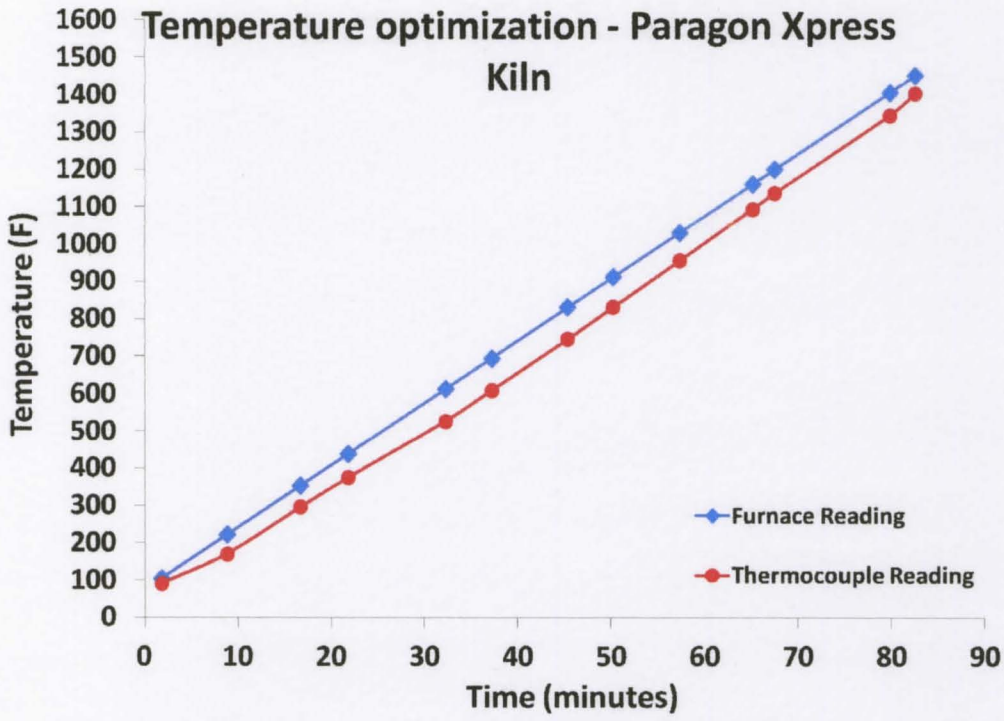

Figure 2.5. Curves comparing temperatures recorded by a mounted thermocouple (furnace reading) versus the temperature at the substrate surface

This shows a temperature difference of close to 70 °C at the surface of the device versus a mounted thermocouple on the kiln. As the thermal decomposition temperature of methane (temperature at which methane chemically decomposes to produce carbon and hydrogen species) is to be reached, any offset from this will lead to the precursor gases leaving the microreactor chamber without breaking down.

Additionally, further experiments with the compensated temperature offset failed to yield growth in the fused silica devices. To further optimize the CVD recipe, detailed and exhaustive calculations were carried out to determine the gas flow rates and the decomposed precursor species-dwell times in the reactor chamber. These dwell time calculations are shown in Figure 2.6

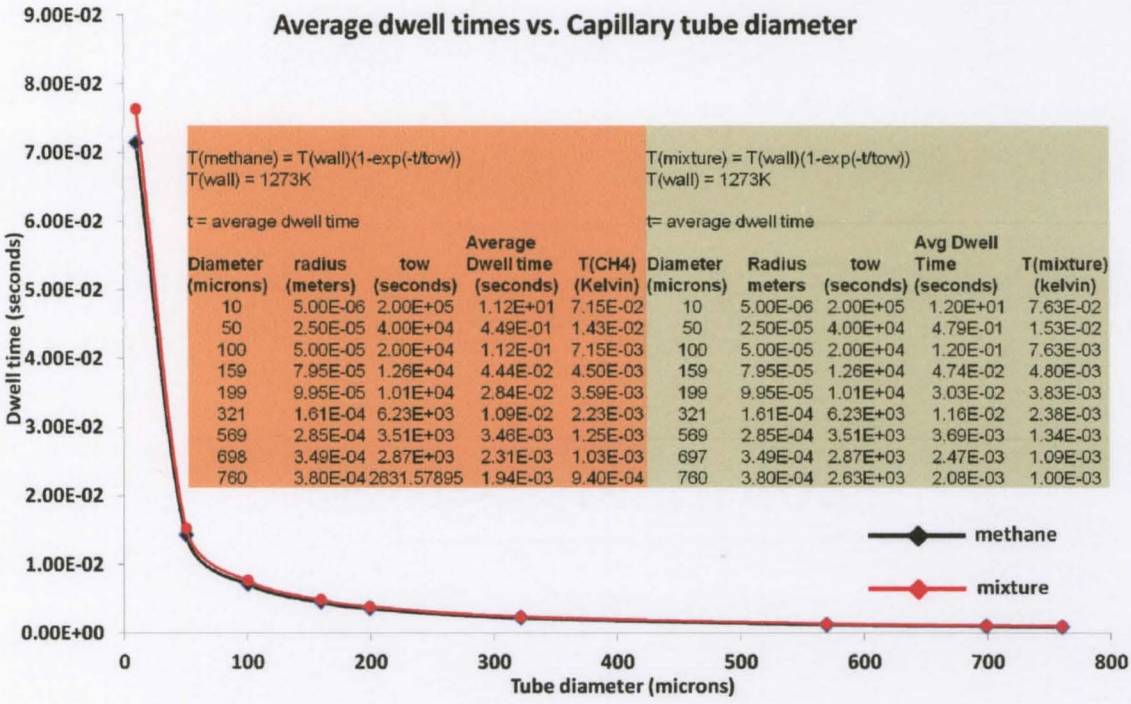

T(methane) = T(wall)(1-exp(-t/tow))
T(wall) = 1273K

t = average dwell time

Diameter (microns)	radius (meters)	tow (seconds)	Average Dwell time (seconds)	T(CH4) (Kelvin)
10	5.00E-06	2.00E+05	1.12E+01	7.15E-02
50	2.50E-05	4.00E+04	4.49E-01	1.43E-02
100	5.00E-05	2.00E+04	1.12E-01	7.15E-03
159	7.95E-05	1.26E+04	4.44E-02	4.50E-03
199	9.95E-05	1.01E+04	2.84E-02	3.59E-03
321	1.61E-04	6.23E+03	1.09E-02	2.23E-03
569	2.85E-04	3.51E+03	3.46E-03	1.25E-03
698	3.49E-04	2.87E+03	2.31E-03	1.03E-03
760	3.80E-04	2631.57895	1.94E-03	9.40E-04

T(mixture) = T(wall)(1-exp(-t/tow))
T(wall) = 1273K

t= average dwell time

Diameter (microns)	Radius meters	tow (seconds)	Avg Dwell Time (seconds)	T(mixture) (kelvin)
10	5.00E-06	2.00E+05	1.20E+01	7.63E-02
50	2.50E-05	4.00E+04	4.79E-01	1.53E-02
100	5.00E-05	2.00E+04	1.20E-01	7.63E-03
159	7.95E-05	1.26E+04	4.74E-02	4.80E-03
199	9.95E-05	1.01E+04	3.03E-02	3.83E-03
321	1.61E-04	6.23E+03	1.16E-02	2.38E-03
569	2.85E-04	3.51E+03	3.69E-03	1.34E-03
697	3.49E-04	2.87E+03	2.47E-03	1.09E-03
760	3.80E-04	2.63E+03	2.08E-03	1.00E-03

Figure 2.6. Dwell time calculations for methane precursor gas and a mixture of (80:20) CH_4:H_2 plotted as a function of capillary tube diameter

As the average dwell time is a function of the tube diameter, the volumetric gas flow rates as a function of the capillary (gas lines) tubing diameters were calculated and tabulated (shown in Figure 2.7). This shows that the number of moles of methane available in the microcapillary tubing (of specific diameters) exceeds the number of moles required for the growth of carbon nanotubes – with the exception of 10μm tubing, eliminating this diameter tubing as a viable substrate for microscale CVD. Optimization of the process is therefore a crucial step during nanomaterial synthesis using catalytic thermal CVD process.

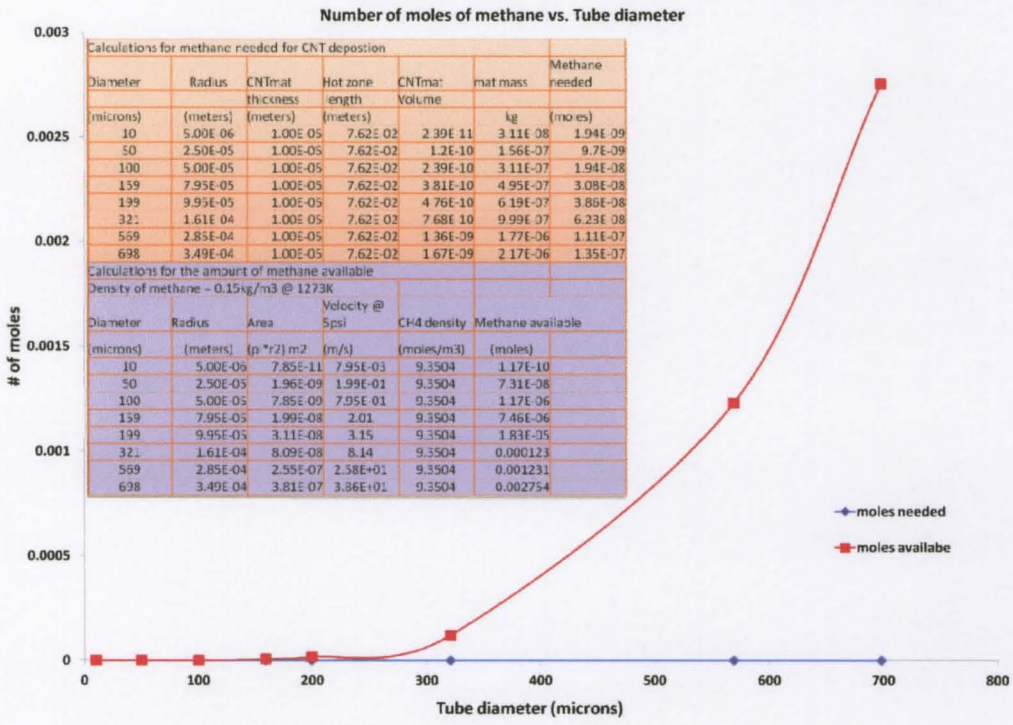

Calculations for methane needed for CNT depostion

Diameter	Radius	CNTmat thickness	Hot zone length	CNTmat Volume	mat mass	Methane needed
(microns)	(meters)	(meters)	(meters)		kg	(moles)
10	5.00E-06	1.00E-05	7.62E-02	2.39E-11	3.11E-08	1.94E-09
50	2.50E-05	1.00E-05	7.62E-02	1.2E-10	1.56E-07	9.7E-09
100	5.00E-05	1.00E-05	7.62E-02	2.39E-10	3.11E-07	1.94E-08
159	7.95E-05	1.00E-05	7.62E-02	3.81E-10	4.95E-07	3.08E-08
199	9.95E-05	1.00E-05	7.62E-02	4.76E-10	6.19E-07	3.86E-08
321	1.61E-04	1.00E-05	7.62E-02	7.68E-10	9.99E-07	6.23E-08
559	2.85E-04	1.00E-05	7.62E-02	1.36E-09	1.77E-06	1.11E-07
698	3.49E-04	1.00E-05	7.62E-02	1.67E-09	2.17E-06	1.35E-07

Calculations for the amount of methane available

Density of methane ~ 0.15kg/m3 @ 1273K

Diameter	Radius	Area	Velocity @ 5psi	CH4 density	Methane available
(microns)	(meters)	(p *r2) m2	(m/s)	(moles/m3)	(moles)
10	5.00E-06	7.85E-11	7.95E-03	9.3504	1.17E-10
50	2.50E-05	1.96E-09	1.99E-01	9.3504	7.31E-08
100	5.00E-05	7.85E-09	7.95E-01	9.3504	1.17E-06
159	7.95E-05	1.99E-08	2.01	9.3504	7.46E-06
199	9.95E-05	3.11E-08	3.15	9.3504	1.83E-05
321	1.61E-04	8.09E-08	8.14	9.3504	0.000123
559	2.85E-04	2.55E-07	2.58E+01	9.3504	0.001231
698	3.49E-04	3.81E-07	3.86E+01	9.3504	0.002754

Figure 2.7. Plot comparing the number of moles of CH4 needed and the actual number of moles available for CNT deposition vs. the capillary tube diameter

Using these parameters, an optimized microreactor setup designed specifically for thermal CVD technique (Figure 2.8) has been shown to successfully modify the inner surface of fused silica chip with carbon nanomaterial thin films. In this setup, methane (CH_4) and hydrogen (H_2) are mixed in 80:20 ratio in a reservoir as shown in the Figure 2.8. A separate N_2 line facilitates flowing N_2 through the reactor during the temperature ramping process, so as to reduce the iron nanoparticles that might have oxidized in ambient air. Valves (Upchurch) are setup along these gas lines, to isolate each from the other during the CVD process. The hydrocarbon gas mixture and Nitrogen gas are filled into syringes that are controlled via basic single syringe, infusion pumps (KD Scientific). These are capable of dispensing syringe contents at controlled flow rates.

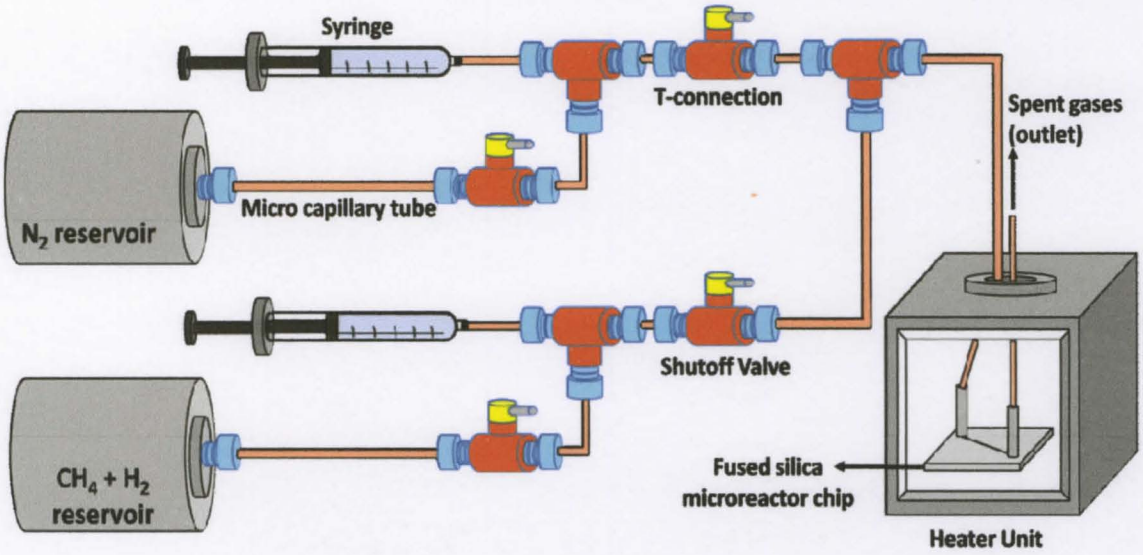

Figure 2.8. Schematic detailing thermal CVD setup for depositing carbon nanomaterial in fused silica chips

Alternately, precursors are introduced into the fused silica chip via gas mass flow controllers (MFCs). For a temperature of 760 ^{o}C and ramp time of 75 minutes, N_2 is sent through the fused silica chip at a rate of 0.8ml/hour via (duration of temperature ramp in oven) followed by hydrocarbon mixture at 3ml/hour. Thermal CVD carried out using these settings successfully deposited carbon thin films on the inner surface of the fused silica chip as can be seen from Figure 2.9.

A close analysis of the type of deposit can be carried out by stripping the chip of its inner-lok ports and dicing the chip carefully (to avoid debris). Figure 2.10 shows a scanning electron microscopic (SEM) image of the deposit on the inner walls of the microchannels.

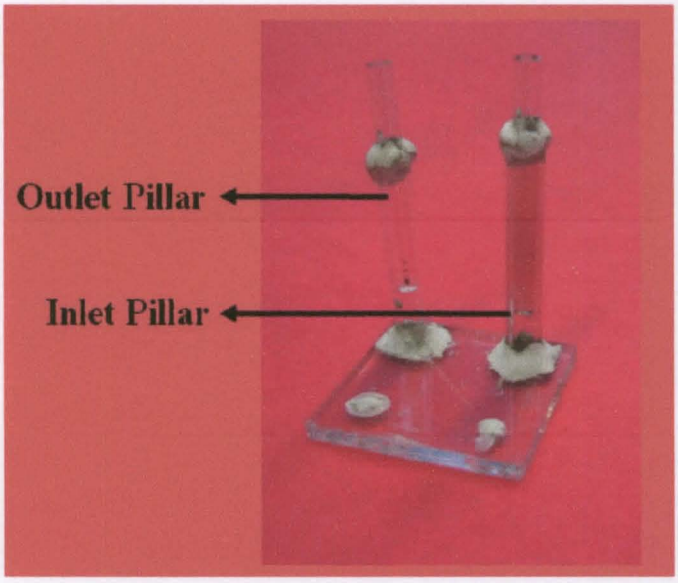

Figure 2.9. Fused silica chip with carbon thin film deposition visible on the inner surface of gas inlet pillar.

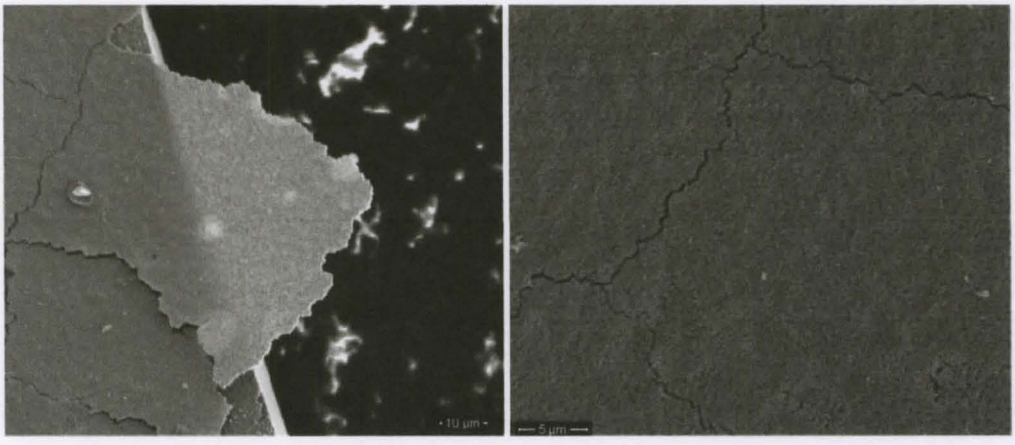

Figure 2.10 SEM image of carbon deposit inside fused silica device

Limitations: The limitation however, in using micro-scale thermal CVD process for in-device growth of nanomaterial in fused silica chips lies is in the prohibitive costs involved in the fabrication (in excess of $200 per wafer) and the extremely time consuming processes involved. Also, the extremely high operating temperatures (in excess of 900 C°), essentially limits the substrates/device materials to only those that can

withstand such high temperatures, driving up the cost of manufacturing each individual sensor device.

2.2.4 In-device growth of carbon nanomaterial in fused silica tubing

Owing to the prohibitive costs involved in fabricating fused silica devices, chemical vapor deposition of carbon sensing material inside fused silica tubing (Polymicro) is explored. These are synthetic fused silica tubing with a standard polyimide coating that makes them flexible and inexpensive to work with. Iron (III) nitrate catalyst solution is prepared and the capillary tubing is loaded with the same and left to air dry. The CVD process involved is described in the succeeding section.

2.2.5 Chemical Vapor Deposition inside fused silica tubing

Thermal CVD: Fused silica tubing of 700 μm inner diameter with a wall thickness of 150 μm is chosen as the microreactor chamber/cvd substrate. After coating the inner surface of the tubing (with iron catalyst particles of 2-10nm), a microheater furnace (MHI. Inc.,) is used to radiatively heat the capillary tube to 1400 ^{o}C. Nitrogen gas is sent in through the system during the heater ramping process and is switched over to a precursor gas mixture containing methane and hydrogen in a 80:20 ratio to facilitate carbon decomposition over the catalyst particles, maintaining the temperature at ~800 ^{o}C. Figure 2.11 shows the microheater and the fused silica capillary tubing before and during the CVD process..

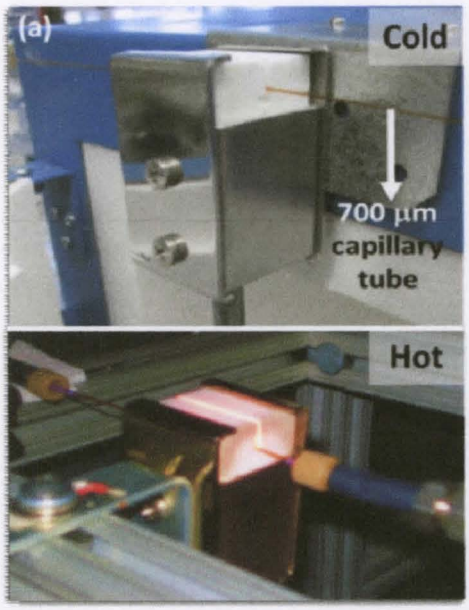

Figure 2.11 MHI microheater furnace and microcapillary tube before and during thermal CVD process

At these high temperatures, the inner surface modification of the microcapillary tube (700 μm) by depositing a dense mat of carbon nanotubes has been shown previously (23). Figure 2.12 shows SEM images of dense mats of Carbon nanotubes grown in microcapillary channels using thermal CVD The thermal CVD process also yields thin carbon films as shown in Figure 2.13. The debris seen on the surface of the deposit comes from the forcible cleaving of the fused silica capillary tubing.

Limitations: Micro-scale thermal CVD process for in-device growth of nanomaterial lies in the extremely operating temperatures (in excess of 800 C°). This essentially limits the substrates/device materials to only those that can withstand such high temperatures, driving up costs and bringing down the options available for feasible sensor substrate materials. To counter this, plasma CVD process is explored.

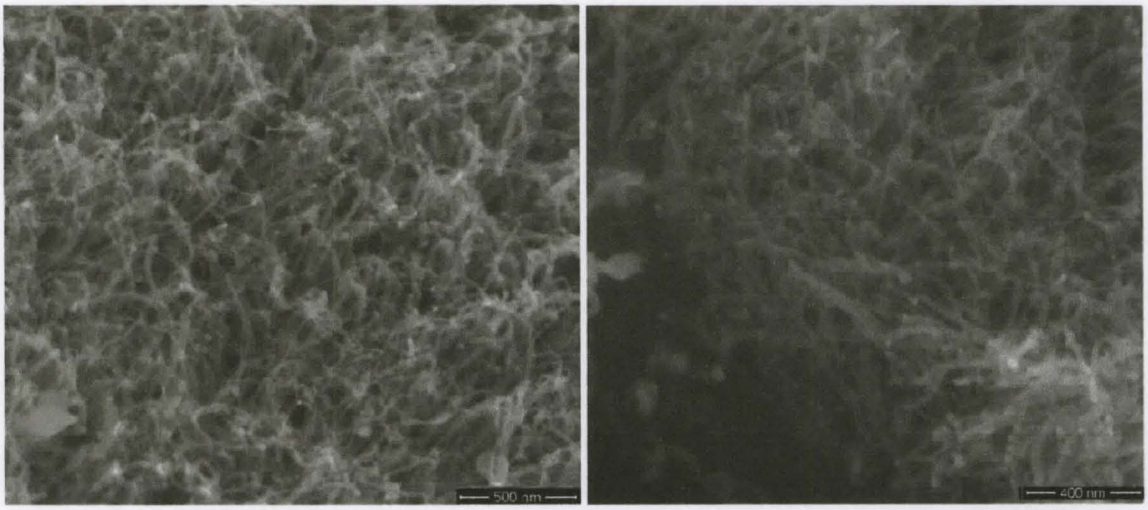

Figure 2.12 SEM images of dense mat of CNTs on the inner surface of microcapillary channels grown in a microreactor environment

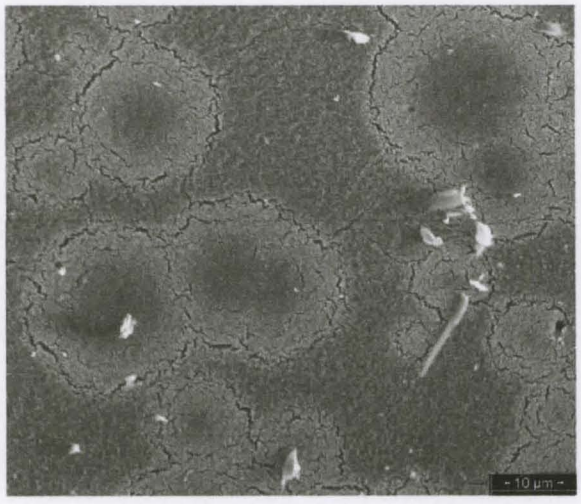

Figure 2.13. SEM image showing thin carbon film deposition on the inner walls of microcapillary tubing in a microreactor environment

Plasma CVD: In macro/large scale, plasma CVD technique has been shown to be a low substrate temperature technique (24). Microplasmas are a special class of scaled down glow-discharges containing highly energetic electrons, which facilitate non-thermal decomposition of precursor gases, and are essentially formed in chambers with

geometries of sub-millimeter length scales (25). Figure 2.14 shows arrangement microplasma sheath ignited inside a microcapillary channel, for the inner surface modification of channel, by depositing carbon nanotubes mats using the process of (micro) plasma enhanced chemical vapor deposition (PECVD) (26).

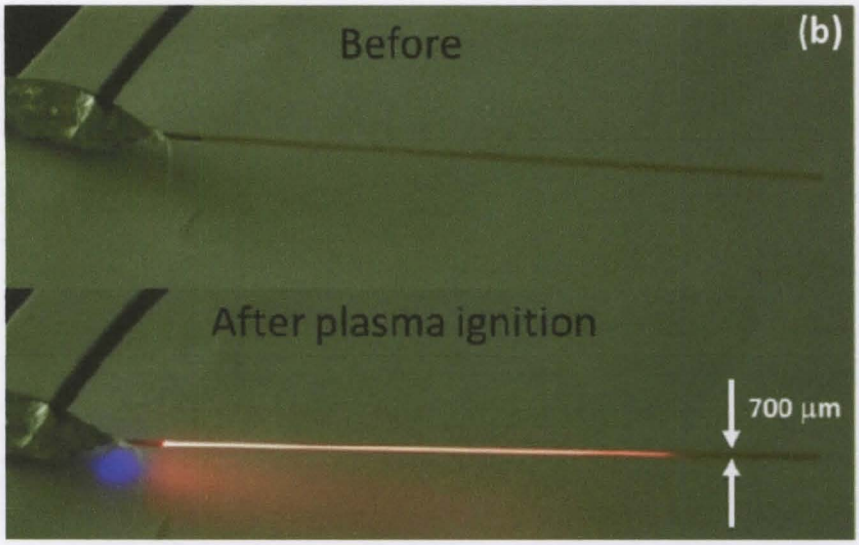

Figure 2.14. Microscale plasma sheath igniting inside a microcapillary tube for Plasma CVD deposition of carbon nanomaterial (26)

Previously, microplasmas have also been used for the synthesis of metal nanoparticles for gas phase studies of CNT growth (27). Compared to thermal CVD, microplasma – CVD is carried out at much lower substrate temperatures (lowest reported is <100C° (26)), making it attractive for in-situ growth of nanomaterials on temperature-sensitive substrates.

Limitations: The process of micro-plasma deposition carries certain limitations where, in spite of lower operating temperatures, the device material/substrate is limited to those that do not interfere with the plasma sheath. Also, the actual growth itself is limited to those nanomaterials that can be synthesized using PECVD technique.

An immensely efficient carbon based nanomaterial- Graphene is one such material that is grown on a metal substrate that is not conducive to PECVD technique. Additionally, the growth conditions involved in the in-device growth of carbon nanomaterials (nanotubes and thin films) limit the geometry and the potential sensor device design. As the proposition of growing graphene on a device directly is not feasible, synthesis of monolayer graphene using traditional techniques (discussed in succeeding chapters) and transferring the as-grown sheet onto the device has been decided to be a better approach for the gas sensor device presented in this study.

2.3 Introduction to Graphene

In the recent years, Graphene, which is a monolayer planar sheet of sp^2 hybridized carbon atoms packed in a hexagonal packed honeycomb crystal lattice structure, has gained immense interest to be used as the next generation material in electronics. It is a semi-metal with charge carriers acting like Dirac fermions with zero effective mass (28) (29), leading to graphene exhibiting mobilities up to 200000 $cm^2V^{-1}s^{-1}$ (30). The zero band gap semiconductor nature of monolayer graphene combined with its unique electronic properties leads to it exhibiting a high opacity value (or absorption) of ~ 2.3% of white light (31) (32) , half-integer Quantum Hall effects (33), low crystal defects - 1/f noise (28) (34) and ballistic transport (in room temperature conditions) up to a micron (35). These properties of high mobility and ballistic transport make graphene extremely attractive in applications like high speed nano-electronics. Other equally astonishing properties of graphene include a breaking strength of ~ 40 N/m, which is very close to predicted theoretical limit and a Young's modulus of ~1.0 TPa (36) thermal conductivity

of ~ 5000$Wm^{-1}K^{-1}$ at room temperature (37), elasticity exceeding that of any other crystal by about 20% (38). Additionally, due to graphene's two-dimensional nature, all its surface atoms are exposed to adsorbing gas molecules – giving rise to the largest sensor area per unit volume (39), paving way for its use as a sensing element.

2.3.1 Graphene Structure

Before attempting to incorporate graphene into any application, it is imperative to understand its structure. Much like mono-layer graphene is a single layer of carbon atoms, bi layer graphene has 2 and multi-layer graphene has 3-10 layers of single graphene sheets stacked one atop the other. Graphene sheets that are stacked to more than 10 layers have been found to have little scientific interest and border on being termed graphite. Graphene has sp^2 hybridization, meaning it has in-plane σ bonds and out-of-plane π bonds (shown in Figure 2.15(b) (40)).

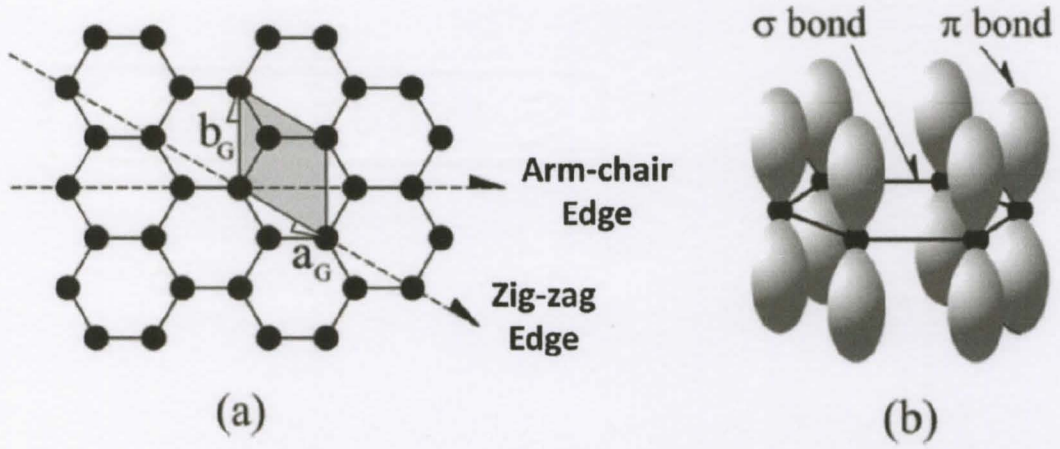

Figure 2.15 :(a) Graphene hexagonal crystal structure. The unit cell (shaded) contains two carbon atoms and is shown along with standard unit cell vectors $\mathbf{a}_G$ and $\mathbf{b}_G$. (b) Schematic of the in-plane σ bonds and the π orbitals perpendicular to the plane of the sheets (40)

The extremely strong σ bonds contribute to graphene's rigid backbone of the honeycomb structure while the π bonds contribute to a system of delocalized electrons. This is responsible for the weak interaction between graphene layers in a stack and also for the electron conduction in graphene. Figure 2.15(a) shows graphene's hexagonal structure of identical carbon atoms. The unit cell (shaded) is shown- containing two carbon atoms at (0, 0) and ($a_G/3$, $2b_G/3$), giving an areal density of 3.820 $A°^{-2}$ (40). The standard unit cell vectors $\mathbf{a}_G$ and $\mathbf{b}_G$ are given by (41)

$$|a_G| = |b_G| = 2.4589\ A°$$

The 'armchair' edge (42) and the 'zig-zag' (43) directions are also shown in Figure 2.14(a). These come into play during stacking of multiple layers of graphene – the three most common arrangements being AA (hexagonal), AB (Bernal) and ABC (Rhombohedral), shown in Figure 2.16 (40).

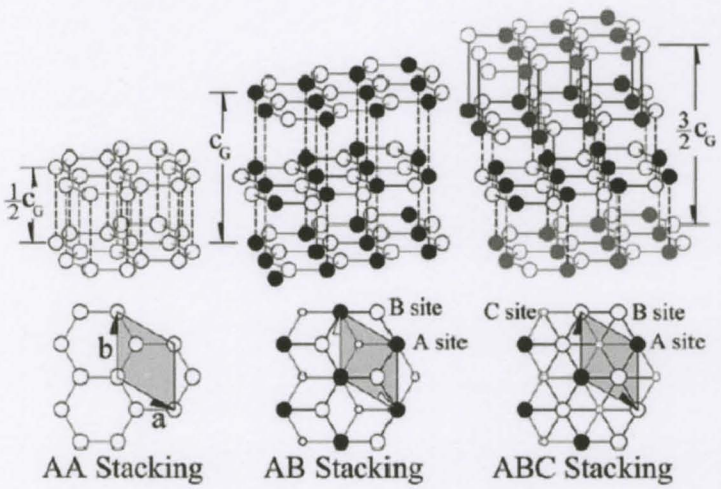

Figure 2.16: Three common stacking arrangements for graphene. AA-Hexagonal, AB -Bernal and ABC – Rhombohedral stacking (Shaded areas show unit cells in each arrangement) (40)

The Bernal stacking is the most commonly seen stacking arrangement in single crystal graphite (44) and is formed when one layer of graphene is rotated 60° with respect to the other along a z-axis. From Figure 2.16, we see that, the distance of separation between two layers is $c_G/2$, where c_G = 6.708 A° at 23C° (41). This is responsible for the sub lattices in both graphene layers, aligning the 'A' atoms positioned one above the other, or a 'B' atom positioned without an atom below it. From the Bernal stacking arrangement we see in Figure 2.15, there is an overlap of π orbitals, which are perpendicular to the plane of graphene leading to a weak bonding between the sheets-AB. This weak interaction (bonds) is called the van der Waals bonds (45). The electronic structure of graphene can be understood from the nearest-neighbor, tight binding approximation that has been proposed – where the two atoms per unit cell in graphene contribute to two conical points K and K′ (Dirac points) where band crossing occurs (Brillouin zone) (46)

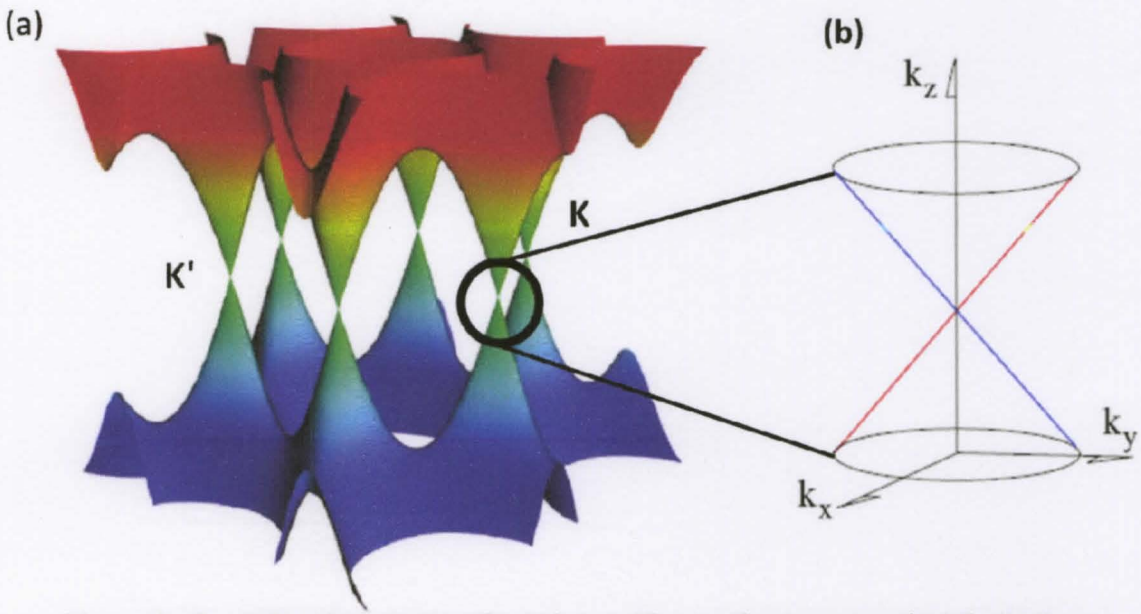

Figure 2.17: (a) Band structure of graphene. The conductance touches the Valence band at the K and K′ points (47) (b) Blow up shows the linear dispersion (Dirac cones) near the K-point in the vicinity of $E = E_F$ (48).

At these Dirac points, the energy dispersion is linear and is given by $E = \hbar\kappa v_F$ where κ is the momentum and v_F is the Fermi velocity given by c/300 ('c' being the speed of light). The 6 Dirac points seen in Figure 2.17(a) form the Fermi surface (E=0), leading to zero effective mass of electrons at E_F (47) (48). Although graphene does not exhibit an intrinsic band gap, a number of different strategies have been proposed and are currently being explored that will lead to opening up the band gap – referred to as 'Band-gap' engineering. As graphene is malleable, any strain or deformation leads to a change in its electronic, phonon and optical properties (38) and subsequent change in its band structure (49), opening pathways to incorporate graphene into several different applications.

2.3.2 Graphene in practical applications

Carbon nanotubes (CNTs) are precursors to research in the carbon-based nanomaterials and act as an analogy or guide to potential applications for graphene. Much like CNTs, graphene has been found to act as a versatile 'filler' material in composites (50). Another emerging area of interest is in nanoelectromechanical systems (NEMS), where the physical properties of graphene (stiffness, lightness among others) are golden traits to be had (51) (52). Figure 2.18(c) shows a NEMS drum resonator made from a 10 nm thick film of reduced graphene oxide, covering a recessed section in a Si wafer (51).

Field effect transistors (FETs) are a potential application for graphene – in a slightly modified form. As graphene intrinsically has zero-bandgap, it cannot be made to function as a transistor in this form. However, by narrowing the width of a graphene sheet to very small dimensions makes it a quasi-one dimensional structure (53) (54) (55) .

This form of graphene is popularly termed as Graphene Nanoribbons (GNRs) and has been shown to function successfully as a transistor. Figure 2.18(a) shows the SEM image of a transistor made of GNR that allows FET action with large On-Off ratios (56). Figure 2.18(b) shows a false color image of a graphene based high-electron mobility transistor (HEMT) that could potentially extend the operational range of HEMTs into terahertz frequencies, giving graphene HEMT devices an edge over the current Ga-As based devices (57). Graphene being a single crystalline material with low atomic mass has been projected to be an ideal support grid in Transmission electron microscope (TEM) imaging.Figure 2.18(d) shows a graphene membrane as a TEM grid (58). The gray background (along the top part) is indicative of graphene, while the carbon atoms in the amorphous layer (section in the image center) appear darker, in a random arrangement of hexagons, pentagons and heptagons.

The extraordinary physical, chemical and optical properties of graphene make it an excellent candidate for conducting transparent electrode applications. The current technology leans heavily on Indium Tin Oxide (ITO) for liquid crystal displays, solar cells and even EMI shielding. The limitations associated with this technology like limited supply of ITO and associated high costs due to the demand lead to the search for an alternate thin-film that is optically transparent, ductile and has excellent thermal, chemical and mechanical stability – namely Graphene (59) (60) (61).

In addition to those mentioned above, the most interesting area of practical application for graphene is in Lab-on-chip devices or electronic noses. Graphene, due to its physical and electronic structure is extremely sensitive to its environment and has

been shown to exhibit high sensitivity, eliciting a response when exposed to an individual gas molecule in a controlled environment (39).

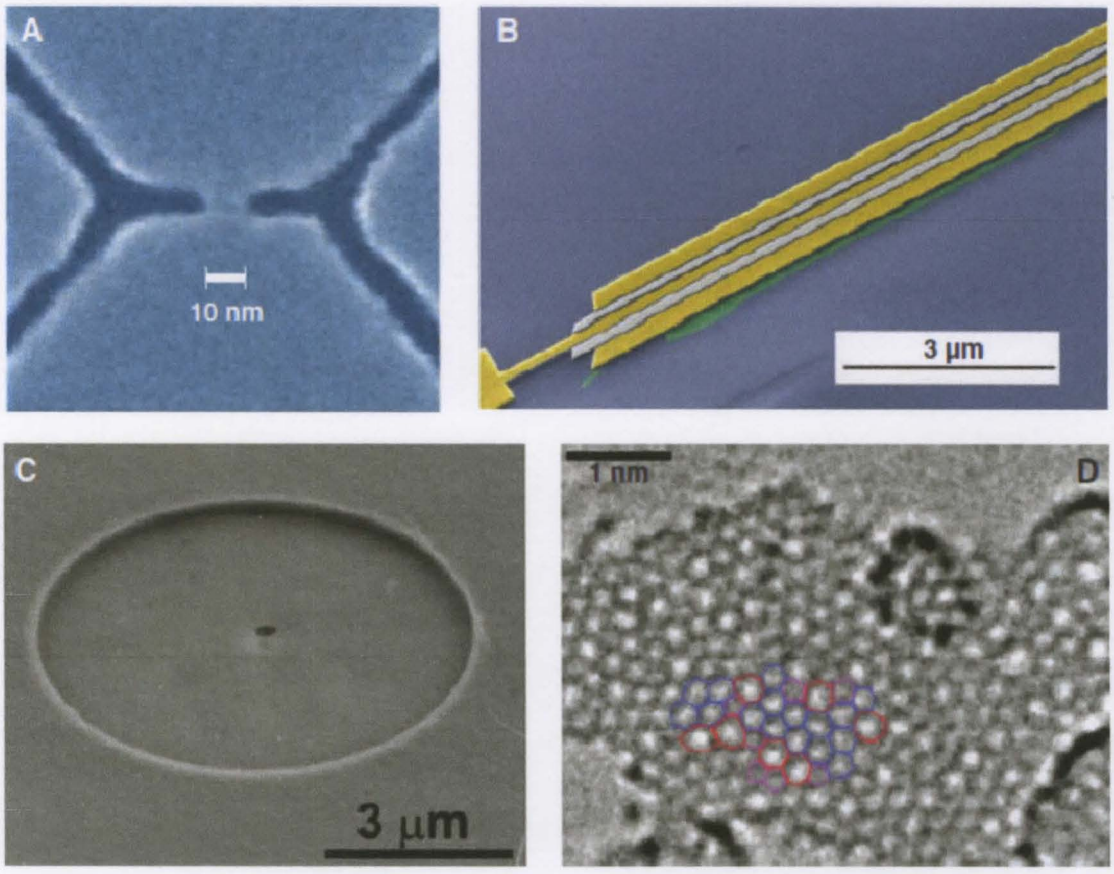

Figure 2.18: (A) SEM image of graphene nanoribbon made by electron-beam lithography for use as a transistor (56). (B) False-color micrograph of a HEMT showing the source and drain contacts in yellow, two top gates in light gray, and graphene underneath in green (C) Graphene-based NEMS (drum resonator) (51) (D) Graphene membranes as TEM grids– highlighted central part is a monolayer of amorphous carbon (58). (Compiled figure courtesy (49))

2.3.3 Graphene for sensing applications

The graphene surface can either adsorb or desorb various gas molecules or atoms (K, -OH, NH_3, NO_2 and the like) from its surface. These surface adsorbates act as either electron donors or acceptors to the graphene layer – leading to a change in the local carrier concentration. This change is reflected in the change in conductivity (or

resistivity) of graphene (39), making it an excellent material for sensing elements. The earliest experimental study of graphene as a gas-sensing element showed the doping effect of ethanol (C_2H_6O), water (H_2O), ammonia (NH_3) vapors on graphene (21). Following this, there has been tremendous increase in interest to exploit graphene to build gas sensors – these efforts however, are still in nascent laboratory level and have yet to reach/translate into commercial scale production.

Various reports have confirmed the gas induced-changes in the conductivity of graphene having different magnitudes dependent on the type of gas molecules the graphene surface is exposed to. The sign of this change (either positive or negative) is dependent on the gas molecules acting as electron donors or acceptors. Since the first report, significant research has gone into understanding how the adsorbing molecules affect the conductivity of the graphene layer. Different theories and experimental data have come into light, that show that changes in the mobility of carrier concentrations or their density, or probably both are responsible for a change in the conductivity of graphene. However, the exact role that each plays is still under debate as various models (of which some take into consideration the coulomb scattering) take up different stands in this respect (39) (62) (63) (64). To further unravel the interaction mechanism between the different adsorbing gases and graphene surface, much more work is to be carried out in addition to the information currently available about the role of charge transfer (that is critical in determining the sensitivity of graphene to gas adsorbates) (65) (66) (67).

Currently, it is accepted that adsorbates like alkali-metal atoms, NO_2 and such-that have an open shell are weakly bound to the graphene surface (which at room temperature, makes them relatively mobile) and some other atoms like those belonging to

H,-OH and the like that form a more stronger covalent bond undergo direct charge transfer to/from the graphene surface. This leads to the zero (tunable) bandgap graphene exhibiting much more sensitivity to surface adsorbates compared to any currently available semiconductor devices that have a much larger bandgap (68). On the other hand, closed-shell gas adsorbates like NH_3 and H_2O act by changing the doping level of graphene by the substrate (support) or alter the charge distribution within graphene rather than directly affect/alter graphene's band structure (69). Additionally, any water molecules that are either adsorbed (from exposure to ambient air) on the surface or trapped between the supporting substrate and graphene layer act as impurities or dopants, that can be reversibly desorbed on vacuum annealing (70). This has also been shown in the case of NH_3 molecules trapped between the substrate-graphene interfaces (71).

Besides the gas adsorbates playing the role of dopants in graphene and dangling edge bonds aiding (albeit only a small fraction ~ 2% (71)) in strong gas molecule adsorption (72), polymer residues (that are a consequence of the processes employed to transfer as-grown graphene onto a substrate of choice) and also hydrocarbon remnant contaminants have been shown to functionalize or contaminate the graphene (73) (39) (74). The problem however arises of the gas adsorbates that form a stronger (covalent) bond with the graphene surface that at times is irreversible (in a reasonable timeframe) unless the sensor is subjected to an external stimulus to release those adsorbates. A successful sensor design therefore balances between the reversibility of the sensor's response to maintaining a decent sensitivity level to adsorbing gases. The next chapters discuss the graphene based device design presented in this work along with the synthesis

techniques, characterization of the as-grown graphene, its transfer mechanism and experiment details.

CHAPTER III

GRAPHENE SYNTHESIS AND CHARACTERIZATION

3.1 Introduction

The synthesis of a monolayer of graphite was first studied by the process of thermal decomposition of carbon on single crystal platinum substrates in 1975 (75). However, it was only in 2004 that synthesis of graphene by the process of exfoliation was reported (21) (76), which earned researchers Andre Geim and Konstantin Novoselov the Nobel Prize in Physics in 2010. Since that time, several different techniques have been reported for the synthesis of mono/multilayer graphene, which have been briefly described in the following sections.

3.2 Graphene Synthesis by Exfoliation/Cleavage

Stacked layers in bulk graphene are held together by weak Van der Waals forces which when broken by imparting either mechanical or chemical energy, yield individual graphene sheets. The mechanical exfoliation of minute traces of graphene from bulk graphite or lead is seen every time a pencil is used to scratch or write on a sheet of paper. Few layer graphene (FLG) is a common occurrence in instances where highly oriented pyrolytic graphite (HOPG) is subjected to smearing/cleaving on a substrate and was

researched as early as 1999 (77). Cleavage of a pure graphite sheet to form a dispersion of scroll-like structures by the process of intercalation using potassium metal followed by exfoliation by ethanol was also reported in 2003 (78). Later efforts report extraction of mesoscopic crystallites of graphite from bulk HOPG by attaching patterned graphite micropillars to an AFM cantilever tip and transferring thin samples onto a Si substrate (79). A schematic showing the microcleaving process using graphite micropillar to deposit thin graphite samples is shown in Figure 3.1 (a,b).

However, a simpler and now very popular method for extracting a single/multi layer graphene was achieved by the process of mechanical exfoliation (or repeated peeling) of 1mm thick platelets of HOPG (supported by a photoresist film) using ordinary adhesive (scotch) tape (21). Figure 3.1(c) shows the "scotch tape approach" depicting transfer of graphene flakes onto the adhesive tape (80). In another approach, single to few-layer graphene flakes of mm-size were produced by exfoliating bulk graphite bonded to borosilicate glass (81).

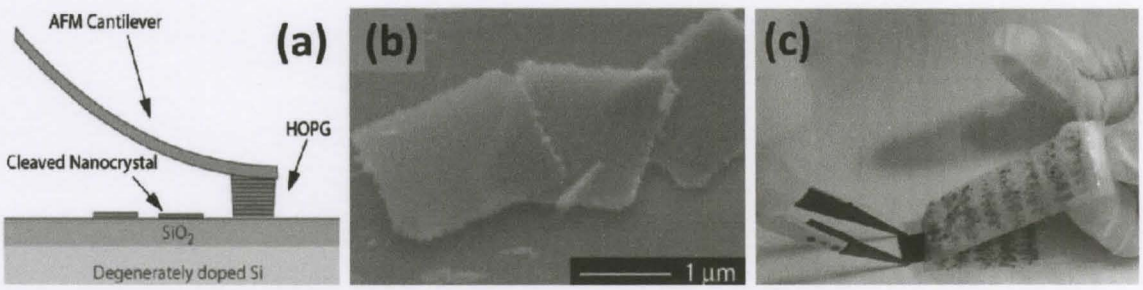

Figure 3.1: (a) Schematic showing the microcleaving process using graphite micropillar mounted onto an AFM tip (b) SEM image of thin graphite samples cleaved onto SiO_2/Si substrate (79) (c) Scotch tape approach for mechanical exfoliation of graphene from bulk graphite (80)

Figure 3.2 shows graphene films transferred onto a Si substrate by the 'scotch tape method' characterized using optical microscope and atomic force microscope techniques.

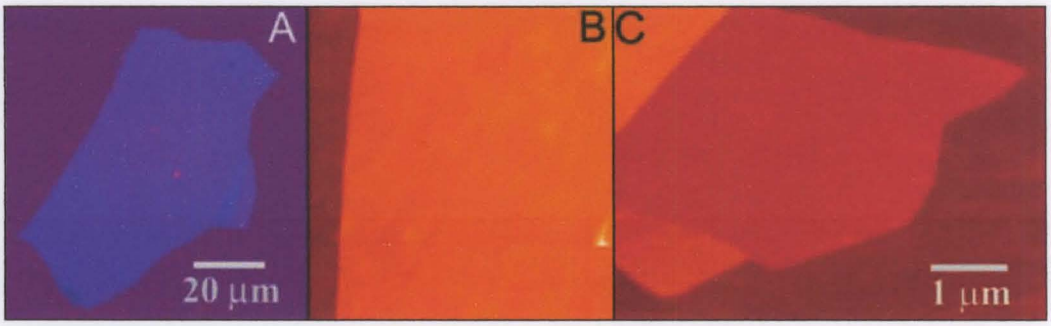

Figure 3.2: Graphene films (A) Normal Light photograph of multi layer graphene flake of ~ 3nm thickness on a Si wafer (B) Atomic force microscope image of the multilayer flake edge (C) AFM image of graphene monolayer (from Ref. (21)

The technique of extracting graphene by mechanical exfoliation or cleavage has so far yielded small amounts of graphene that are useful for fundamental studies but there are certain limitations related to scalability of the process – as it is neither high throughput nor high yield. An alternative approach for synthesizing graphene on large scale is through chemically modified forms of graphene such as graphene oxide (82).

3.3 Chemically derived graphene

Graphene Oxide (GO) is produced by the oxidation of graphite by one of three principal methods which were developed by Hummers (83), Brodie (84) and Staudenmeier (85) and has gained prominence in recent years due to its relatively high yield prospects for graphene production. Chemical exfoliation of GO is carried out in three steps of intercalating the graphite material, expanding and exfoliating the layers of graphite and transferring or depositing the separated layers of graphene onto substrate of choice.

The process of intercalation involves inserting (intercalating) an external compound called a Graphene Intercalation Compound (GIC) between the graphite layers by chemical treatment (86). The compounds are selected such that the graphite layers are left intact while the compound molecules are located between the graphene sheets (See Figure 3.3(a)). On subjecting the treated graphite to heat (87), the intercallant converts from solid/liquid phase to gas phase, resulting in an increase in the volume of the intercallant close to 3 orders of magnitude. The pressure generated by this volume increase forces the adjacent graphene layers to separate, resulting in the accordion expansion observed (88). Figure 3 (adapted from (89)) shows a schematic of the process of expansion and exfoliation. Figure 3.3(a) shows the expansion agent/intercallant (blue spheres) in their metastable residence between adjacent graphene layers. Figure 3.3(b) shows the expanded intercallant and the results of the expansion on the graphene layer spacing.

In a slightly modified approach of exfoliation in liquid phase – the process uses the hydrophobicity of GO sheets to prepare a dispersion by ultra-sonication and subsequent reduction, to separate individual graphene layers (90) (91) (92).

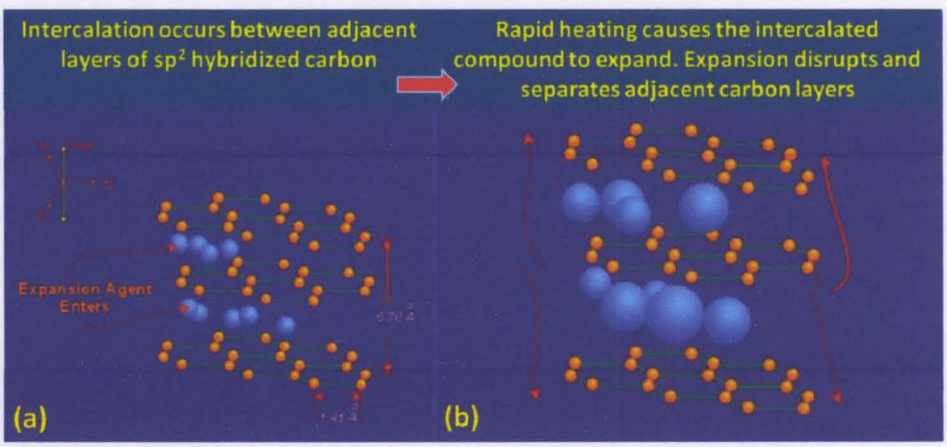

Figure 3.3: Schematic representation of the process of expansion/exfoliation (Adapted from (89))

Recently, reports of varying approaches to obtaining graphene layers from reduced graphene oxide have been made that include microwave treatment and high frequency ultra-sonication and centrifugation for obtaining individual layers of graphene (93). Additionally, extraction of graphene films from graphite using chemical methods but without the exfoliation step has also been demonstrated elsewhere (94) – where oxidized natural graphite was diluted in methanol, and subjected to centrifugation. Very thin carbon nanofilms (CNFs) were obtained from such dispersions. In spite of the high yield of such techniques, there are certain limitation likes the contamination from the intercalating compounds, difficulty in obtaining a consistent yield of wrinkle-free graphene sheets and the transfer of the exfoliated graphene sheets onto an insulating material.

3.4 Epitaxial growth on SiC

The synthesis of wafer-size monolayer graphene by the process of thermal decomposition on silicon carbide (SiC) substrate has been proposed as an alternate to the exfoliation process (95). As SiC is an insulator by nature, this epitaxial growth technique bypasses the transfer step, making it a viable route for the synthesis of uniform, wafer-size graphene layers for technological applications (96) (97) (48). A significant advantage of the wafer-based thin film approach is its compatibility with currently installed infrastructure for semiconductor micro and nanofabrication. Additionally, SiC is a robust material that has superior tolerance towards high temperatures as, in this process, the silicon carbide is annealed in very high temperatures (in excess of 1100 °C) in vacuum to

reduce it to graphene. This approach however produces small grain graphene with inhomogeneous coverage over the substrate surface (98). Large grain, multilayer graphene growth has been reported on C-terminated SiC with 0001 surface (40). However, this technique is limited by the disorder that crops up between different layers in the multilayer graphene. Improving on the earlier annealing technique, large area homogenous growth of monolayer graphene was successfully carried out in ambient air on the SiC (0001) surface (99) (100). Unlike the exfoliation technique, the limitation to the size of the graphene film produced is dependent on the size of the SiC wafer. Figure 3.4(a) illustrates the SiC substrate characterized by AFM and Figure 3.4(b) and (c) show homogeneous single domain graphene layer and two-domain graphene layer growth respectively on most of the sample (99).

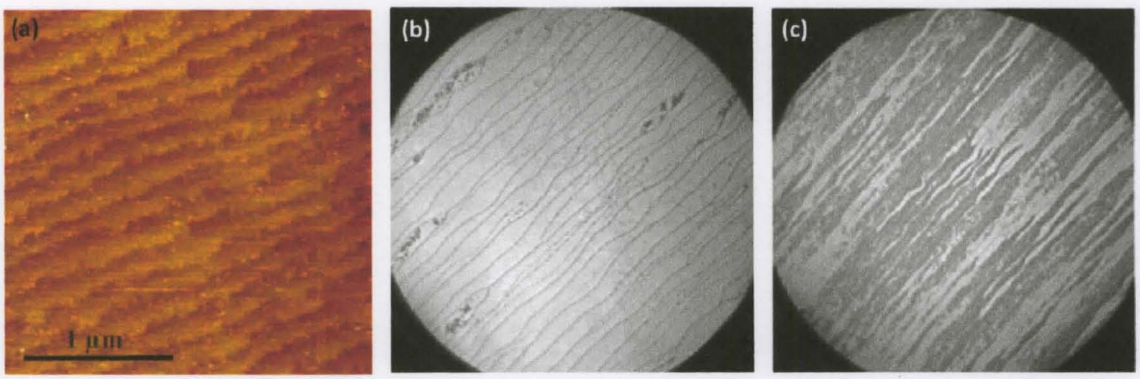

Figure 3.4: (a) A typical AFM image of the substrate surface before graphene growth (b) LEEM image of a single domain monolayer graphene sheet grown ex situ on SiC (0001) (c) LEEM image illustrating the existence of two domains of monolayer graphene (99)

An important issue in epitaxial growth of graphene on SiC is the interface layer between the graphene and the substrate. The electronic properties and structure of this interface are known to play a role in modifying the as-grown graphene properties. Further research

might lead to good control over the number of layers grown on the substrate, as well as the interface effects, paving the way to large scale wafer synthesis of graphene with predictable, uniform and controllable performance in devices.

3.5 Unzipping of carbon nanotubes

One recent development in graphene synthesis techniques uses multiwalled carbon nanotubes (MWCNTs) as the starting material and involves 'unzipping' them to obtain graphene layers (see Figure 3.5(a)).

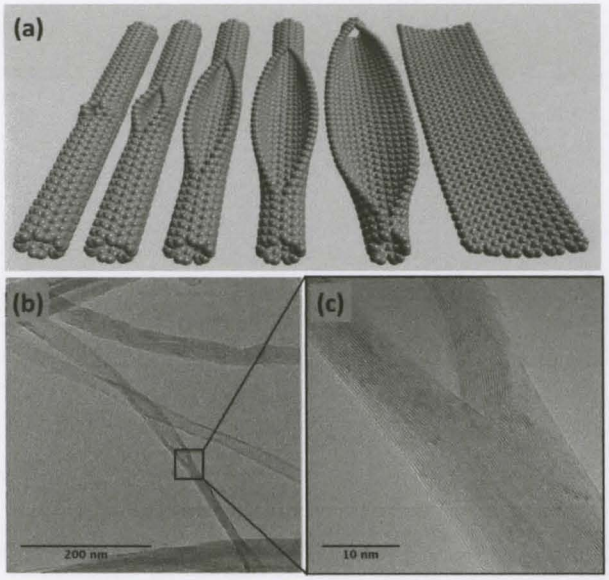

Figure 3.5: (a) Representation of the gradual unzipping of one wall of a carbon nanotube to form a nanoribbon (103) (b) TEM image of a partially opened MWNT (c) Enlargement of the area in (b) where the nanotube unwrappping stops or collapses (101).

This is a unique approach as the synthesis process is essentially 'substrate-free'. One of the earliest reports details longitudinal unzipping or opening of MWCNTs by the process of intercalation and subsequent exfoliation (101). An opened MWCNT is shown in Figure 3.5(b,c).

Plasma etching MWCNTs has also shown to produce graphene nanoribbons (102). Additionally, severe chemical treatment of MWCNTs including exfoliation, oxidation and reduction has also been reported to produce graphene (103).

3.6 Chemical Vapor Deposition

The purpose or aim of depositing a thin film using the process of chemical vapor deposition is to synthesize a pure functional material with specific electrical, mechanical, magnetic, optical, chemical properties or even a combination of any of these properties (104). Defined broadly, chemical vapor deposition (CVD) involves formation of solid thin films on a substrate by the chemical reaction of vapor phase precursors (both gas phase and on substrate surface). Different approaches can be taken to initiate the chemical reactions – High frequency radiation like UV termed photo-assisted CVD, plasma enhanced CVD or by breaking down the precursors by heat (thermal CVD).

In a chemical vapor deposition reactor, forced flow of precursors/gas species into the reactor chamber sets off the sequence of events before deposition can occur. These gas species diffuse through the boundary layer that exists above the substrate surface, react with the surface and are either adsorbed or are incorporated into the lattice, by undergoing chemical reactions at the interface. The residual by-products from the chemical reactions desorb from the surface, diffuse through the boundary layer and are carried out of the reactor by the gas stream. The sequence of events occurring during deposition in a chemical vapor deposition process is shown schematically in Figure 3.6 (105). It is to be noted however, that boundary layer conditions are applicable only in

CVD processes taking place in the higher pressure regimes in the viscous flow range (for example- in atmospheric pressure CVD). In case of very low pressure CVD, where molecular flow range prevails, the boundary layer conditions cannot be applied. The rate limiting step in a general CVD process is shown in Figure 3.7 (105), where the pressure and furnace temperature determine which of the two is more dominant – the surface reaction kinetics or mass transport phenomenon .

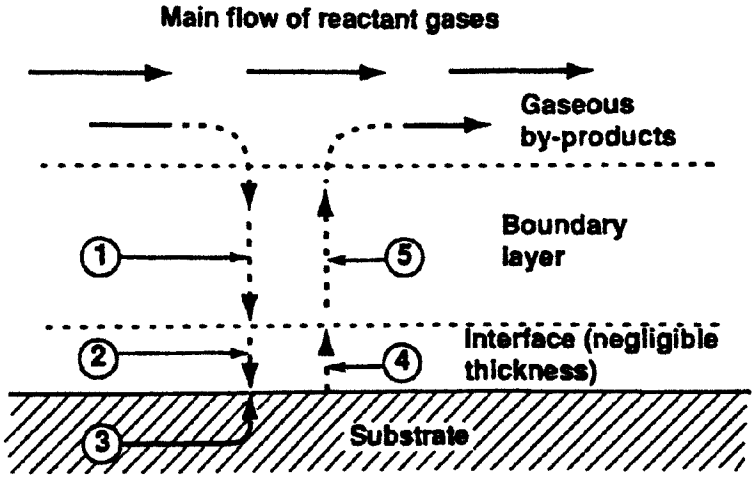

1. Diffusion in of reactants through boundary layer
2. Adsorption of reactants on substrate
3. Chemical reaction takes place
4. Desorption of adsorbed species
5. Diffusion out of by-products

Figure 3.6: Sequence of events in a chemical vapor deposition process (105)

In the case of lower synthesis temperatures, the thin film growth rate is dependent on the surface reaction kinetics – where the chemical reactions occur either in the gas phase or on the surface of the substrate. The growth rate is controlled by substrate temperature and increases exponentially – according to the Arrhenius equation

$$Growth\,rate \propto e^{\left(\frac{E_A}{RT}\right)}$$

where, E_A is activation energy, R is the gas constant, T is temperature

It has been seen during the early attempts at synthesizing CNTs inside a microreactor environment, amorphous carbon films tended to be the dominant form of deposition. This is due to the high growth rates and low substrate temperature conditions, where the rate of precursor gas flow is much more rapid than surface diffusion of species.

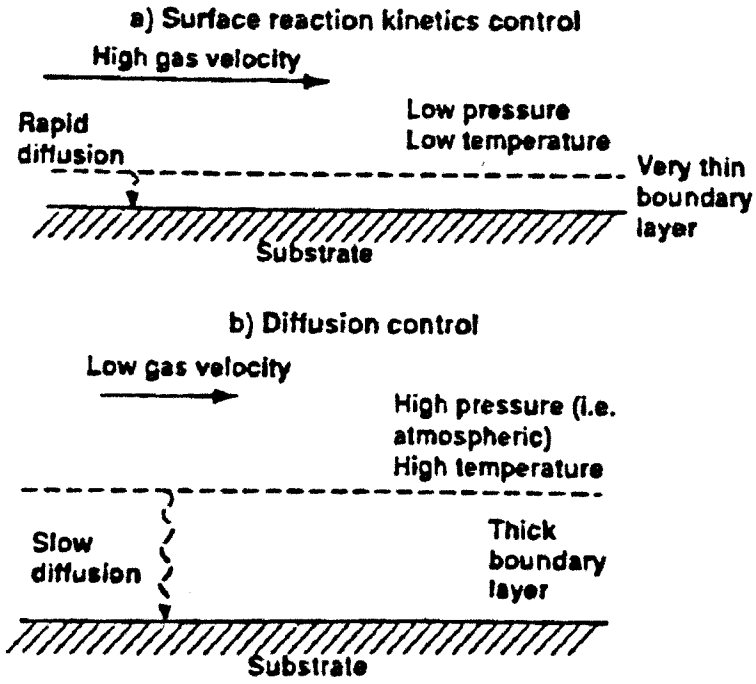

Figure 3.7: Rate limiting steps in a general CVD process

As layer morphology (crystallinity – fewer defects in graphene layer) is an important factor in determining the physical characteristics of the deposited thin film, the temperature of growth, the pressure range in the rector chamber and the partial pressures of the gases are identified as the key aspects to be monitored (as these in turn control the surface diffusion and the nucleation process steps). Hence, optimization of CVD

parameters is imperative to obtain a homogenous deposition of thin film (either carbon nanotubes of mono/multilayer graphene) over the substrate surface. The section below discusses the CVD process involved in the synthesis of graphene for the express purpose of using it as a sensing element.

3.6.1 Thermal CVD process for synthesis of graphene

The first report of electric furnace production of graphite was made in the late 1890's in a patent that led to a rapid commercialization of the process for bulk production (106) . The success of a reactor's design is highly dependent on the homogenous growth conditions that exist inside the active region of growth and the three main performance aspects of quality of the deposited film, its uniformity and the throughput. Several factors play a role in defining these performance aspects, like the precursor purity and substrate/seed quality. From a practical perspective, it is essential that the synthesized thin film adheres well to the substrate. This is possible if the substrate (here, copper) surface is cleaned properly prior to the actual process of CVD.

3.6.1.1 Pre-treatment of copper substrate

The effect of deposition parameters has been known to have a minimal influence on the properties of as-grown graphene. However, several factors come into play for the copper foils chosen to act as the seed layer for graphene growth. Copper in atmospheric conditions, is covered in native oxide that is a deterrent for CVD as it reduces copper's

catalytic capacity (107). Also, any impurities on the surface can considerably affect the amount or mode of nucleation of graphene. Therefore, treating the copper foil/substrate prior to subjecting to graphene CVD becomes imperative. This can be achieved by either of two ways – by treating the foil in acetic acid (108) or by annealing it in the presence of H_2 at 1000°C (109).

In the current work, 25 μm thick copper foil samples are dipped into acetic acid for 10 minutes to remove any oxide on the copper surface, followed by drying with compressed air. Pretreatment via annealing is also important for developing large grain domains and eliminating any surface structural defects on the copper foil. This is carried out in the reactor chamber after establishing chamber pressure of 100 mTorr, prior to introducing the precursor gases. The annealing is carried out as per established recipe at 1000 °C for 30 minutes (110) (111) (112) (113) while maintaining the H_2/Ar flow. Figure 3.8(b) shows the copper sheet – pretreatment schematic (first three steps pertain to cleaning and annealing of the copper sheet, while the last two steps show graphene nucleation islands and subsequent growth). Annealing has also been shown to play a role in the crystallization of amorphous carbon thin films after the end of a deposition cycle, if the sample is exposed to heat from the furnace in a microreactor environment, as can be seen in Figure 3.9.

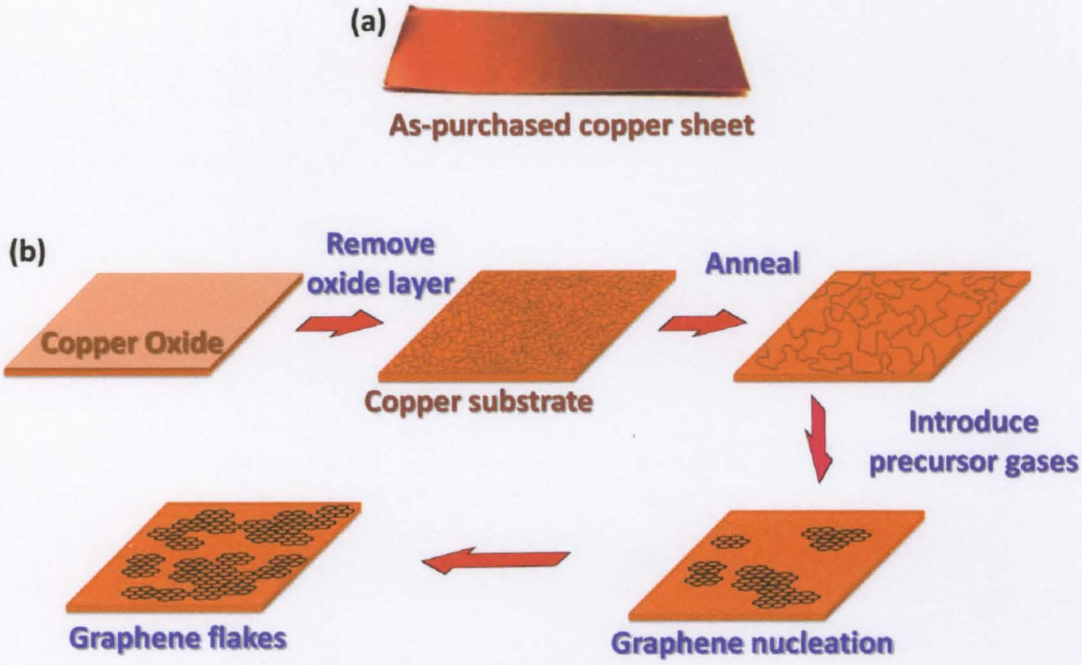

Figure 3.8 (a) As purchased copper sheet (156) (b) Schematic showing in the first three steps - cleaning and annealing of the copper sheet, followed by the last two steps showing graphene nucleation in islands and subsequent growth

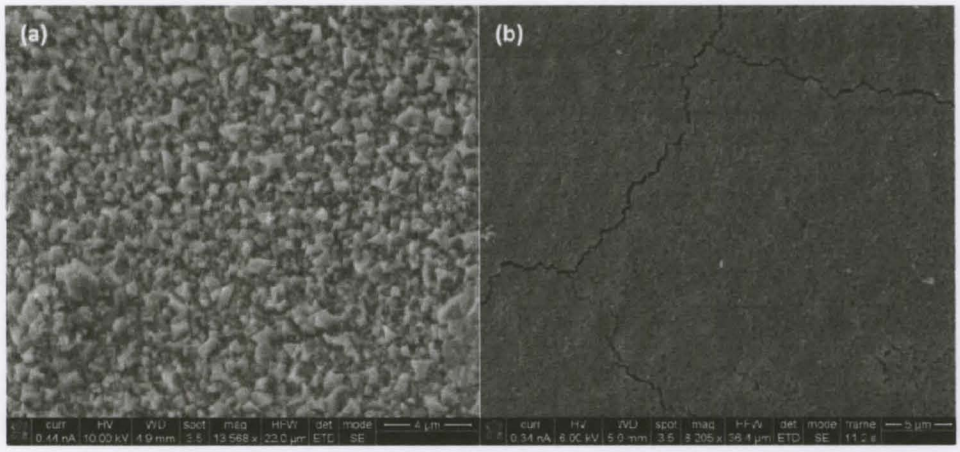

Figure 3.9: (a) Amorphous carbon thin film in the absence of annealing (b) Annealed carbon thin film showing crystallization and improved surface morphology

3.6.1.2 Surface catalysis

The process of graphene synthesis can be divided primarily into two sections – the dissociation of hydrocarbons precursors and the subsequent nucleation of graphene on the copper seed layer from these dissociated species of carbon. To avoid the formation of amorphous carbon films, it is important that precursor dissociation and the resulting chemical reactions are only heterogeneous in nature. This is because, the amorphous carbon (called soot) that deposits on the graphene surface can lead to the formation of graphene-soot compounds, thus altering the properties of as-deposited graphene. The cleaned copper seed layer thus acts as a catalyst and reduces the work function of the reaction, increasing the chances of obtaining a heterogeneous reaction inside the CVD chamber. The other popular catalyst used for graphene synthesis is polycrystalline Ni (114) (115), though it is notorious for producing multilayer graphene as opposed to the monolayer growth seen on copper substrates. It has been proposed that at elevated growth temperatures, (multilayer) graphene growth occurs by the process of diffusion of carbon into the bulk of the seed layer (due to the high carbon solubility of Ni), followed by segregation (114) or precipitation (115). In contrast, the carbon solubility in copper is low (almost negligible), leading to the growth of graphene layer by surface adsorption.

This multilayer growth is better explained from Figure 3.10 (116) that shows phase diagrams for Ni and Cu and reveals the solubility of carbon in these metals. From Figure 3.10(a), it is clear that at temperatures exceeding 800 C°, the carbon solubility forms a solid solution and when temperature is lowered (conditions that exist in CVD reactor during cool-down process), the solubility decreases, leading to carbon

precipitating out of Ni bulk. This precipitation happens preferentially along the grain boundaries of Ni – hence thicker graphene layers are obtained at these boundaries than within the boundaries – leading to multi layer graphene growth across the substrate. Cu has low affinity to carbon – with low carbon solubility of ~ 0.001 -0.008 wt% at ~1084 ° C (117) (118) . This is due to copper having only half filled 3d shell and being able to form only 'soft bonds' by charge transfer from the π electrons (sp^2 hybridized electrons) present in carbon. The low carbon solubility combined with its ability to stabilize carbon on its surface (even if only by 'weak bonds') therefore makes copper an ideal seed layer for the growth of monolayer graphene.

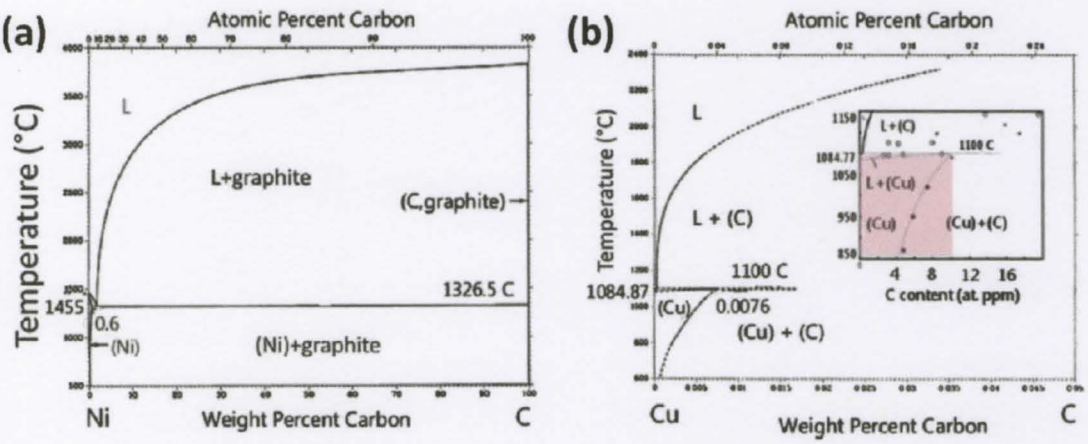

Figure 3.10: Binary Phase diagrams of transition metals (a) Ni-C (b) Cu-C (117) (inset shows low carbon solubility in copper (118))

Figure 3.11 shows a schematic where (a) details the carbon dissolution into the bulk of the Ni seed layer, segregation from the bulk to the metals surface and subsequent precipitation-mediated growth of graphene, (b) shows the graphene growth on copper that is surface mediated and self-limiting in nature - leading to the growth on monolayer graphene

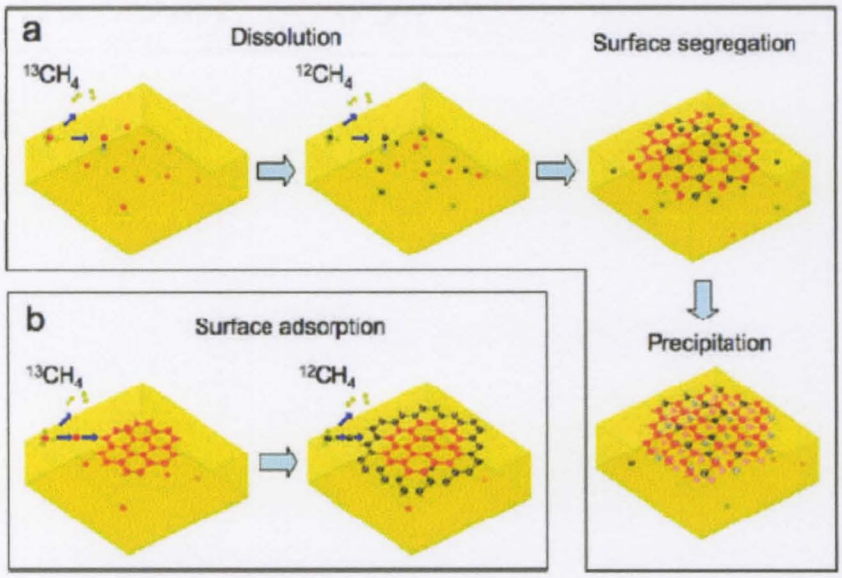

Figure 3.11: Schematic of possible distribution of C isotopes in graphene films based on different growth mechanisms (147)(a) Graphene growth by surface segregation/dissolution (seen when Ni used as catalyst) (b) Graphene growth by surface adsorption of separated C isotopes

3.6.1.3 Graphene growth on copper

The process of thermal CVD for graphene growth is essentially straightforward. The cleaned Cu samples (from previous step) are placed in a 2″ quartz tube Thermolyne F79300 CVD furnace and the temperature is ramped up to 1000 °C in the presence of 2sccm H_2 and 18 sccm Ar while maintaining a pressure of 100mTorr. Following this, 10 sccm of methane (CH_4) is introduced into the existing gas stream, bringing the chamber pressure to 500mTorr for the duration of the growth period (15 minutes) (119). At the end of this process, the furnace is cooled down slowly while maintaining the gas flow and the pressure. Figure 3.12 shows the schematic of the CVD chamber used for the synthesis of graphene monolayer on copper substrate.

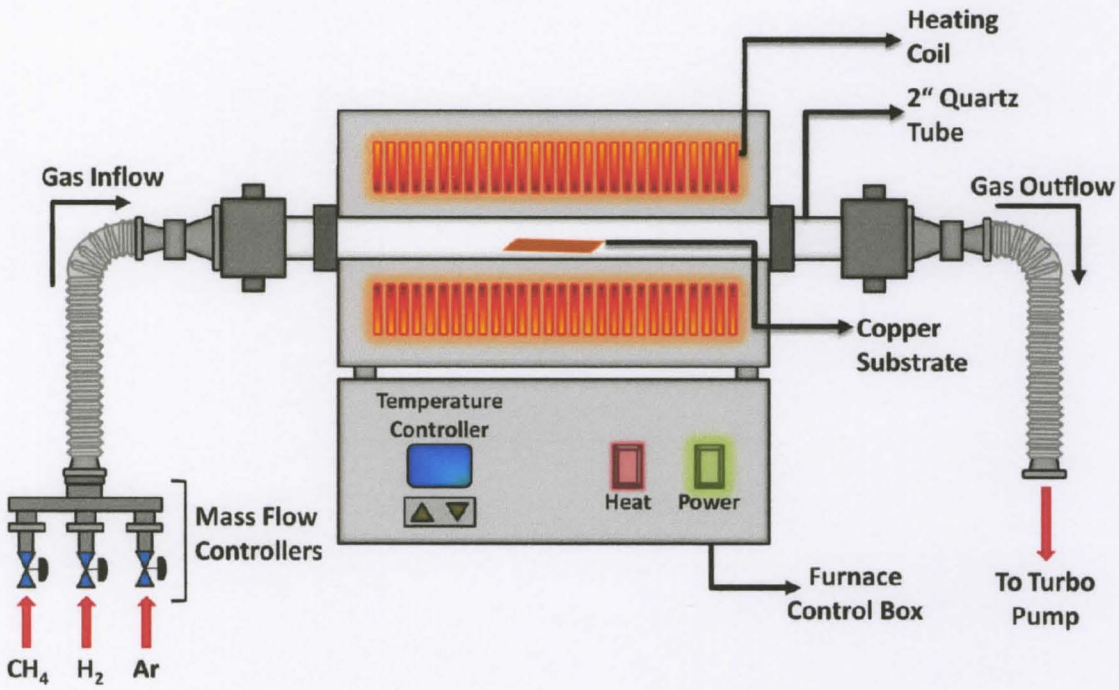

Figure 3.12: Schematic of CVD reactor used for synthesis of graphene on copper

3.7 Characterization Techniques

Any thin film deposited by CVD needs to be characterized to determine its purity and composition – especially where the synthesis of such materials is application oriented. The composition of the as-grown graphene can be measured using any of the techniques of Auger electron spectroscopy (AES), energy or wavelength dispersive X-ray analysis (EDX or WDX) or X-ray Photoelectron spectroscopy (XPS) and Raman spectroscopy. This section of the chapter details the analysis of the as-grown graphene samples using Raman spectroscopy while further characterization using XPS is carried out on the sample after transfer (see Chapter IV)

3.7.1 Raman Spectroscopic analysis

In the last decade, experimental studies on graphene have led to Raman spectroscopy emerging as the forerunner in spectroscopic analysis techniques. Previous knowledge of the characteristics of Raman spectra obtained from carbon nanotubes has greatly helped in the current level of understanding of the phonon modes in graphene/graphitic systems. As graphene is an atomically thin layer, conventional nanomaterial imaging techniques like SEM are not feasible methods to determine the thickness of the as-grown graphene layer. Atomic Force Microscopy (AFM) technique identifies between single and two layers of graphene transferred onto an oxidized substrate (usually Si) but, has the disadvantage of very low throughput. The deficiency in characterization techniques is filled by Raman spectroscopy that has been demonstrated to fingerprint single, bilayer and few layer graphene (FLG) efficiently (120). In the current work, Raman spectra are measured on single layer graphene (as grown on copper) initially. Later, in chapter IV, Raman spectra of graphene transferred onto an insulating substrate is also shown.

A unit cell of monolayer graphene consists of two carbon atoms (A and B) , as can be seen from Figure 3.13(b), and therefore six phonon dispersion bands that are shown in Figure 3.13(a) (121). An understanding of the phonon dispersion in graphene is essential when trying to interpret its obtained Raman Spectra. Of the six phonons dispersion, three are acoustic (A) in nature, while three are optic (O) in nature. A brief discussion of these modes will greatly help in understanding the bands that are obtained

in Raman spectra. For one Acoustic (A) and one Optic (O) branch of phonons, atomic vibrations are seen to be perpendicular (out-of-plane (o)) to the graphene layer. For two acoustic, two optics branches, the atomic vibrations are in-plane (i). Additionally, the wave vector k specifies whether these vibrations run parallel (Longitudinal (L)) or perpendicular (Transverse (T)) to the wave propagating direction. i.e., The in-plane modes include longitudinal acoustic (LA), longitudinal optical (LO), iTA and iTO (where, the latter are normal to the LA, LO modes) and the out-of-plane modes are the oTA and oTO (these are normal to all the other 4 modes of LA,LO, iTA and iTO) (122). Figure 3.13(a) depicts all these phonon modes and can be used to specifically characterize graphene, graphite and carbon nanotubes. The phonon modes around the K point are of special interest as the band structures named D and G′ band manifest from the phonons that are in the area around the K point.

For monolayer graphene, two major peaks are of interest in the Raman spectra. The first is called the G band and occurs around ~1580 cm^{-1}. This is associated with the LO phonon mode and is a very dominant peak in graphitic structures. The second is the 2D or G′ band that occurs at ~ 2700 cm^{-1}. It is to be noted that the frequency of the 2D band is dependent on the excitation energy of the laser (E_{laser}) being used in the Raman analysis, shown in detail in Figure 3.13(c) (123). As the number of layers in graphene samples increases, the associated change in the width and intensities of the G and G′ band can be noticed (due to the interaction between the stacked layers) (124).

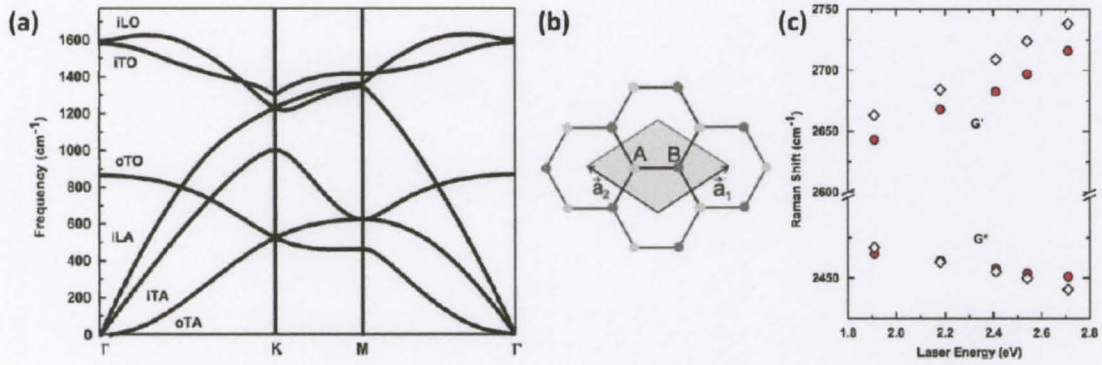

Figure 3.13: (a) Calculated phonon dispersion of graphene (121) (b) Top view of a unit cell in monolayer graphene showing the inequivalent atoms A and B and unit vectors a_1 and a_2 (c)Dependence of ω_G and ω_{G*} on laser energy E_{laser} (circles correspond to graphene data and the lozenges correspond to turbostatic graphite (123)

The other significant band to be aware of in sp^2 hybridized graphitic systems is the D band. Graphene edges, disordered stacking and defects in the atomic lattice give rise to D (disorder-induced) band that occurs at ~ 1350 cm^{-1} (for E_{laser} of 2.414 eV). A lot of information regarding the graphene sample can be gleaned from all three bands, their relative intensities and full width half maximum (FWHM) values. Figure 3.14(a) (120) shows the comparison of Raman spectra at 514 nm for bulk graphite and graphene.

In the current work, the as-grown graphene samples are characterized at room temperature using a Renishaw Raman spectrometer at 632nm, and 100X objective, with notch filters cutting in at ~ 100cm^{-1}. Extreme care is to be taken to prevent sample damage during characterizing by the localized laser induced heating. All measurements are carried out at ~ 4 to 0.04mW of the incident power. From Figure 3.14(b), it can be seen that the two most intense features are the G-peak at ~ 1580 cm^{-1} and a G′ band at nearly 2640 cm^{-1}. Also, the absence of D peak proves that there are no significant defects on the graphene layer.From Figure 3.14(a), the Raman spectra of bulk graphite shows

that the intensity of G (I_G) is much greater than intensity of the 2D peak (I_{2D}) and has spectral components (shoulders on the peak) called $2D_1$ and $2D_2$ (125).

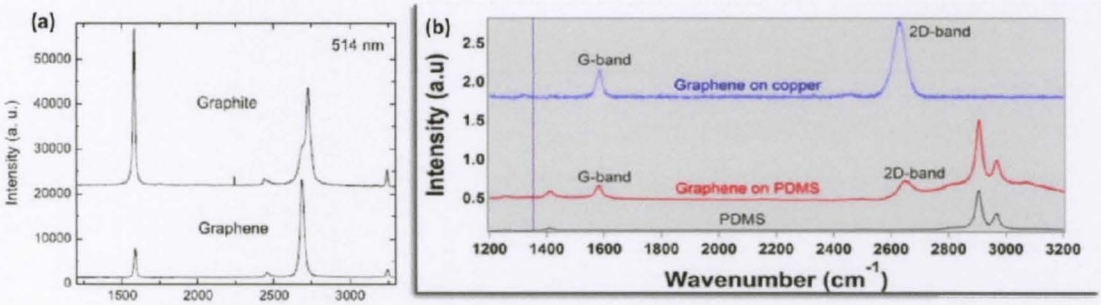

Figure 3.14: (a) Comparison of Raman spectra for bulk graphite and graphene (120) (b) Raman spectra characterizing monolayer graphene grown on Cu (133)

This is in contrast to the single sharp 2D peak obtained in graphene samples (see Figure 3.14 (b)), where the I_{2D} is ~ 4 times the I_G. The peak positions and their FWHM values confirm that the as-grown graphene on copper is monolayer in nature.

CHAPTER IV

DEVICE DESIGN AND EXPERIMENT SETUP

4.1 Overview

The resistive chemical sensor design involves measuring an effective change in resistance of the graphene sheet when exposed to analyte vapors. Due to the bipolar nature of graphene, it can exhibit either an increase or a decrease in its resistance depending on the analyte vapors acting as either electron donors or acceptors. The design involves creating an enclosed channel over the length of the graphene surface and incorporating two electrode ports (in case of single ended voltage measurements) or four electrode ports (in case of differential voltage measurements). Figure 4.1 describes the device as a simple circuit, with a one port acting as a 400mV AC signal input and the other port at ground potential. Graphene has a baseline resistance of R_1 (measured in the presence of N_2). When an analyte gas flows through the gas channel – molecules adsorb onto the graphene surface in the gas channel leading to a change in the local electron carrier concentration (leading to R_2) as a parallel resistance across the circuit. The effective change in resistance is the response of the graphene layer to the analyte vapor.

For the sensor device to register the change in graphene's resistance, the design requires a hermetic seal around the gas channel as well as electrode ports. This is achieved by using acrylic as the base and top plate material with gas channels etched in to the top plate and bonding the plates together, essentially creating gas channel isolated

from the rest of the device. The materials used and the corresponding design are further discussed in the succeeding sections.

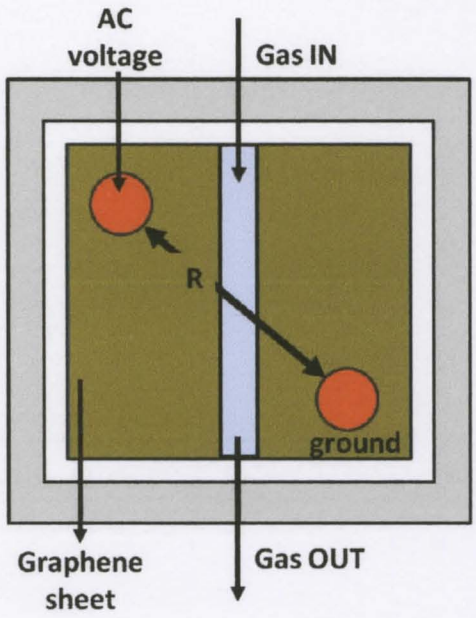

Figure 4.1. Schematic showing simplified circuit in resistive sensor device

4.2 Sensing Organic Solvent Vapors

The sensitivity of graphene to various organic solvent vapors (ethanol, methanol and isopropyl alcohol) is investigated by resistance measurements. Experiments were designed to investigate the sensor response to different volume fractions of these organic solvent vapors defined by vapor pressure. Initial experiments dealt with single ended AC voltage measurements following which, differential voltage measurements have been carried out – to eliminate noise as well as obtain stable measurements. Keeping in mind the initial goal – reducing the cost of manufacturing a working sensor device, appropriate materials have been chosen to build the sensors.

4.3 Device design

Acrylic is a term used to describe a thermoplastic material made from poly(methylmethacrylate) or PMMA. Chemically, it is the synthetic polymer of methyl methacrylate and is characterized by its impact resistance and light weight. Also called as acrylic glass, it is a very clear material, allowing 92% of visible light to pass through it – making it a popular alternate to glass in several domestic/commercial applications. Some of the salient features of the acrylic material in being chosen as the packaging for the graphene sensor described in this work are its moderate properties of thermal expansion and modulus of elasticity, ease of processing and handling the acrylic sheet, and low cost. In this work, for packaging the graphene sensors, extruded acrylic boards of 0.08″ are purchased from McMaster Carr. Extruded acrylic is made through a process in which the liquid plastic is pushed through rollers, which press it into sheets as it cools. This is a comparatively inexpensive process, but the resulting sheets are softer than cast acrylic, making it easier to engrave and cut them using the EPILOG laser mini (see Figure 4.2).

The Epilog Mini uses a CO_2 laser to engrave and cut the acrylic sheet into the required package size of the graphene sensors. With a power consumption of 600W (at full power engraving/cutting and constant Laser ON), and power costing around $0.075/KWH, the cost of running the EPILOG Laser for an entire 8 hour work day comes to around 36 cents. Shown in the second inset in Figure 4.1, the integrated vacuum hold-down table in the Epilog laser systems uses the air from the exhaust fan to hold thin sheet stock flat. This built-in method of securely holding thin sheet stock in place is a large benefit to as it eliminates the need for double-sided tape when creating a mask using Polyethylene Terephthalate (PET) or more commonly called Mylar films. This

revolutionary feature saves significant time when engraving and cutting plastic, aluminum sheet stock and any other thin material that will not lay flat on its own. The chip packaging involves a lock-and-key design with a base plate and a top plate that snap into place during bonding, sandwiching a transferred graphene layer in between schematically shown in Figure 4.3. This design concept is realized by making shallow indentations into a solid thin piece of acrylic, that form the channels for the gas flow (as can be seen in the top plate shown in Figure 4.2), while another square section is etched into the base plate. To make these indentations, a blueprint is to be created first, specifying the gas flow channel dimensions and specific locations of the electrode ports. Figure 4.4 shows a blueprint of the acrylic chip design, drawn using Adobe Illustrator CS5.

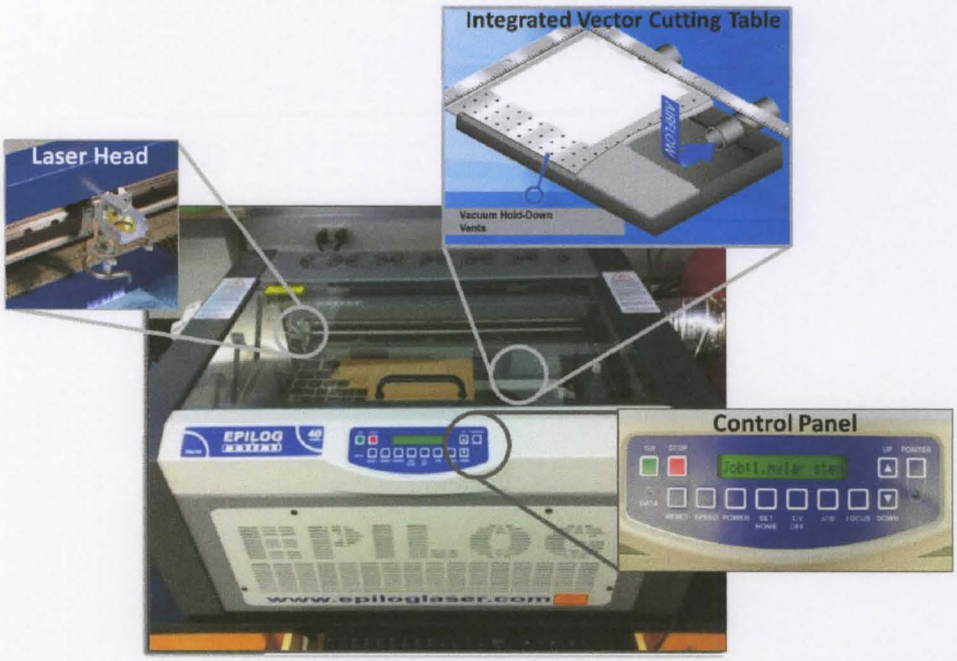

Figure 4.2. Epilog Mini Laser with insets showing the positioning laser head, the integrated vector cutting table and the main control panel

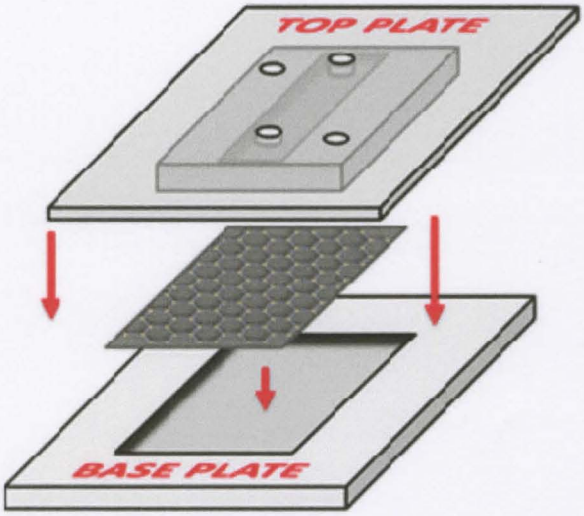

Figure 4.3. Schematic showing sensor device design

A single channel device is designed to have a footprint of 10X10 mm while a dual channel device footprint is designed to be around 21X21 mm. Keeping in mind the larger footprint of the dual channel device, to facilitate good bonding of the plates, the device design is slightly modified to include 2 pairs of vertical and one pair of horizontal notches in the base and top plates. An interrupted groove is also included in the design to facilitate a secure lock when the plates are bonded together, preventing any leaks (see Figure 4.4(c)). The single channel chip blueprint, shown in Figure 4.4(a), shows the markup in two colors of black and white. This is for the Epilog laser to be able to differentiate between sections in the markeup that are to be etched (rastered) and those that are to be left untouched. This color mapping feature in the Epilog laser is useful in setting up a design to run faster, and to assign the order of rastering on the chip. For example, the top plate has gas channels that have a different depth profile when compared to the base plate with the square trench. It is therefore, a very useful tool that

can be taken advantage of to obtain precise lasering. The thickness of each line and feature determines the action that is to be taken when the laser head encounters that feature's physical position on the acrylic board. For any rastered feature, a line thickness of 0.5" is chosen in the Adobe Illustrator and for gas and electrode ports that are to be cut out of the acrylic surface, and the final outlines of the chips separating them from the bulk of the acrylic board, a line thickness of 0.072" is chosen. Figure 4.4 shows screen shots of the Epilog engraving window, with color mapping, power speed and frequency settings. For a speed setting of 80% of full speed, and 75% of full power, a single pass creates a depth profile of 1 mil on an acrylic board of 1/8" thickness.

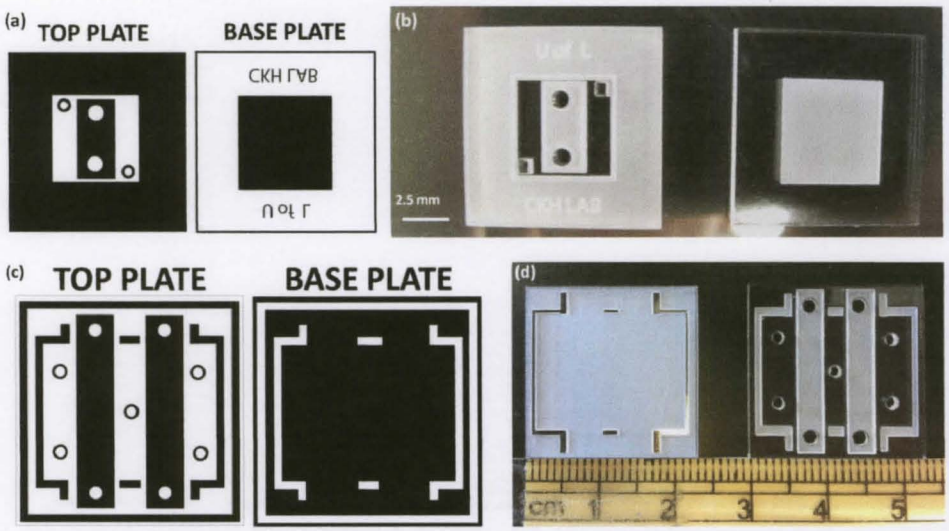

Figure 4.4. (a) Adobe illustrator markup for a single channel device (b) Actual device packaging made of acrylic (c) Illustrator markup for a dual channel device (d) The actual dual channel device

To obtain a smoother raster pattern, a 600 dpi (dots per inch) of laser rastering is chosen. This smaller spot size of the laser eliminates the formation of rippled or textured surfaces when creating gas flow channels. Figure 4.5 shows a collage of screen captures of the printing preferences when fabricating a sensor chip using a combined job (raster and vector cuts). These settings have been optimized following several combinations of

speed/power settings, so as to obtain the right dimensions of the gas channels and electrode ports. For example, a higher power (>75%) and slower speed (<50%), leads to wider channels as the laser stays longer at each dot location during the dithering, thus melting the acrylic. A much lower power (< 35%) and slower speed (<50%) fails to give the desired profile depth for the rastered feature. Multiple tries with different power and speed setting A completed raster step is followed immediately by a vector cut (in a combined job on the Epilog Mini) that separates the finished chips from the acrylic board (see Figure 4.4(b), (d)). Any residual fine debris in the channels (rastered sections) is removed and the chip thoroughly cleaned using pressurized air flow.

yielded a successful recipe shown in Figure 4.5.

Figure 4.5. Printing preferences chosen for a combined job on Epilog Laser

4.4 Graphene Transfer Process and Chip Packaging

Transferring as the grown graphene sheet from the metal substrate onto an insulating substrate is a crucial step towards realizing electronic applications. Different approaches have been broached regarding the transfer of graphene onto substrates. The use of polymer supports such as soft poly(dimethylsiloxane) (PDMS) stamps (59) and thermal-release tapes (111) (shown in Figure 4.6) that are attached to the graphene films grown on metal layers has gained been reported recently. Though this method facilitates transfer of large area graphene onto insulating substrates, it has certain limitations like defective transfer of monolayer graphene and the thermal release tape leaving residue onto the transferred layers. It has also been observed qualitatively from reports in literature (111) (126) that graphene transfer is much more uniform with lesser number of defects with PMMA as the support polymer when compared to either thermal release tapes or PDMS stamping. This argument is further strengthened by reports that show that graphene films transferred using PMMA exhibit the lowest sheet resistance (127) (128).

In the current work, as grown graphene on copper sheets are cut to size, keeping in mind the dimensions of the acrylic chip (10X10mm for single channel chip and 12X15mm for dual channel chip). Transfer is done by depositing a protective polymethylmethacrylate (PMMA) (Sigma-Aldrich) coating over the graphene.

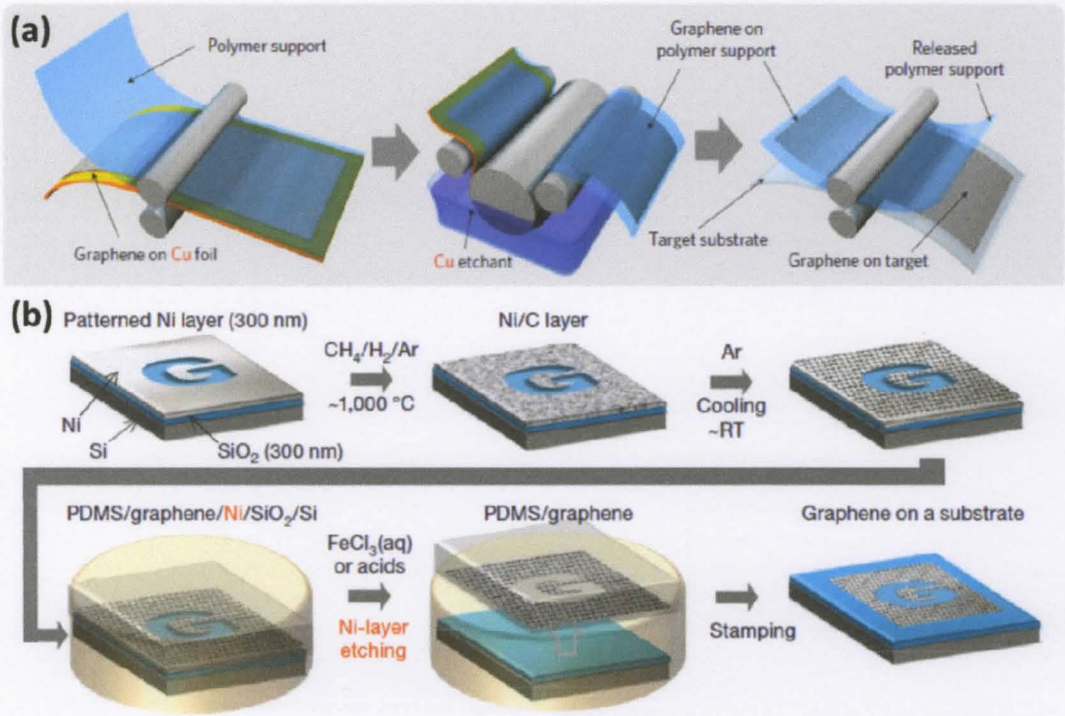

Figure 4.6. (a) Thermal release tape aided transfer of graphene onto polymer support (111) (b) Synthesis of patterned graphene films on Ni layers, etching using FeCl3 and transfer of graphene films using PDMS stamp (59)

This is done by spinning PMMA in two stages – 1000 rpm for 30 seconds followed by 700 rpm for 15 seconds in a spin coater (Chemat Technology – shown in Figure 4.8(b)), so as to deposit a uniform thin film of 1-3 (on the higher end) micron thickness on graphene. In the process of determining the ideal PMMA (by molecular weight and % solid) to obtain the desired film thickness, PMMA 495K (A4) and PMMA 950K (A4) were tested. Different spin speeds were tested and durable film thicknesses compared against existing literature (129) (shown in Figure 4.7)

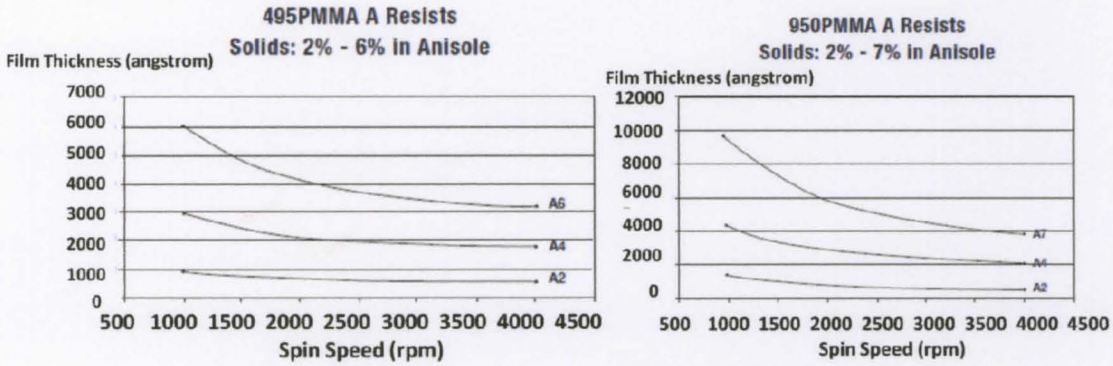

Figure 4.7: Spin speed versus film thickness curves for PMMA – two different molecular weights

From the obtained film durability, 950PMMA-A resist was chosen and spun as a thin film on as grown-graphene on copper pieces cut to size. Baking the PMMA + graphene on copper sheet at this stage at a temperature of 125°C for 5 minutes in Yamato DX 300 gravity convection oven (shown in Figure 4.8(a)), hardens the PMMA layer. This acts as the supportive backbone for the graphene layer upon etching the copper layer underneath it in ferric chloride (1:20 by weight $FeCl_3$ in H_2O) (112) (130). Ferric chloride is an efficient etching solution as it effectively removes the copper without any precipitation or toxic gaseous products (131). Once the copper is etched, a freestanding polymer-coated graphene layer is obtained. The progression of etching is shown in Figure 4.9. From this figure, it can be seen that there are a few air bubbles trapped between the graphene and etching solution interface. This leads to uneven etching of copper and can be remedied by gently transferring the floating graphene + PMMA sheet into a DI water rinse and then transferring it back into the etching solution so as to remove any residual copper that was not previously etched due to the presence of air bubbles. The PMMA + graphene on copper is transferred again to the DI water bath one last time to rinse away any residual etching solution before it is transferred onto an insulating substrate.

The transfer of graphene films is to be carried out with utmost care and diligence, as there is a high probability for the film to develop cracks during this process (as can be seen in Figure 4.10). One reason behind the development of cracks is that the metal (copper) undergoes significant reconstruction of its surface during the CVD growth step (127), leading to a rough surface. Graphene that grows on this surface tends to be influenced by the surface imperfections and retains them even after the etching of the copper is completed. Also, the appearance of folds on graphene during transfer leads to a change in the local stacking of graphene, i.e., 'folding' leads to local 'multilayer' graphene elements – also called as grafold. Due to this, the grafold exhibits electronic properties that differ from those of monolayer graphene (132). Therefore, to minimize the risk of wrinkles during transfer, good adhesion needs to be established between the substrate and the graphene film being transferred. This can be done by maintaining good control over the hydrophobicity and surface roughness of the substrate material. In the current work, for the single channel device, graphene is transferred onto a thin film of PDMS (Dow Corning Sylgard 184, mixed in 10:1 base to catalyst ratio) that is spun onto a glass slide (at 1000 rpm for 20 seconds) using a PDMS spinner (WS-400B-6NPP-Lite, Laurell Technologies Corp, shown in Figure 4.11(b)).

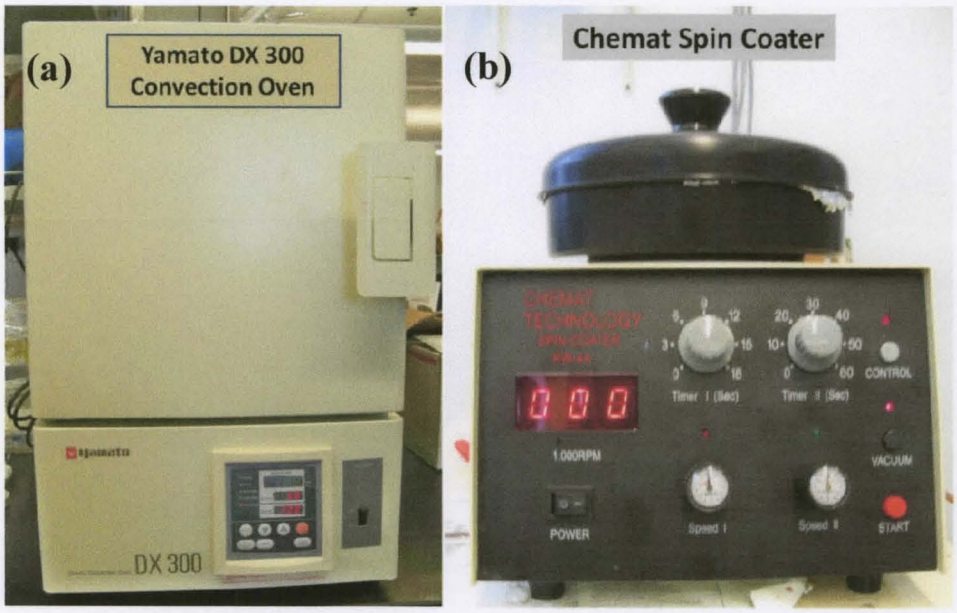

Figure 4.8: (a) Yamata DX oven (b) Chemat spin coater used for spinning PMMA film on graphene on copper

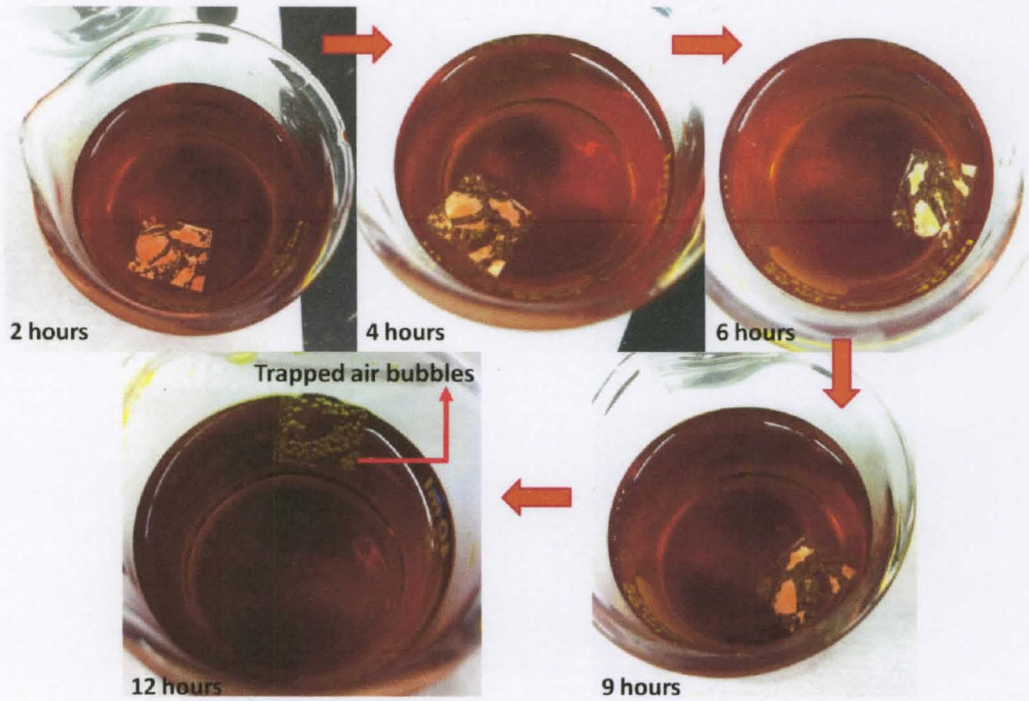

Figure 4.9. Progression of copper etching process over a 12 hour period

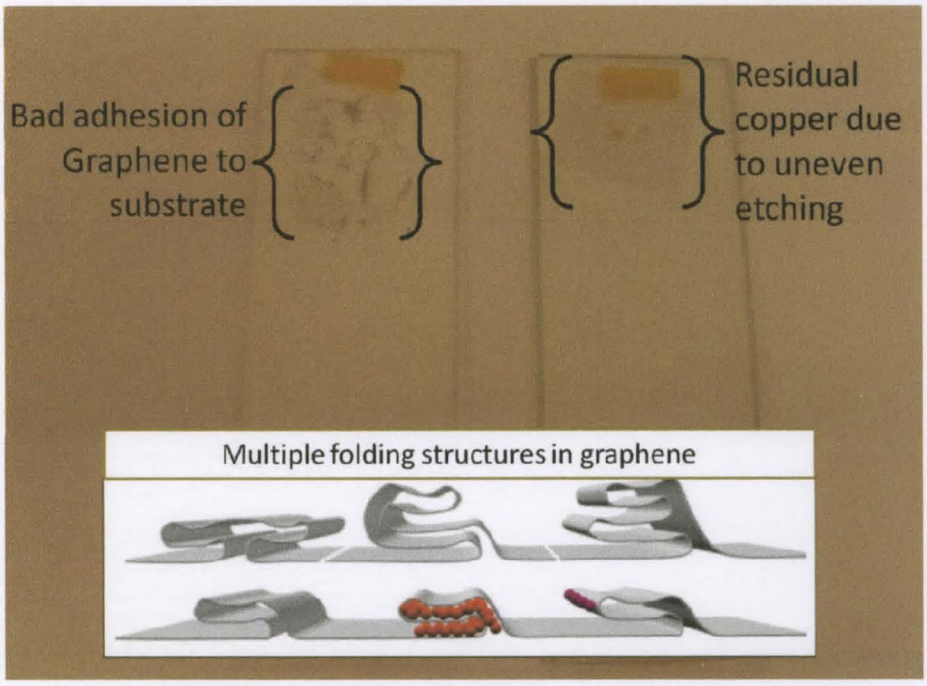

Figure 4.10. Two samples showing bad adhesion of graphene to the substrate and uneven etching of copper. Inset (132) shows various complex folds that can be formed in monolayer graphene.

The inclusion of a PDMS thin film is a necessary step as washing the PMMA off the transferred graphene involves an acetone wash which is detrimental to the acrylic substrate being used here. In the case of a dual channel device, a 3mil thick Mylar sheet (McMasterCarr) is chosen as the support substrate (explained in detail in Chapter V). Briefly, Mylar is a transparent polyester film (BoPET: Biaxially-oriented polyethylene terepthalate) made from stretched polyethylene terepthelate or PET. It has attractive characteristics like being electrically insulating and has gas barrier properties and good chemical stability. Much like when transferring onto PDMS thin film, good adhesion is to be maintained in case of Mylar. Pre-treatment of the Mylar film, in addition to regular cleaning in acetone and isopropyl wash, is carried out in air plasma cleaner (Harrick Plasma Cleaner PDC–002, see Figure 4.11(a)) for 30 seconds. This greatly increases the

wettability of the Mylar surface and therefore the adhesion of the graphene film to the Mylar sheet and is shown as an inset in Figure 4.12 (133) depicting the entire transfer process. The graphene monolayer that is transferred onto either PDMS or Mylar with the help of a thin PMMA backlayer has a thin film of residual water from the DI wash. It is imperative that this water layer is removed, so as to increase the contact area of graphene with the substrate. Additionally, any microscopic air bubbles that are also trapped can be eliminated, reducing the appearance of wrinkles or cracks in the subsequent steps. To carry out this step in a thorough manner, the substrate (with the transferred graphene) is heated to 125 °C in the Yamato DX convection oven for 5 minutes.

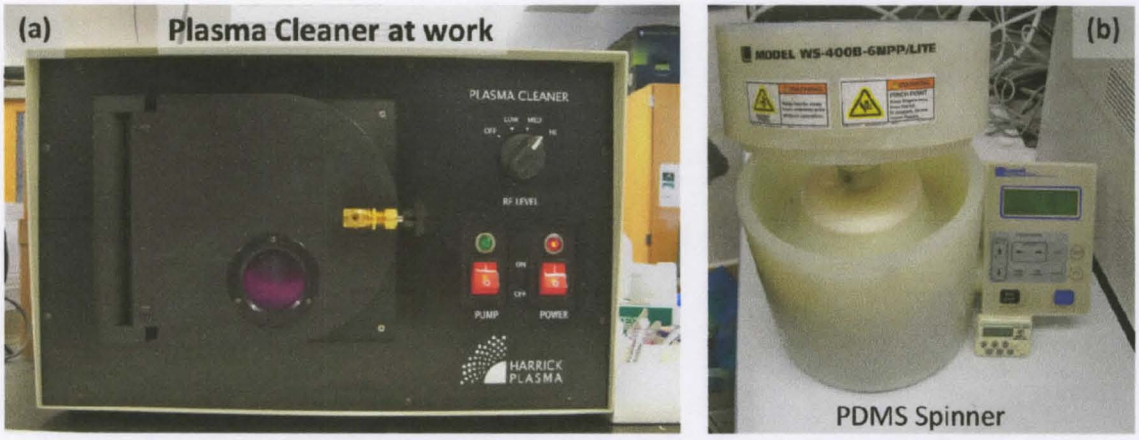

Figure 4.11. (a) Plasma ignited inside Harrick Plasma cleaner (b) PDMS spinner

The second baking step lends certain hardness to the PMMA 'backbone' and therefore has to be softened before it can be washed away. This is to reduce the strain on the underlying graphene layer during the PMMA removal step. PMMA is among the several solvents that can dissolve it efficiently. Therefore, a few drops of PMMA is dropped onto the hardened layer and left to dissolve it at room temperature for approximately 10 minutes, succeeding which, it is washed away in a heated acetone bath (at 60 °C). This is

followed by a rinse with room temperature Isopropyl alcohol (IPA) at room temperature. These rinses are repeated a couple of times until the PMMA is completely washed away and the graphene layer is left adhered to the support substrate. Once transferred, monolayer graphene is difficult to image using an optical microscope on most substrates. It can however be made out faintly against a background, as a slightly discolored section on a PDMS or Mylar substrate, as shown in Figure 4.13(a) and (b) respectively. A better profile of the transferred graphene is obtained by Raman characterization.

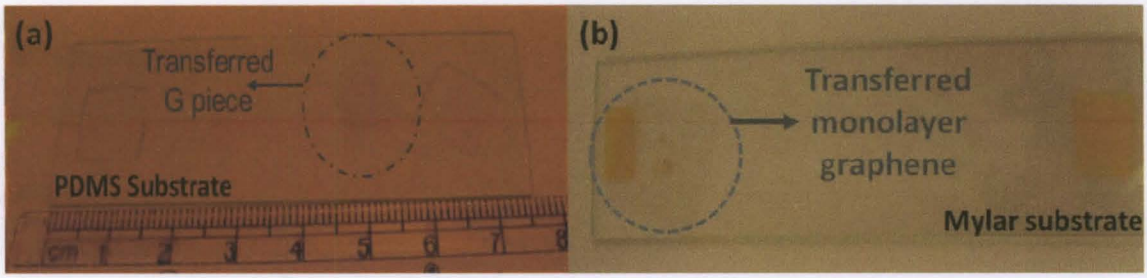

Figure 4.13. (a) Optical image of graphene transferred onto PDMS thin film (b) Optical image of graphene transferred onto Mylar support substrate

4.4.1 Raman Characterization of Transferred Graphene Samples

Raman spectroscopy is well know to involve minimal sample preparation and handling during analysis. This non-destructive method of identifying fingerprints of single, bi and multilayer graphene is an essential tool where graphene is transferred onto arbitary substrates for various applications. A comparitive study of raman spectra of the as-grown graphene with that transferred onto both PDMS and Mylar is shown in Figure 4.14. This details the spectra obtained for graphene grown on copper (control), graphene after transfer onto PDMS thin film and the spectra for plain PDMS thin film (control). From the obtained data, it is seen that the as grown graphene exhibits the G band at ~1580cm^{-1}

and the G′ band at ~ 2640cm^{-1}. In comparison, the transferred graphene shows the bands shift – with the G band at ~ 1584cm^{-1} and the G′ at ~2658cm^{-1}. This upshift can be attributed to the sensitivity of graphene to substrate charge transfer doping , where the effects are similar to those seen in electrochemical doping (refs). From the Figure, it is seen that the D band is conspicuosly absent (usually occuring around ~ 1350cm^{-1}), confirming that no significant defects are present in the transferred graphene sheet.

A similar analysis is carried out on the graphene layer that is transferred onto an optically transparent 3mil Mylar sheet. In Figure 4.15, a plain Mylar sheet is characterized so as to serve as control, along with the as-grown graphene on copper (insert into plot) for comparison against the transferred graphene sheet. The G band is seen to occur at ~1584cm^{-1} and the G′ at ~ 2661cm^{-1}. Any extranous dominant peaks can easily attributed to the Mylar sheet supporting the graphene layer. The most dominant Mylar peaks occur at ~1294cm^{-1}, 1614cm^{-1}, 1728 cm^{-1}, 3086cm^{-1}. After characterizing the transferred graphene sheets, the next step entails cutting the sheets (PDMS/Mylar) to size and transferring onto the acrylic base plate of the chip to start packaging (Refer to Figure 4.3).

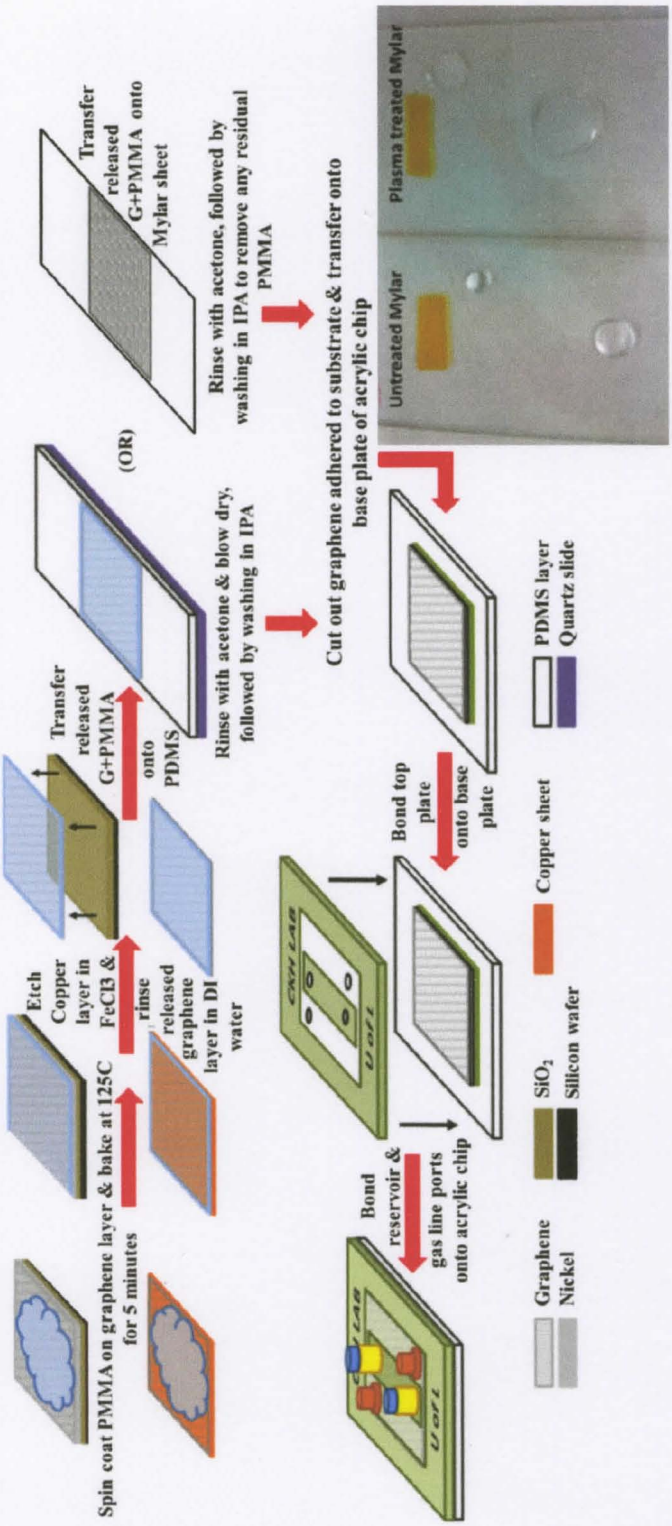

Figure 10. Schematic depicting transfer of graphene from Ni/Cu onto PDMS/Mylar support substrate followed by device packaging (9)

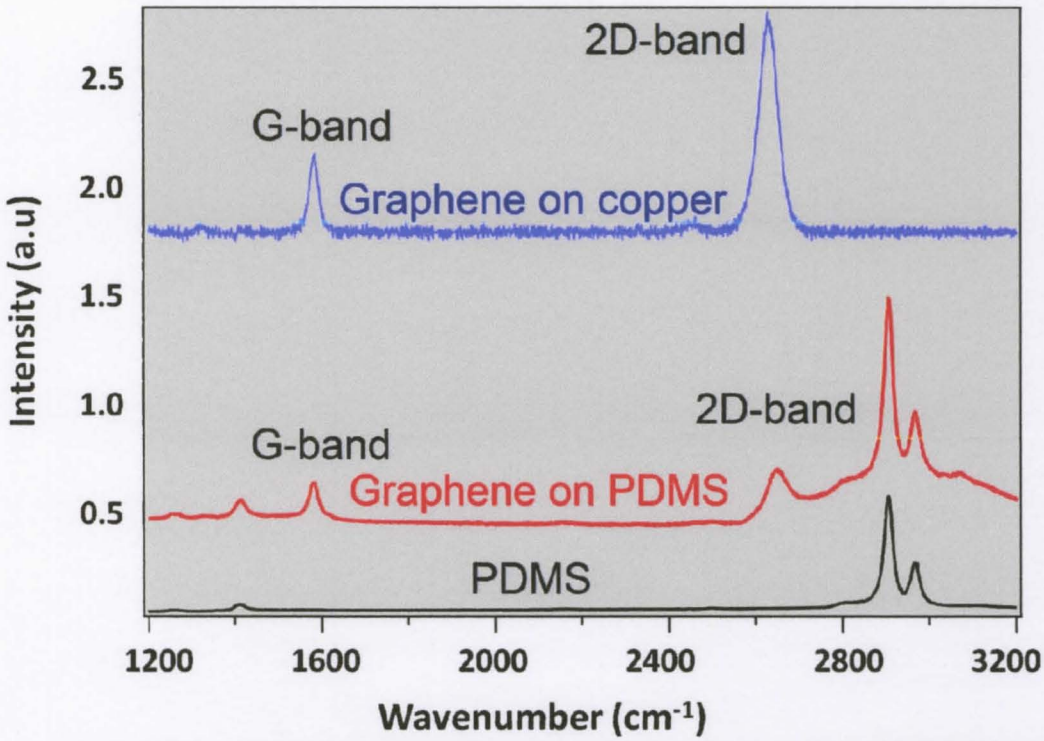

Figure 4.14. Raman Spectra comparing graphene transferred on PDMS with controls

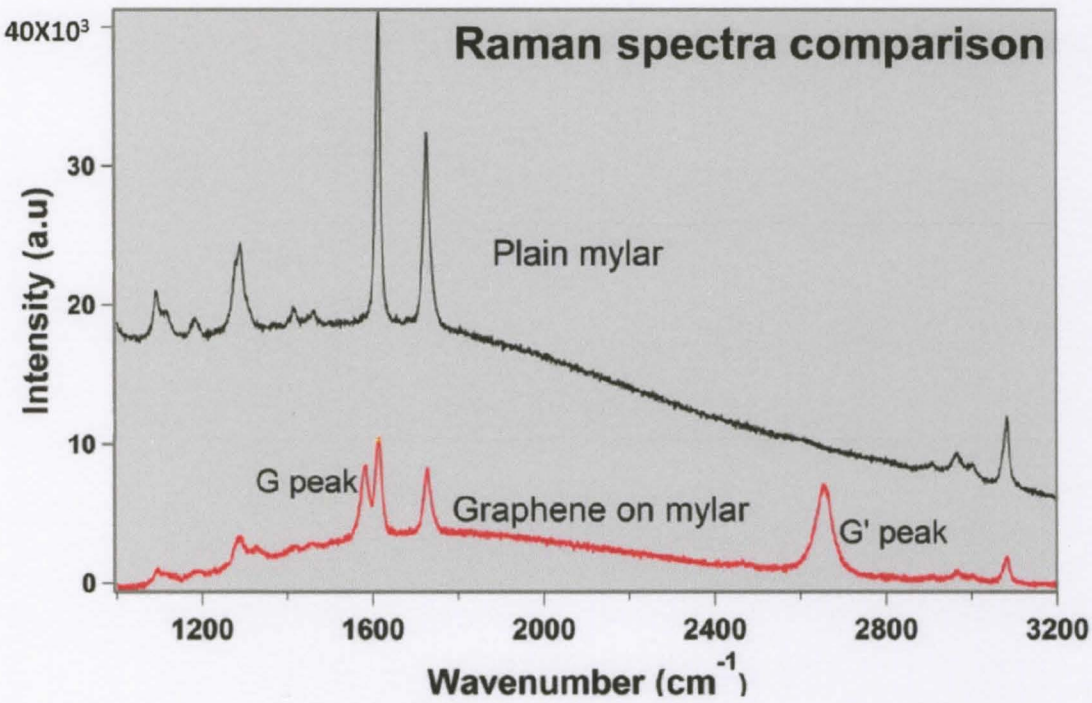

Figure 4.15. Raman spectra comparing graphene transferred onto Mylar with control

4.4.2 X-ray photoelectron spectroscopy

The physical and chemical composition of a material's surface plays a role in its interactions, influencing its adhesive properties, wettability, contact potential, catalytic activity, corrosion rates and failure mechanisms (134). X-ray photoelectron spectroscopy (XPS) is a spectroscopic technique that is capable of quantitatively measuring the elemental composition on the surface of a material, its empirical formula, the chemical and electronic state of the elements present in the sample, their spatial distribution and the uniformity of the composition of the material among others.

XPS working principle: A sample surface is irradiated with x-rays in an ultra high vacuum environment. When an x-ray photon from the x-ray source (either Al Kα or Mg Kα) hits the sample surface, it transfers the energy to the material's core level electron, leading to an electron emission. This kinetic energy of emission is a direct function of the binding energy of the originating atomic orbital of the electron as well as the incident x-ray energy. Analysis of the intensity and associated energy spectrum of the electrons emitted from the surface therefore enables identifying and determining the elemental composition of the sample's surface (135).

XPS analysis: This section reports the XPS measurements performed on a sample of graphene monolayer transferred onto a mylar substrate and mounted on copper stubs. The x-ray excitations source used was Al x-ray source (work function of 8.64) and the measurements were carried out in a custom assembled photoelectron spectroscope. A low resolution survey scan shown in Figure 4.16 establishes the presence of Carbon, oxygen

and copper. In such low resolution, individual peaks are usually quenched. To be able to determine the individual elements and their compositions, high resolution scans must be carried out. Figure 4.17 shows a high resolution scan targeting the Binding energy (BE) range of 280-296 eV. A single element usually produces 1-20 peaks in a high resolution scan, depending on the sample's surface composition. In the current sample, the raw wave (red) is deconvoluted to realize 3 individual peaks and the corresponding energies of carbon peaks are analyzed (Figure 4.17).

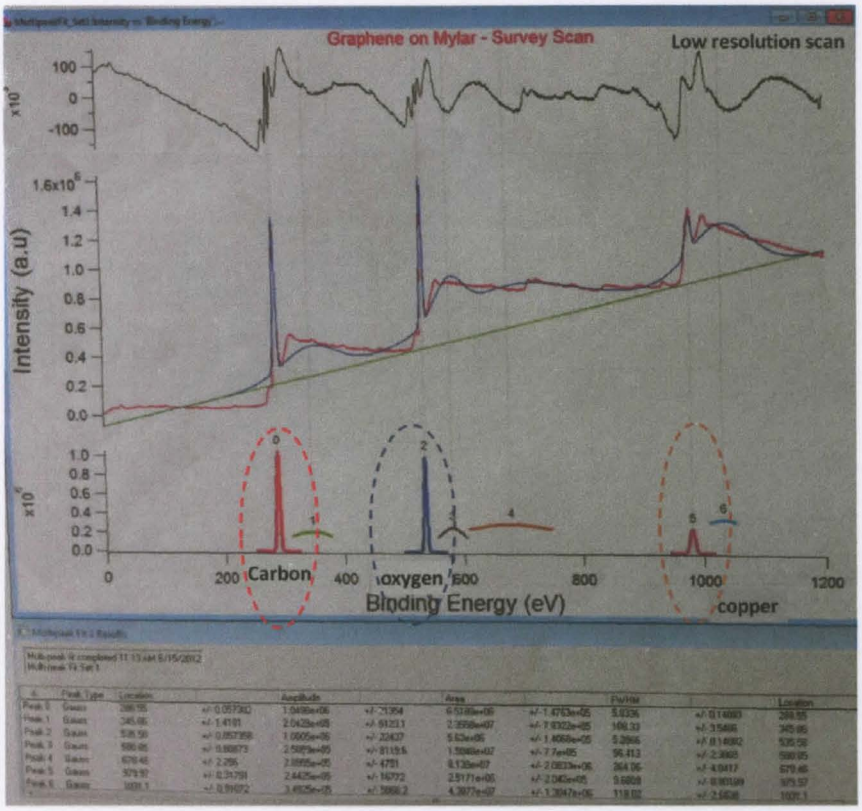

Figure 4.16. Low resolution survey scan showing presence of carbon, oxygen and copper

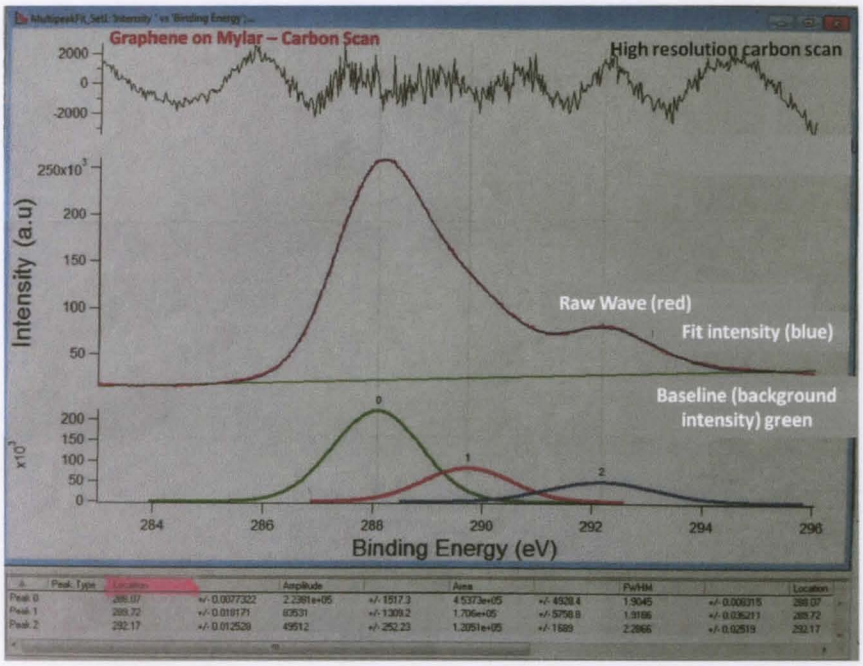

Figure 4.17. High resolution scan showing with deconvoluted carbon peaks

XPS is a technique that is also used for depth profiling of the samples and is capable of retrieving surface information to a depth of approximately 10nm. As the graphene sheet in the current sample is only one atom thick, and is supported on a mylar substrate, electron emission from the surface is expected to include those from both the graphene as well as the mylar substrate. To identify the carbon signal coming from each of these surfaces, an oxygen scan (high resolution) is also performed. This is to be able to eliminate the carbon signal from the C=O and C-O-C=O bonds present in mylar. Figure 4.18 shows a high resolution scan with deconvoluted oxygen peaks. From Figure 4.17, it can be seen that the peak 0 at 288 eV and peaks in Figure 4.18 correspond to the mylar's carbon and oxygen content (136). The slight shift in the binding energy could be from oxidation of the sample.

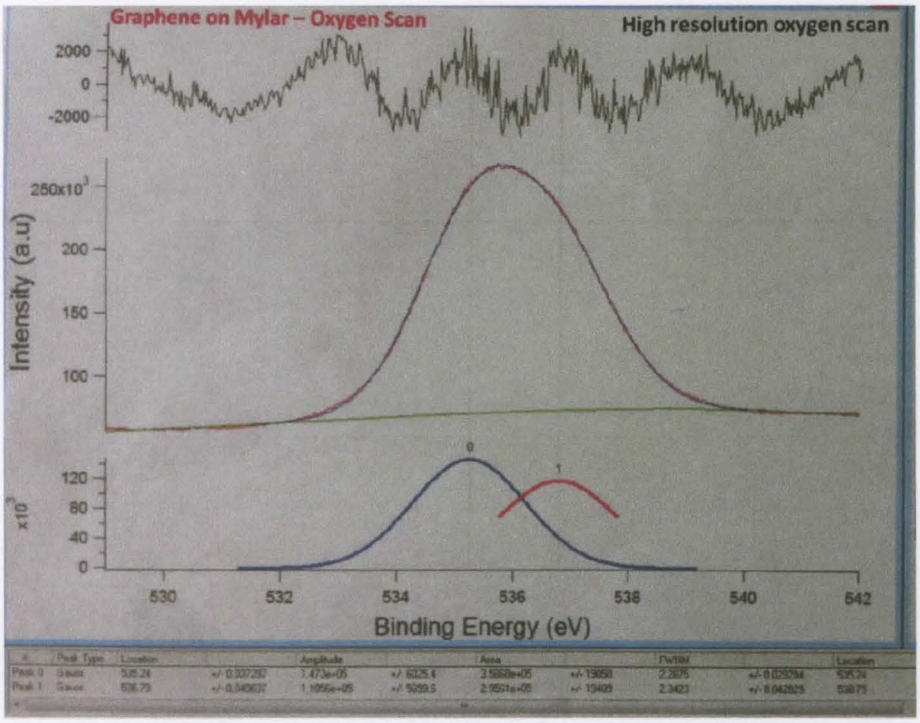

Figure 4.18 . High resolution survey scan showing deconvoluted oxygen peaks

XPS analysis is also useful to determine the presence of trace amounts of copper left on the graphene sheet after the copper etch and transfer onto the mylar substrate. To accurately determine this, a control scan is carried out where the graphene on mylar sampel is mounted directly onto the substrate holder in the XPS system (copper stub). This control scan of the sample on an exposed substrate holder is shown in Figure 4.19. Upon deconvoluting the raw wave, several peaks of varying energies are found to be present. This however is an expected result – as the sample stub as well as the walls of the surrounding chamber are made of copper. To substantiate the copper electrons sourced from the XPS chamber as being the source of a majority of these peaks, a second scan is run on the sample after mounting it on a covered stub. This eliminates the effect of immediate exposure of the copper stub to the x-ray source and minimizes the number

of peaks in the scan. Figure 4.20 shows the high resolution scan obtained from the graphene on mylar sample showing residual copper present.

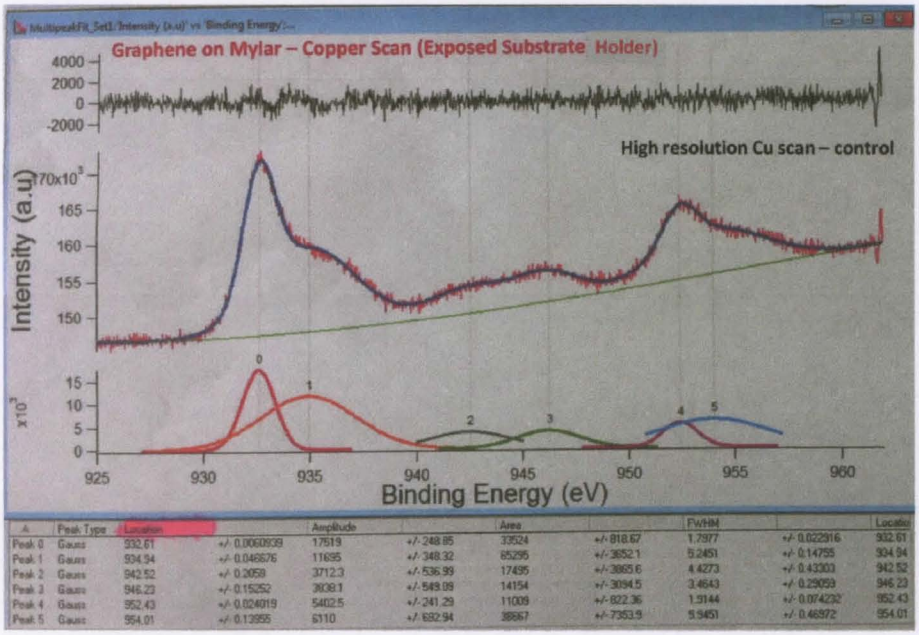

Figure 4.19 . High resolution scan showing deconvoluted copper peaks – control scan

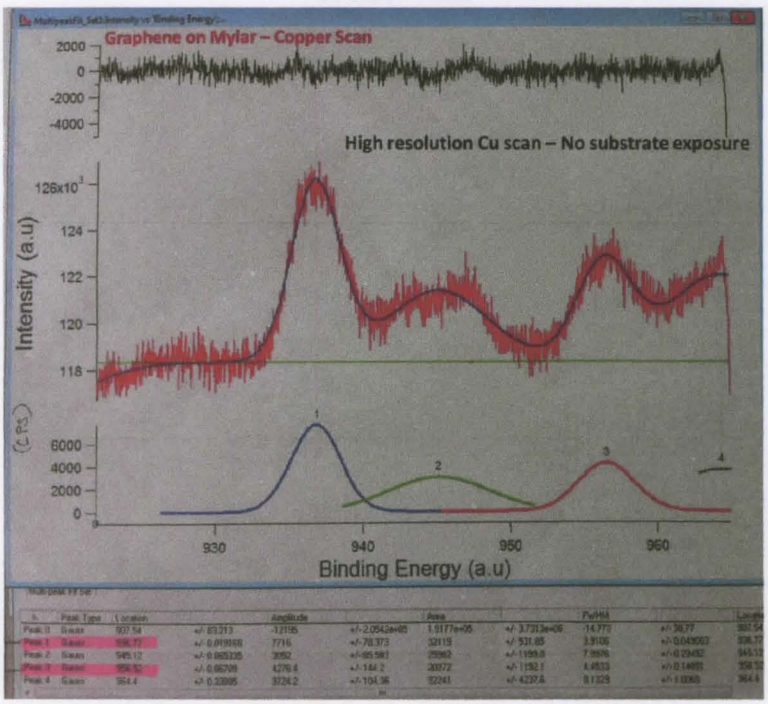

Figure 4.20 . High resolution scan showing deconvoluted copper peaks – confirming presence of copper on sample

This is in agreement with existing literature which shows that trace amounts of copper is present on graphene following etching and transferring onto a substrate unless the sample is subjected to a rigorous regime of RCA cleaning (137) usually used in Si wafer cleaning techniques in semiconductor manufacturing facilities (138)

4.5 Device Packaging

The sensor chip packaging involves bonding the top and base plates together under slight compression at a temperature of 125 °C in a Yamato convection oven for one hour, which seals the raised portions of the top and base plates together, creating enclosed shallow gas channels traversing the length of the graphene layer. Figure 4.21 shows cross sectional views of bonded sensor chips. Gas and electrode ports (Small Parts Inc.,) are then bonded onto the chip using 3M Scotch-Weld Epoxy adhesive. Schematics detailing the single/dual channel packaged devices and the gas inflow/outflow and electrode ports are shown in Figure 4.22 (133).

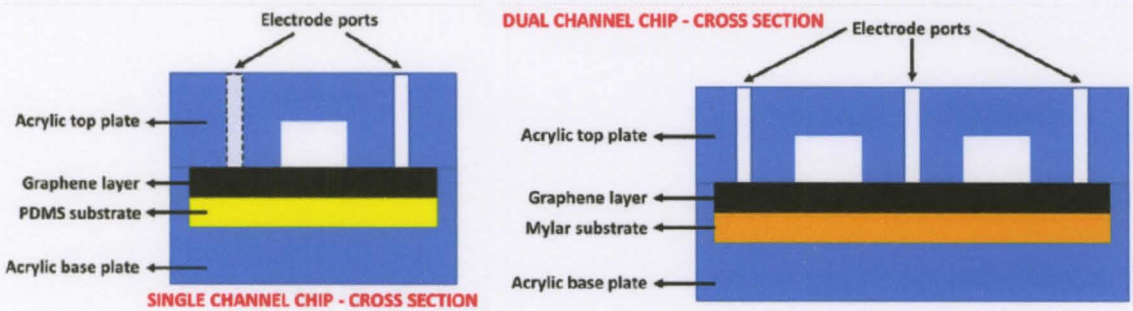

Figure 4.21: Cross sectional views of sealed acrylic chips

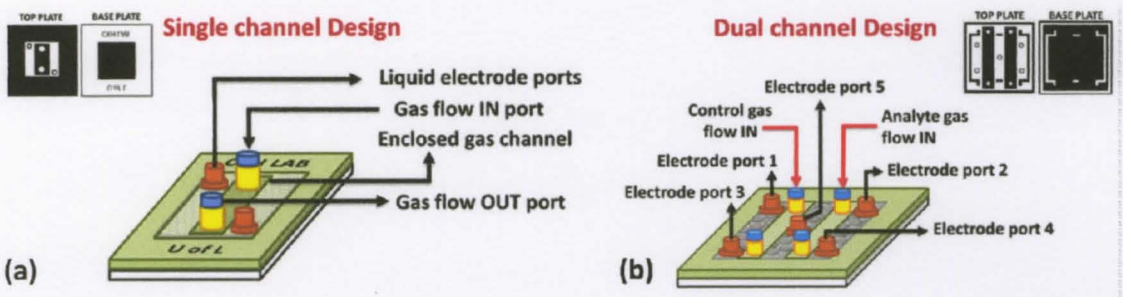

Figure 4.22: (a) Schematic detailing the layout of a single channel device design (b) Schematic of dual channel device, with gas ports over two separate channels; insets shows the original blueprint of the device (133)

An acrylic board of 12X12″ on average yields a total of 80 sensor chip packages, bringing the total cost of each individual chip to ~$2. Figure 4.23 shows the packaged sensor chips (133).

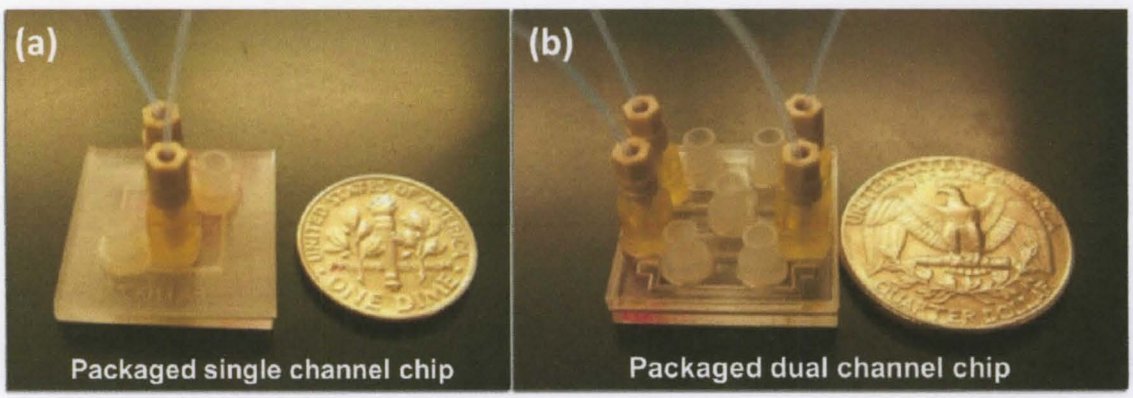

Figure 4.23. (a) Packaged single channel device with a small footprint (b) Dual channel device packaged in acrylic

For the packaged devices, the single channel devices have a gas flow channel of 500μm depth profile, 3mm wide and 8mm in length. The dual channel devices on the other hand, have gas flow channels dimensions of 500μm depth profile, 3mm wide and 18mm length.

The electrode ports are bores of 2mm diameter. The experiment setup is discussed in the following sections.

4.6 Experiment Setup

The experiment setup nitrogen gas (N_2-Welder's Supply) that is used as a purging environment for the sensor between vapor exposure cycles. It is also used as the carrier gas for introducing the organic solvent vapors into the sensor environment. To facilitate this dual purpose, the experiment setup involves two separate gas flow lines – the purge line and a bubbler line. The gas flow lines are all connected with 1/8" steel tubing to ensure uniformity and to minimize pressure drops along the line. Appropriate valves (UpChurch-IDEX) have also been chosen that isolate the purge line from the target gas lines. Figure 4.24 shows a schematic of the experiment setup.

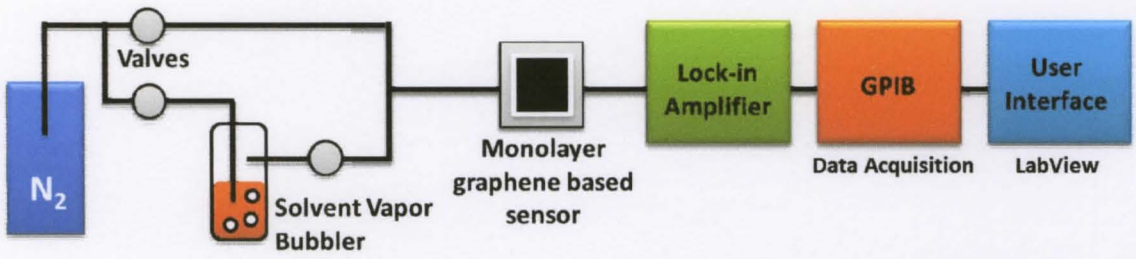

Figure 4.24: Schematic showing setup for carrying out experiments

The organic solvent vapors are introduced into the sensor system via a carrier gas (N_2) that flows through a mini bubbler (shown in Figure 4.25). Different volume concentrations of the organic solvents (ethanol (CH_3CH_2OH), methanol (CH_3OH) and isopropyl alcohol or IPA ($(CH_3)_2CHOH$) have been tested using this setup.

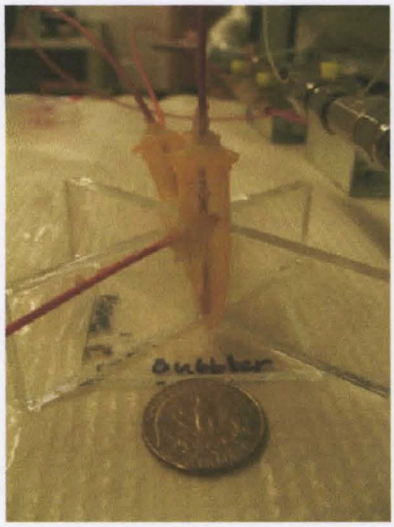

Figure 4.25. Mini bubbler used to bubble organic solvent vapors into sensor environment

PTFE (Polytetrafluoroethylene) tubes (Small Parts Inc.,) with an outer diameter of 30mil and an inner diameter of 10mil connect the bubbler to the sensor. These gas lines are inserted into the gas ports previously bonded onto the acrylic chip using finger tight ports that make a seal and prevent the purge/analyte gas from leaking. The electrode ports are filled with KCl solution of 100mM and platinum (Pt) electrodes (Omega Engineering) are dipped into the ports. Connections from the sensor are made to a Lock-in amplifier, thus completing the circuit through the sensor.

Lockin Amplifier

A Lock-in amplifier is capable of detecting and measuring very small AC signals, even in presence of noise. In the current setup, an SRS 830 DSP amplifier (Stanford Research Systems, Inc) is used to carry out the AC measurements.

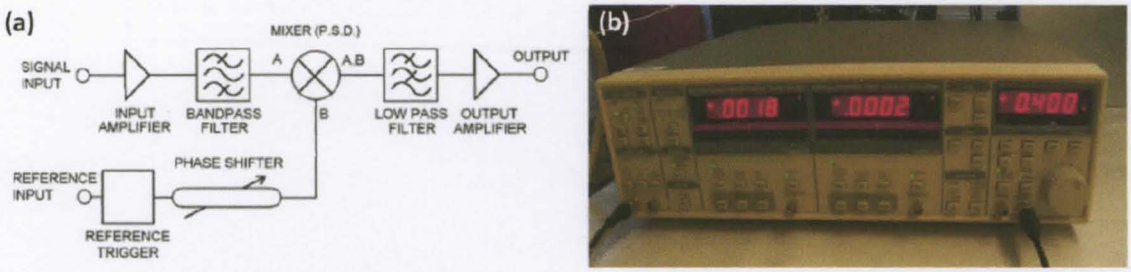

Figure 4.26: (a) Block diagram of a lock-in amplifier (157) (b) SRS 830 Lock-in amplifier

Figure 4.26 (a) shows a typical lock-in amplifier's block diagram, whereas Figure 4.26(b) shows the SRS DSP Lock-in amplifier used in the experiment setup currently being described.

General Purpose Interface Bus (GPIB)

GPIB is a standard, high speed interface for communication between instruments and controllers from a multitude of vendors and is widely used in a variety of industrial applications (139). It provides high reliability and an increased productivity, saving time and reducing costs. Figure 4.27 shows the GPIB communication setup used in the current experiment setup, where an IEEE 488 cable transmits communication between devices – the GPIB PCI card installed in a computer and the SPS830 Lock-in amplifier. LabVIEW provides the interface to the GPIB PCI card and is used to collect, analyze illustrate and write the collected measurements into data files.

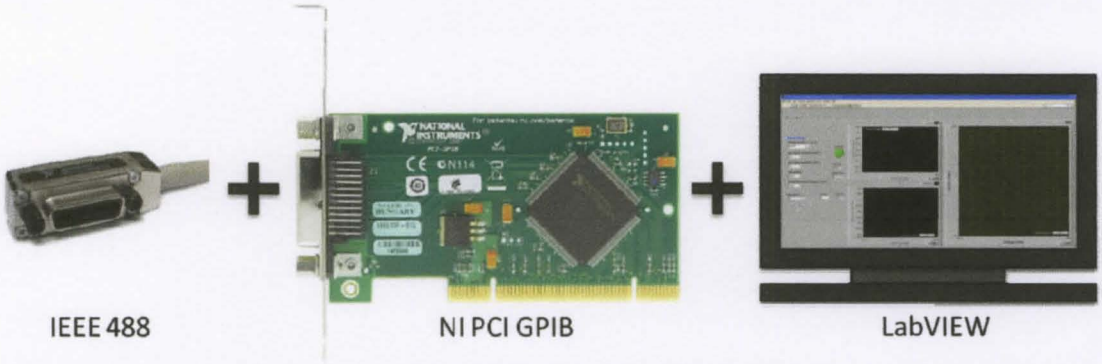

Figure 4.27: GPIB communication setup

LabVIEW Program

National Instruments, which is the creator of NI LabVIEW, describes this highly flexible programming environment as (140)

> "A system design software that provides engineers and scientists with the tools needed to create and deploy measurement and control systems through unprecedented hardware integration."

Taking advantage of this LabVIEW development environment, a custom program has been built that acquires the data from the Lock in amplifier via the GPIB card and graphically illustrates the sensor response on its front panel. A user can also control the Lock-in Amplifier via the front panel. Figure 4.28 shows the front panel with the user control tabs for reference voltage i.e., input voltage, the internal frequency. Current, resistance waveforms plotted versus time (in seconds) and a secondary current vs. voltage waveform (IV curve) are also placed in this panel. The inset in the figure shows the second tab control with the sensitivity and reserve signals and a drop down menu to select the input connections. The block diagram associated with this front panel is shown in Figure 4.29. In Figure 4.28, a HOLD option shown as a green lit LED can be seen on the front panel. This is included in the block diagram (in a loop) so as to allow the output value to stabilize after each reading before recording that value as a data point. This

(adjustable) delay is taken into consideration while building the waveform to plot the current and resistance readings vs. time in the waveform. The voltage and current readings obtained from the sensor are used to calculate the corresponding resistance values and fed into an array that plugs into the output waveform that shows the dynamic changes in the sensor response when it exposed to the target vapors. This array plugs into a secondary loop that houses the final data (at the end of N (number of steps specified) loops) and prompts the user to Save the file. This custom written LabVIEW program is designed to facilitate easy switching between single ended and differential voltage measurements and the results from these shown in the succeeding chapter V.

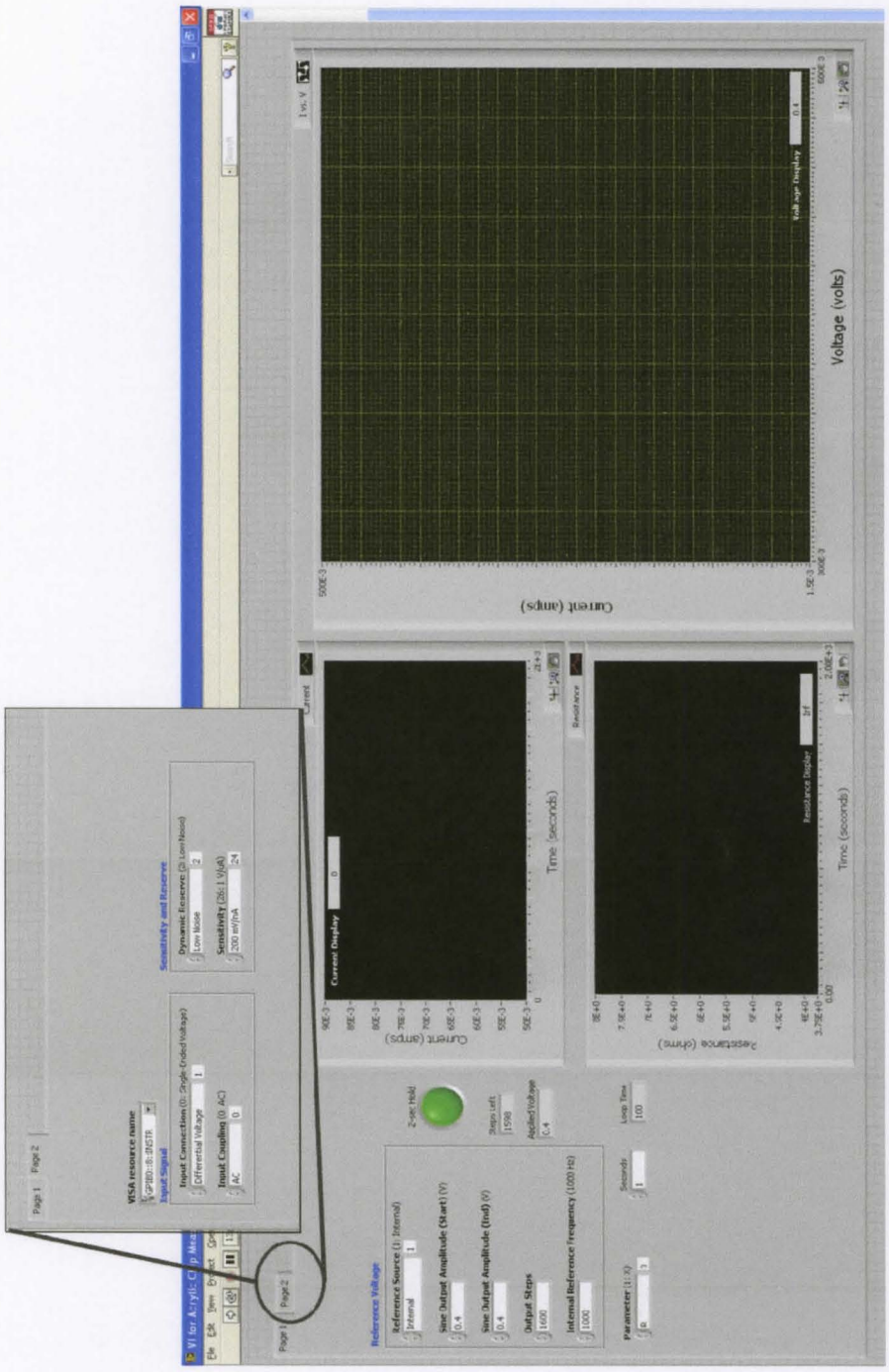

Figure 4.28: LabVIEW Program Front Panel

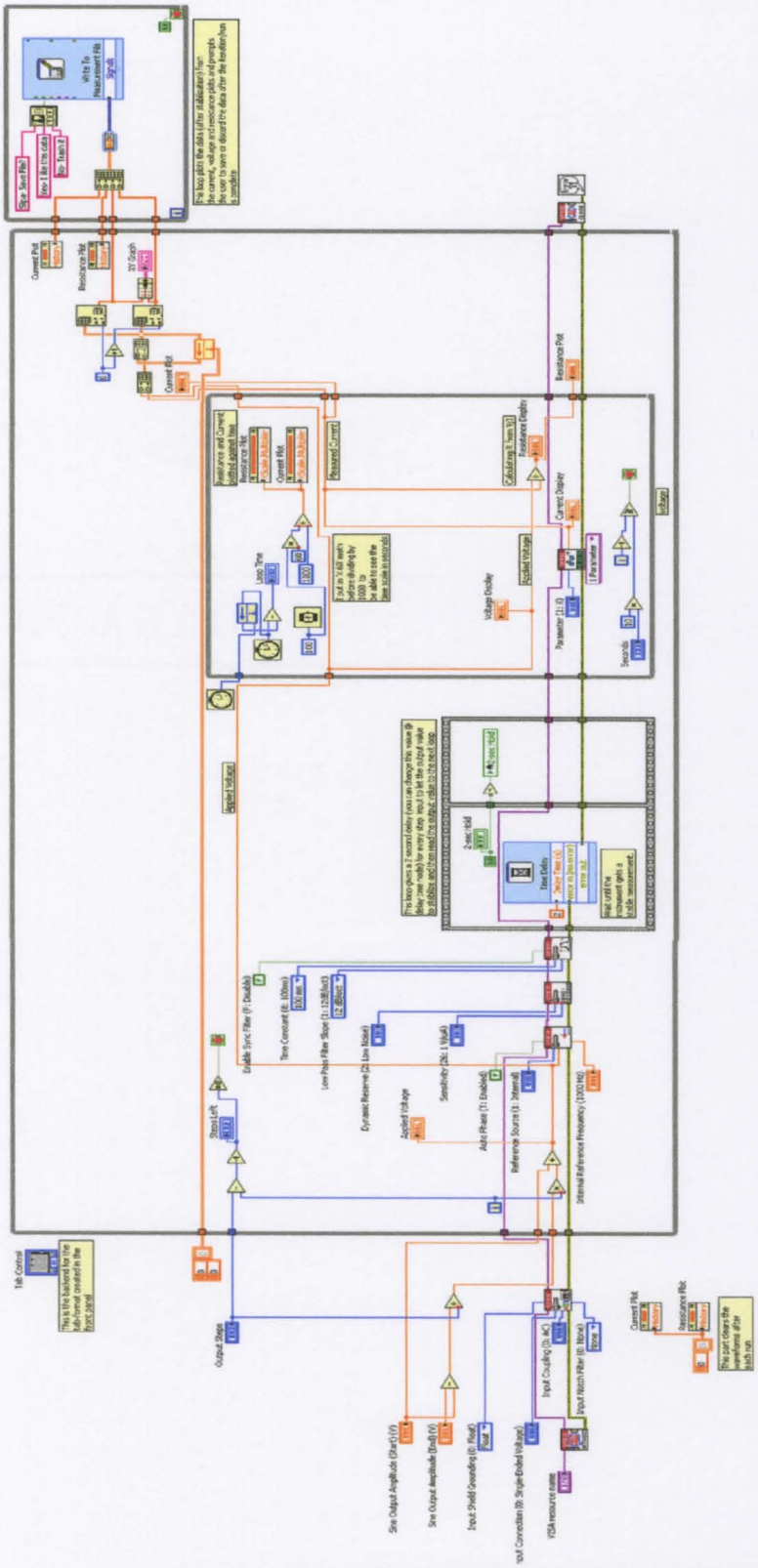

Figure 4.29: LabVIEW Program Block Diagram

4.6.1 Single channel device – single ended voltage measurements

Sensor response from the single channel device is tested by flowing the purge gas and analyte gas (different concentrations) through the channel in alternate cycles. A constant voltage of 400mV is applied to one of the electrode ports, with reference to the other, at a frequency of 1KHz. The graphene sensing layer that is extremely conductive completes this circuit and has resistance R_1 in a nitrogen environment. When the purge cycle (N2 flow only) switches to the analyte gas cycle, the graphene layer registers a change in its resistance as R_2. These cycles are alternated with different concentrations of the analyte vapors flowing through the sensor and the corresponding change in resistance of graphene is plotted. From the obtained data, the sensitivity, response and recovery times of the sensor in the presence of these analyte gases are plotted.

4.6.2 Dual channel device – differential voltage measurements

Differential voltage measurements are highly efficient in reducing noisy signals. By referencing the lock-in signal to ground (center port) and identifying two (one each with respect to the purge/analyte gas channels) as the voltage inputs (400 mV) , the voltage difference between the two signal output electrode ports is recorded. Figure 4.30 shows the equivalent resistances between the electrode ports. Promising results from the single channel device have led to the designing of differential voltage measurements on the sensor chip. However, it was observed that on modifying the design to accommodate two channels (instead of one) brings cross-talk between the channels.

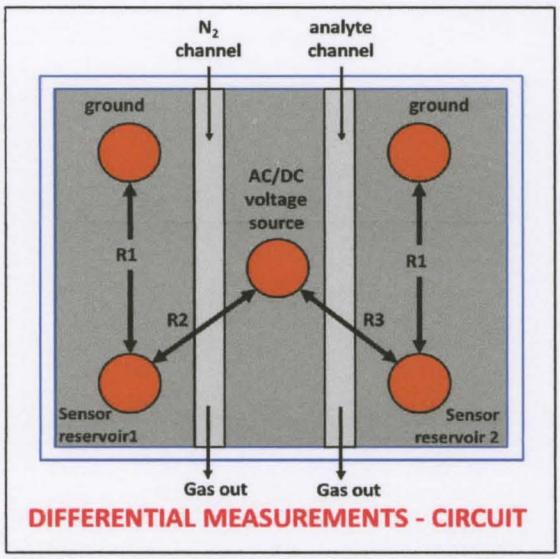

Figure 4.30. Dual channel device- differential voltage measurement setup

By making a cross-sectional cut through the device and perusing under an optical microscope sheds light on the cross-talk occurring in the devices. Figure 4.31 shows an optical microscope image of the device cross-section. This shows that the underlying support for the graphene layer-PDMS is permeable in nature.

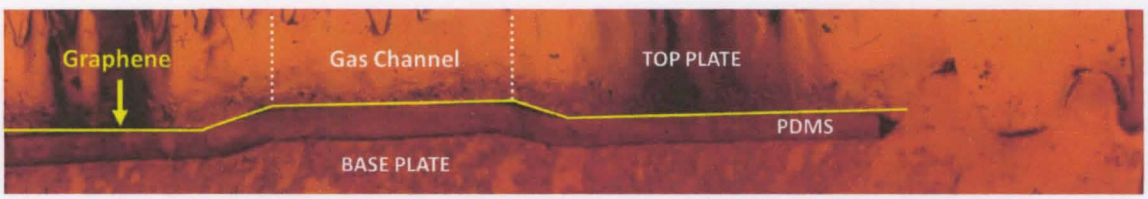

Figure 4.31. Optical microscope image of dual channel device cross-section

Hence, the purge gas from the reference channel bleeds into the analyte gas in the test channel. Reducing the thickness of the PDMS layer to less than 10 μm (threshold for safe handling without crippling the graphene layer) fails to eliminate the cross talk. Therefore,

a gas-impermeable layer is introduced as the support substrate for graphene – namely Mylar. These modified devices are used to carry out the differential voltage measurements at constant 400mV input voltages and the devices responses are tabulated and plotted Results from these devices are shown in Chapter V

4.6.3 Patterned gold electrodes

Differential voltage measurements carried out in the previous section establish the sensor device's vapor detection limit and the sensitivity (see Chapter V). To improve on these parameters and carry out comparative studies, gold electrodes are patterned onto the device's top plate. Figure 4.32 shows a schematic of a mylar stencil mask (mask made using Epilog Mini Laser) over an acrylic top plate.

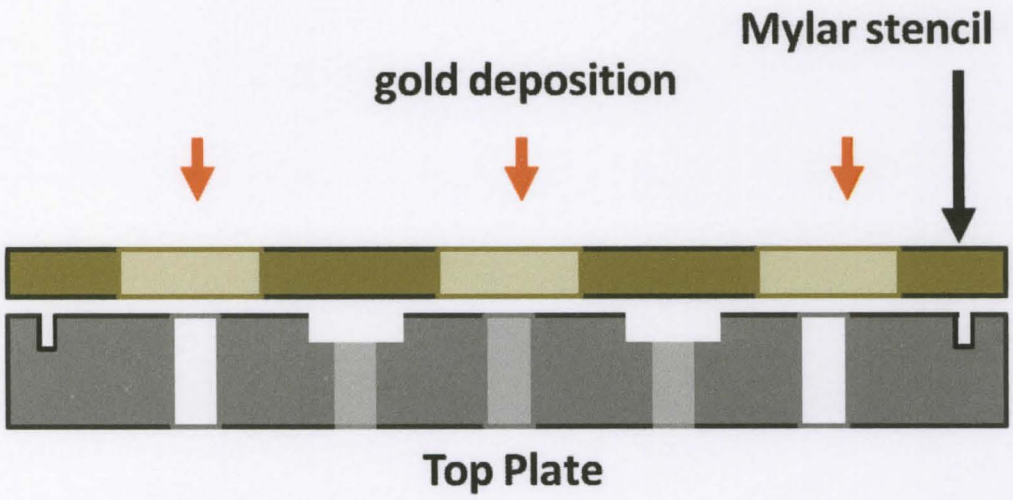

Figure 4.32. Schematic showing mylar stencil over acrylic top plate for gold electrode patterning

The mylar stencil accommodates electrode ports slightly larger than the dimension on the top plate – so as to deposit a 'lip' of gold around the electrode port. This leads to a larger contact area of the electrode with the graphene layer during bonding.

Sputtering is carried out for 30 seconds with Ti and 1 minute gold using DC power at 300 watts in the presence of argon at 5mTorr pressure. This yields a gold layer of approximately 50nm thickness over the top plate.

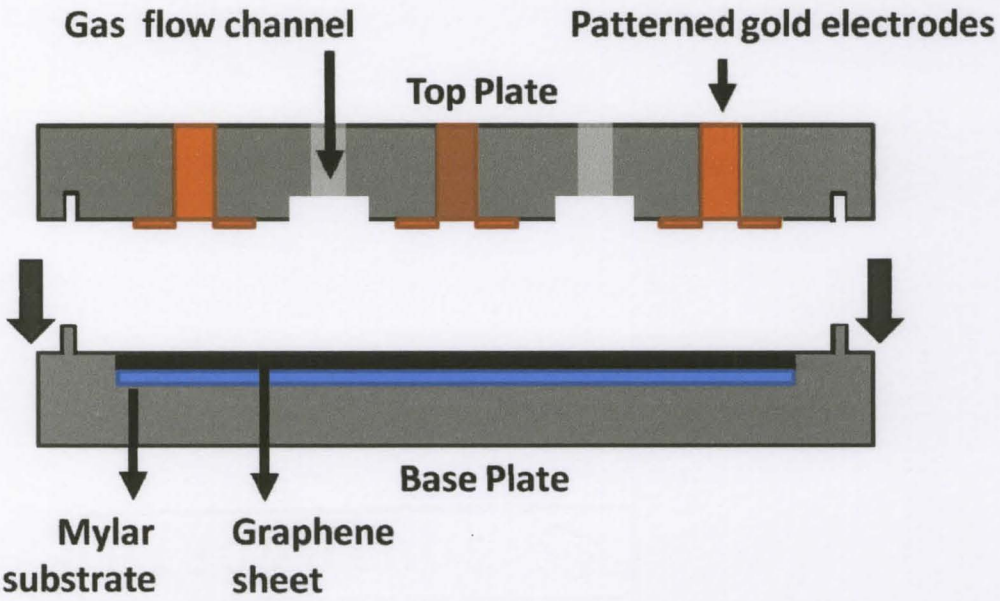

Figure 4.33. Schematic showing bonding of top plate with patterned gold electrodes with base plate

Figure 4.33 shows a schematic of an acrylic top plate of a dual channel device with patterned gold electrodes (ready to bond to base plate) while an optical image of the same is shown in Figure 4.34. The top and base plates are bonded together in Yamato DX oven at a temperature of 125 ^{o}C for one hour and allowed to cool down. This is followed by the gas port bonding via the procedure described in previous sections. Traditional

conductive epoxies when used to make a contact with the platinum electrodes have shown to be especially destructive towards the graphene layer.

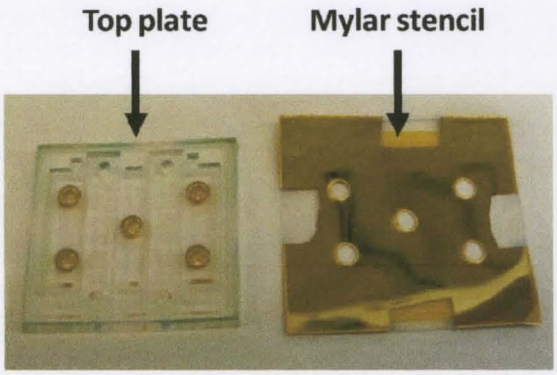

Figure 4.34. Top plate with patterned gold electrodes and corresponding mylar stencil

Severe breakage leads to poor contact within the circuit described earlier in this chapter. Alternately, patterning a protective layer of gold over the graphene following the bonding process (see Figure 4.35) using a second mylar stencil provides good contact with the graphene layer (and forms a protective base for pt wire/conductive epoxy when making a contact with graphene).

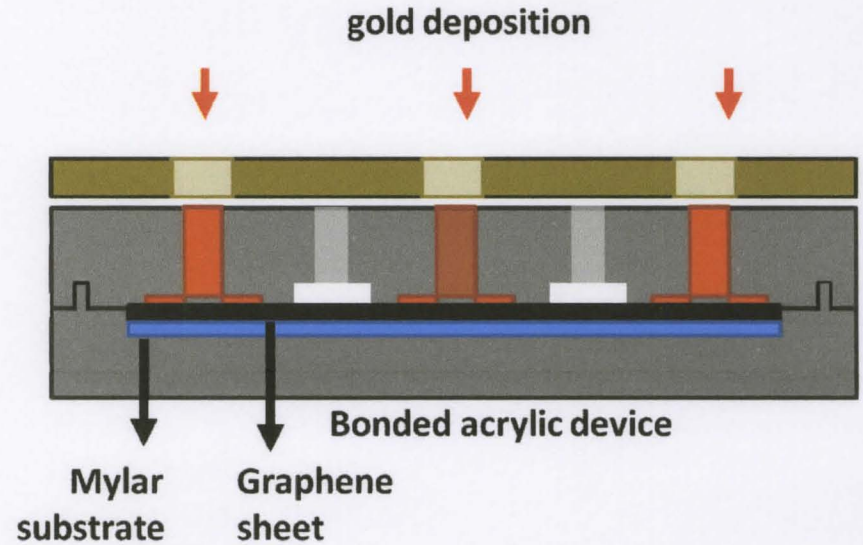

Figure 4.35. Patterning second layer of gold electrodes onto a bonded acrylic device using as mylar stencil mask

A schematic of an acrylic device following a second patterning of gold electrodes is shown in Figure 5.36. This second patterning step in spite of protecting the graphene layer from the conductive epoxy does not make proper contact.

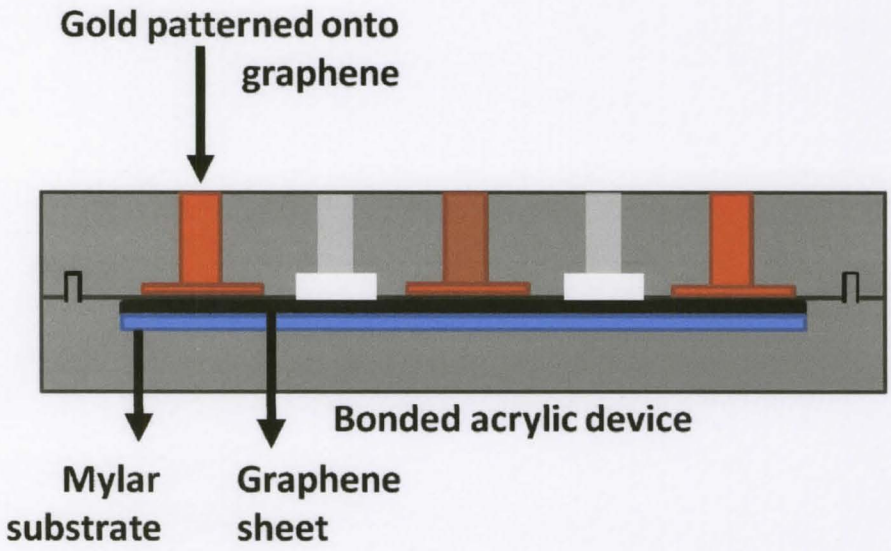

Figure 4.36. Schematic showing gold patterned directly onto underlying graphene layer

Differential voltage measurements carried out on these devices show a noisy output which can be attributed to poor contact of the gold electrodes with the underlying graphene sheet.

CHAPTER V

RESULTS AND DISCUSSIONS

5.1 Sensor response in single channel device

The operating principle behind a resistive chemical device sensor is the change in local carrier concentration due to gas molecules adsorbed on graphene's surface – that act as either donors or acceptors, resulting in a change in resistance (39). It has been reported that the adsorption of individual gas molecules onto a graphene surface leads to a discernible change in its electrical resistance. It has been seen in the current work being reported here, that on exposure to the organic solvent vapors, a large easily detectable change in graphene's resistance is recorded immediately.

The results shown in the succeeding pages discuss the sensor response when it is exposed to organic solvent vapors Ethanol, Methanol and IPA at 100% concentration levels. When these solvents are bubbled individually into the sensor through a neutral carrier gas (N_2), the sensing element graphene exhibits a marked change in its resistance. Each experiment is carried out in phases, where the sensor is exposed to alternate phases of purge (N_2) gas and analyte gas.

5.1.1 Sensor response to methanol vapors

Methanol, more commonly known as methyl alcohol is a volatile, colorless flammable liquid. It is characterized by its chemical formula CH_3OH (or MeOH). It is a highly toxic material, and has been known to cause blindness, permanent damage and even fatality when ingested (141). In order to be able to detect the presence of methanol, a sensor needs to exhibit marked sensitivity to its presence i.e., the sensor has to respond by exhibiting a change in its electrical properties when methanol molecules adsorb onto the surface of the sensing element. These initial tests on graphene as a viable MeOH sensor are carried out and the response is recorded. Figure 5.1 shows the graphene monolayers response to methanol vapors at 100% concentration. The data is plotted as a change in resistance $R_{graphene}$ against discrete intervals of time – each phase lasting 360 seconds.

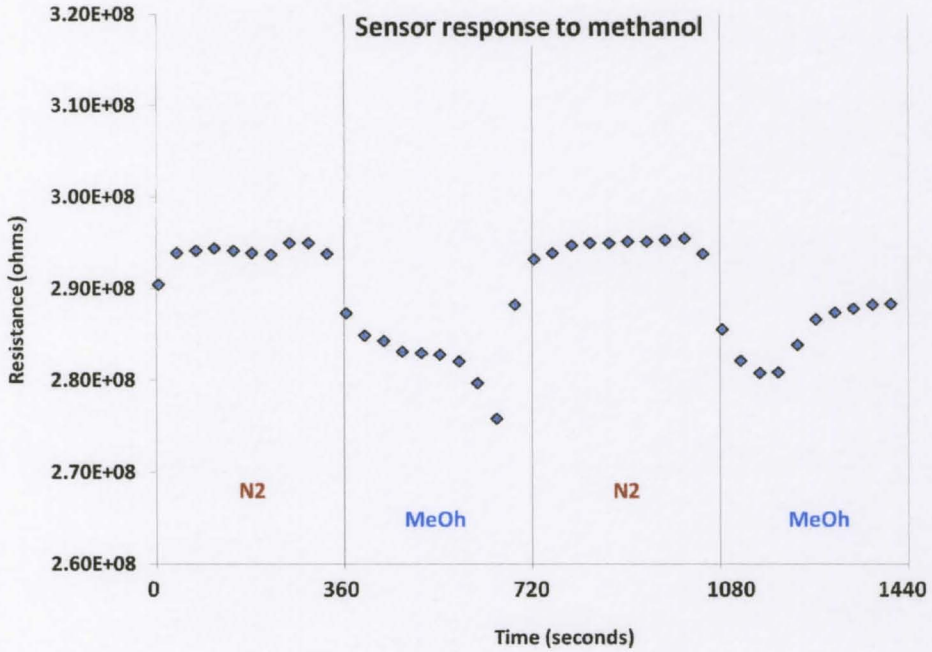

Figure 5.1: Graphene resistance change on exposure to methanol vapors

The first phase or cycle in the experiment exposes the graphene layer to 100% N_2 gas. At this stage, a baseline resistance is established – that of $R_{graphene(N2)}$. This cycle runs for 360 seconds at the end of which, the analyte (here-MeOH) cycle is introduced immediately

after isolating the N_2 line. At the onset of the analyte cycle, the graphene resistance is seen decreasing instantaneously. These cycles of alternating N_2 and methanol vapors are continued and the graphene responds by exhibiting a corresponding change in its resistance.

5.1.2 Sensor response to ethanol vapors

Ethanol, more commonly called ethyl alcohol- like methanol is a volatile, flammable colorless liquid. It is characterized by its chemical formula CH_3CH_2OH (or EtOH). It is a highly toxic material, with a flash point of 16.6 ^{o}C for pure ethanol (142) and has been known to target the central nervous system, liver and other vital organs.

This section describes the graphene based sensor's ability to detect the presence of ethanol in a nitrogen rich environment. In order to be able to detect ethanol, a sensor needs to exhibit marked sensitivity to its presence. To investigate this, N2 gas saturated with EtOH is introduced into the sensor environment and the response to the same is shown in Figure 5.2. Similar to the experiments carried out in the presence of MeOH vapors, the first phase or cycle in the experiment exposes the graphene layer to 100% N_2 gas for 360 seconds at the end of which, the analyte (here-EtOH) cycle is introduced immediately after isolating the N_2 line. Contrary to expectations – the graphene resistance increasing, at the onset of the analyte cycle, the graphene resistance is seen decreasing instantaneously (much like in the presence of methanol vapors). These cycles of alternating N_2 and ethanol vapors are continued and the graphene response is tabulated.

Previously, ΔR/R values of ~23% in a bilayer graphene sensor have been reported for a 0.5%concentration of ethanol (143).

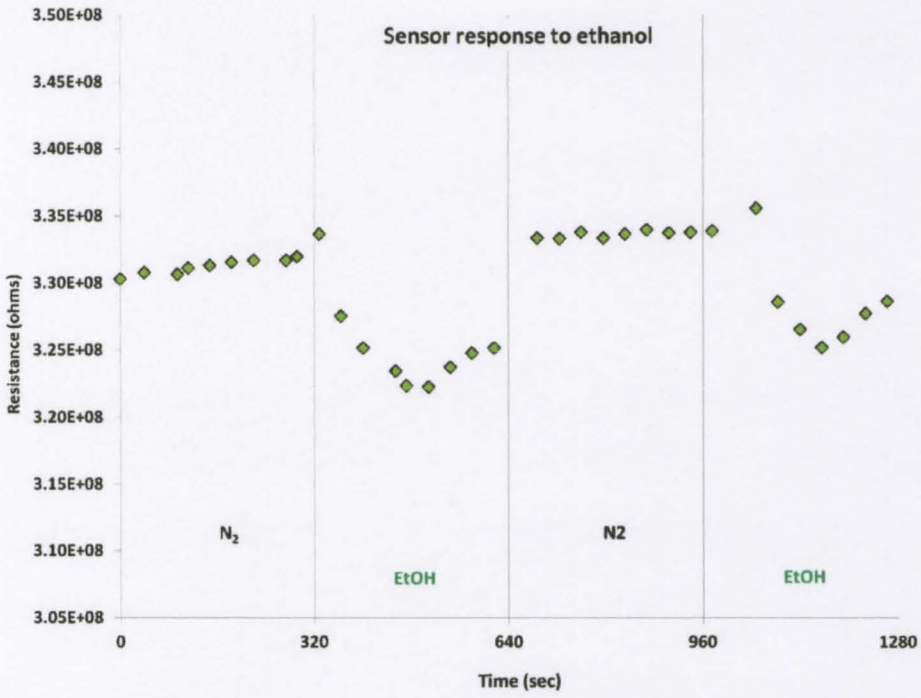

Figure 5.2: Graphene resistance change on exposure to ethanol

5.1.3 Sensor response to Isopropyl alchohol vapors

Isopropyl alcohol or 2-propanol is characterized by its chemical formula $(CH_3)_2CHOH$. Though it is preceeded in toxicity and hazard by methanol, IPA does act as a poison when either ingested, inhaled or absorbed into the skin. This section discusses the senor response on exposure to 100% IPA vapors, in cycles of N_2 to flush out these vapors. Figure 5.3 shows the change in graphene resistance where surface adsorbates from the IPA vapors influence the electric properties of graphene, showing a marked decrease in its resistance.

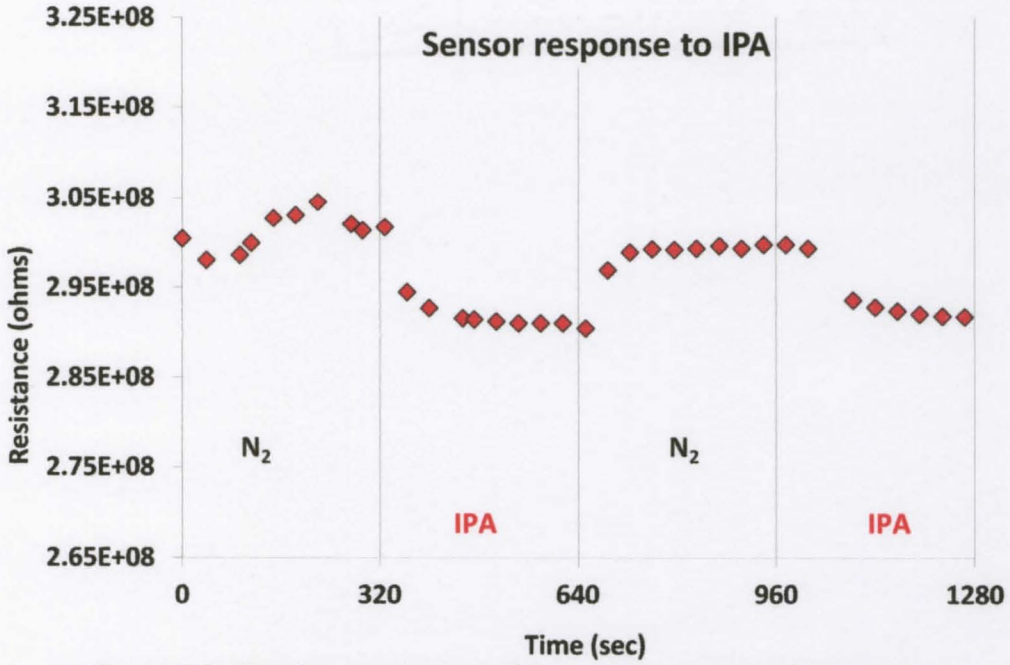

Figure 5.3: Graphene resistance change on exposure to isopropyl alcohol vapors

It is interesting to note that the resistance in all the vapor exposure cycles decreases for the graphene layer. This change can be plotted as a function of sensitivity of the sensor and is shown in Figure 5.4. The analysis of the sensor response on being exposed to analyte gases shows that the response is rapid (tens of seconds) and the signal recovery is reversible when the sensor is flushed with pure N_2 between analyte gas phases, suggesting no covalent bonding is occurring with the graphene surface, with an estimated signal recovery time constant of 400 seconds. This signal recovery after each cycle is also spontaneous and is independent of any heating, annealing or exposure to UV radiation – as is seen is several of the sensors being reported in literature currently . Repetitive analyte-gas/N_2 exposure cycles show consistent performance by the sensor without any signal degradation. The reproducibility of these sensors was investigated over a period of

16 weeks. The results indicate stable electrical characteristics which is a desired trait in sensors applications.

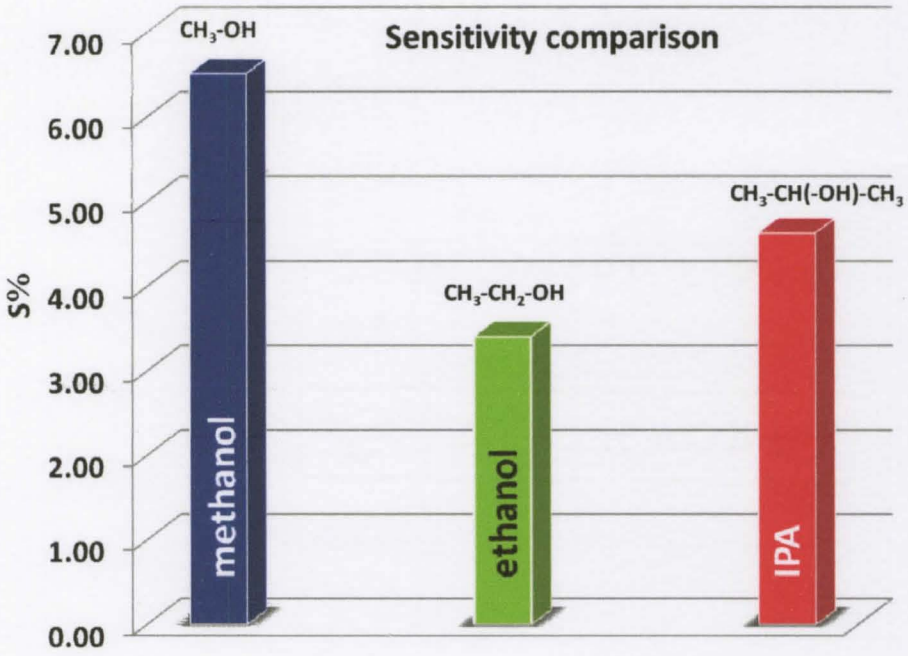

Figure 5.4: Bar chart comparing sensitivity of single channel sensor device to organic solvent vapors

The sensitivity comparison in Figure 5.4 shows that Methanol induces the highest change in resistance ($\Delta R/R_0$) of graphene at ~6.5%, followed by isopropyl alcohol at 4.6% and ethanol at 3.4%. The sensitivity of the sensor is with upper limit concentrations of the vapors are therefore estimated at 4-5%.

Graphene is essentially a p-type material in ambient air. And being a 2-dimensional material, it is extremely sensitive to the environment it is exposed to, as well as the substrate it is transferred onto. Though several reports have shown the effect of substrate (144) (145) and the role of PMMA in introducing n-type dopants in graphene (146) the exact role that each plays is yet to be fully understood. The sensor response

showing a decreased resistance in the presence of the organic vapor solvents that serve as electron donors shows that the graphene layer is exhibiting n-type behavior. This could be due to either the effect of PDMS substrate or the influence of PMMA used during the transfer process. For a better understanding of the mechanism at work here, further investigation in this direction is carried out by modifying the sensor design and incorporating dual channels and differential voltage measurements to filter out noise. The experimental results from the dual channel sensor device are described in the succeeding section.

5.2: Sensor response in dual channel device

The experimental data from single channel sensor devices confirms the graphene monolayer responding to the presence of organic solvent vapors, with varying sensitivity. This quality is further analyzed in the dual channel device with the same solvent vapors, (methanol, ethanol and IPA) but at varying concentrations. Dilutions from a 100% organic solvents are prepared with de-ionized (DI) water to decrease their weight/weight concentrations, thus preparing 50%, 25%, 10%, 8%, 5% and 2% dilutions. The results are then plotted as a function of % sensitivity (S) of the device given by $\Delta R/R$, where ΔR is the difference in the resistance of graphene in the presence of N_2 and in the presence of the analyte vapor.

5.2.1 Sensor response to methanol vapors

The dual channel sensor device's response shows the cycle dependent responses of the graphene monolayer resistance when the devices were tested in the pure nitrogen environment and in varying methanol concentrations with nitrogen backfill (see Figure 5.5)

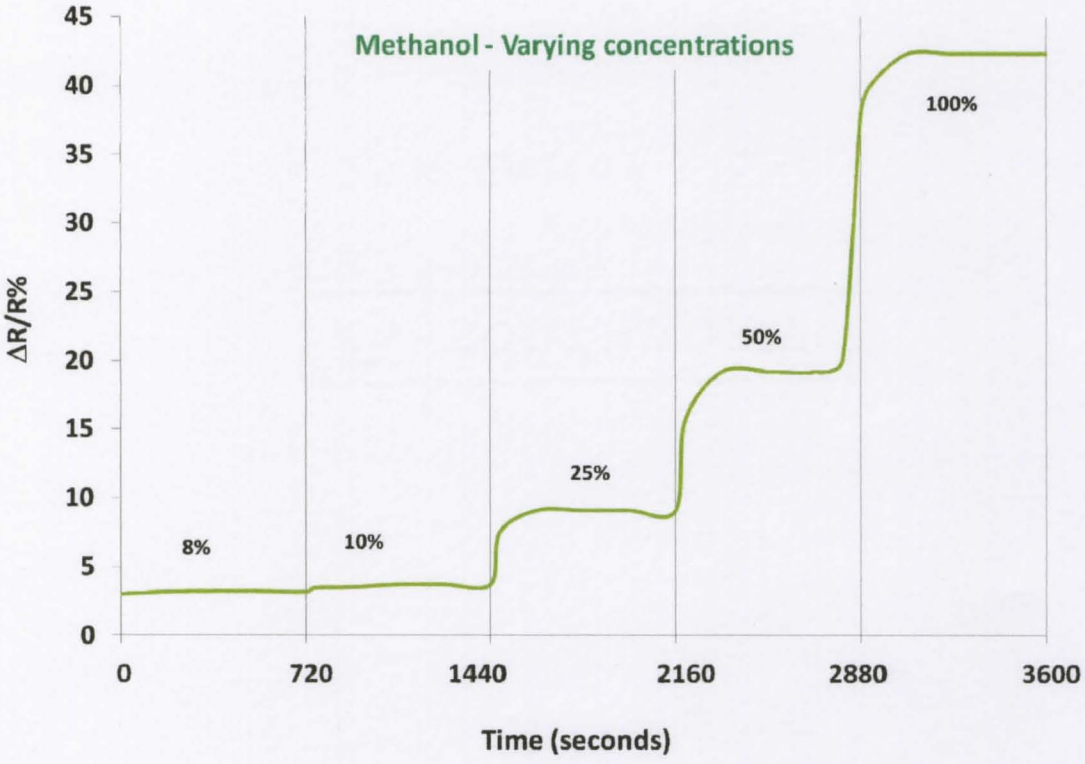

Figure 5.5. Dual channel device – graphene response to varying concentrations of methanol

All the experiments are carried out at a low voltage of 400mV applied to the electrodes of the sensors. This low voltage prevents graphene from undergoing electrical breakdown. As has been explained in the previous chapter (IV), the graphene response is allowed to stabilize before each data point is recorded by the data acquisition system, minimizing

stray readings and providing a window for the adsorbed gas molecules to redistribute over the graphene surface (during and in-between gas cycle switching). It has been observed that in contrast to the single channel graphene sensors that show a marked decrease in resistance on exposure to analyte vapors, the dual channel devices show an increase in resistance (as was originally expected regarding the device behavior). This is interesting especially since, the substrate that supports the monolayer graphene in the dual channel device is mylar (as opposed to PDMS in the single channel device). It is therefore very promising to see if the devices behave in this expected manner in the presence of other analyte vapors (reported in the next sections of the chapter).

The data plotted in Figure 5.5 shows the sensor response shows a remarkably significant increase in sensitivity when the graphene layer is exposed to 100% methanol vapors. As the concentration of the solvent vapors is decreased, it is seen that the sensor response drops. This might be indicative of the sensor's lower detection limit. These experiments are all carried out with alternating N_2 and analyte vapor cycles, and the data obtained is plotted as shown in Figure 5.5, to provide a comprehensive view of the sensor's response.

5.2.2 Sensor response to ethanol vapors

On establishing graphene's response to methanol vapors, experiments on dual channel devices are repeated to investigate its ability to sense ethanol vapors of varying concentrations. The data obtained from these experiments are shown graphically in Figure 5.6

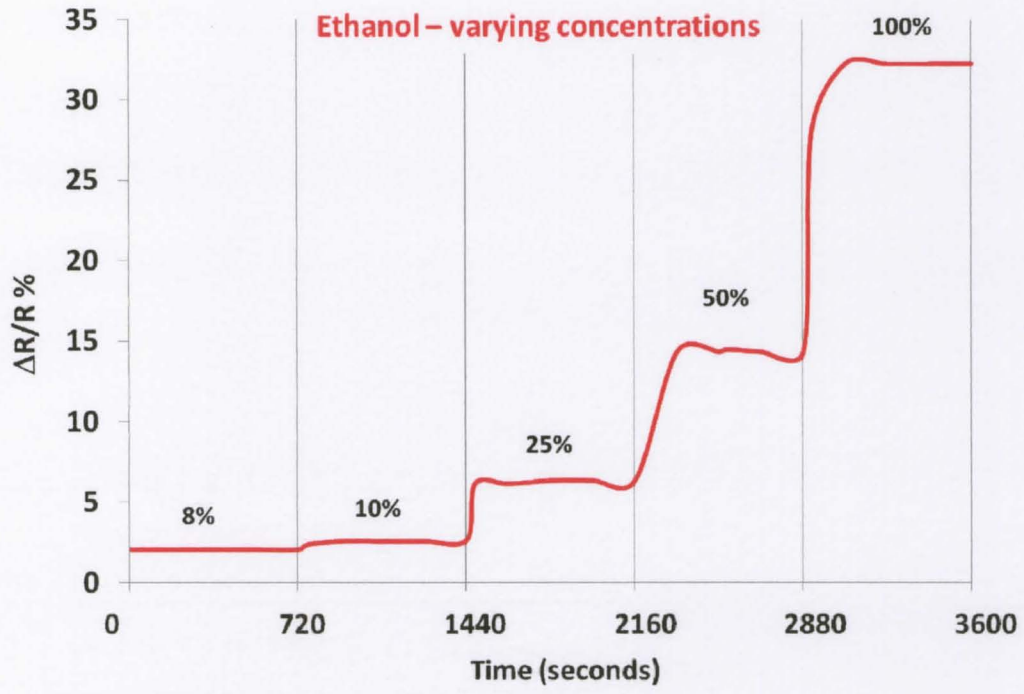

Figure 5.6 Dual channel device – graphene response to varying concentrations of ethanol

Similar to the device response when exposed to methanol, the ethanol vapors induce a remarkable increase in graphene resistance (from its base line resistance in the N_2 cycle), again in marked contrast to the same vapors inducing a decrease in resistance in the single channel device. Concentrations of vapors below 7% however, failed to elicit any discernible change in resistance, marking the lower detection limit of the device.

5.2.3 Sensor response to IPA vapors

Following the trend established by the single channel device, graphene shows a preferentially higher response (change in resistance) to methanol, followed closely by IPA, with ethanol eliciting least (comparatively) response. Figure 5.7 shows the dual

channel device sensing varying concentrations of IPA, at a constant applied voltage of 400mV and stable room temperature conditions.

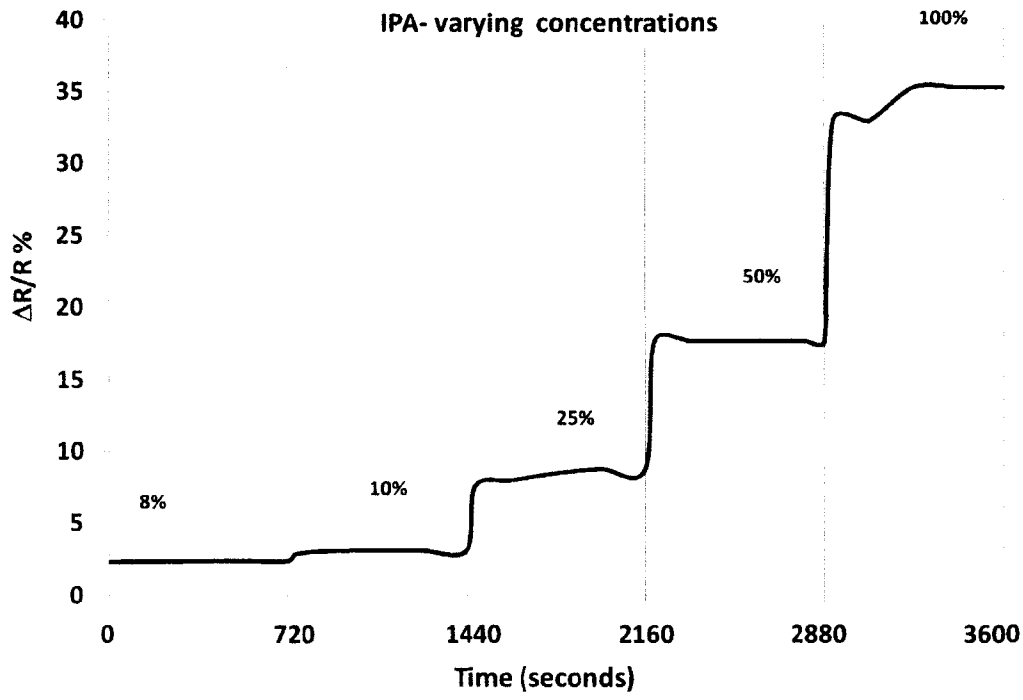

Figure 5.7: Dual channel device – graphene response to varying concentrations of ethanol

The response of the sensor drops and no significant change is observed when the vapor concentration is reduced to below 8%. However, at upper limit concentrations, the single and dual channel devices show marked difference in their responses, as can be seen in Figure 5.8.

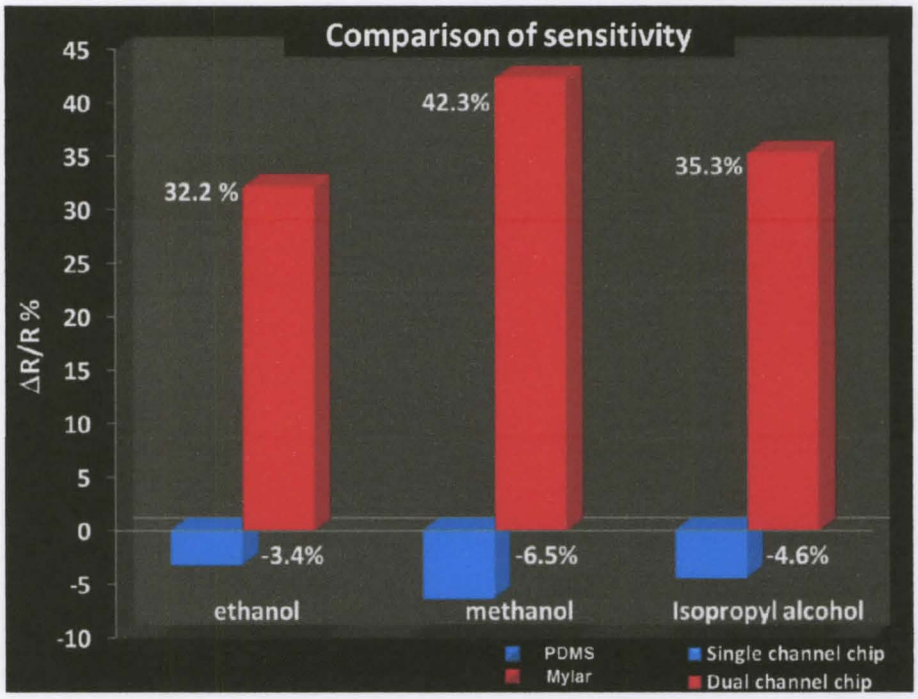

Figure 5.8: Plot comparing sensor response

Figure 5.8 shows a compiled plot with the dual channel device response at upper limit concentrations.

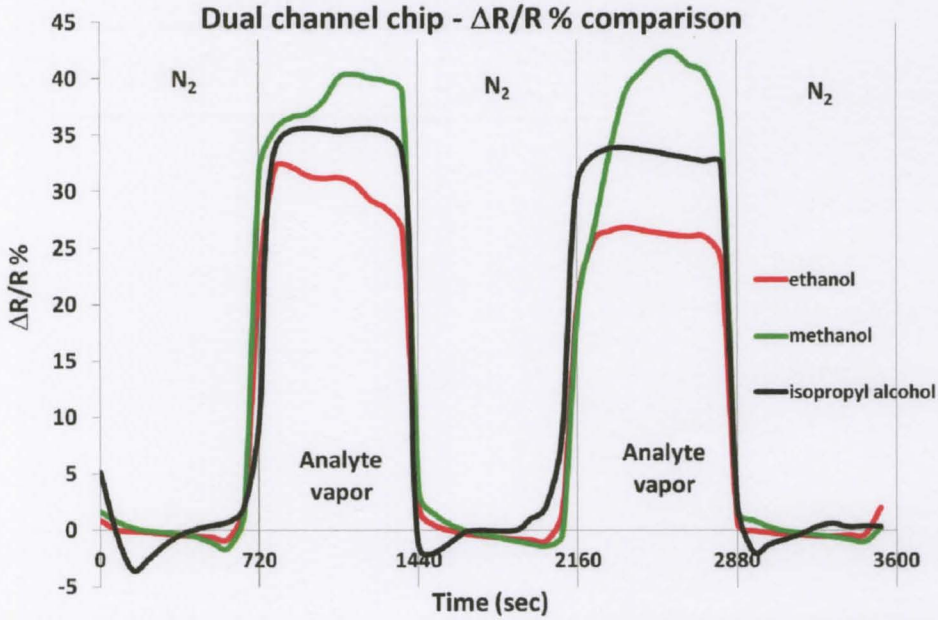

Figure 5.9: Plot comparing sensor response – upper limit concentrations

From the data shown in Figure 5.9, the positive change in resistance of the graphene in the presence of analyte vapors can only be attributed to the substrate playing a role. This behavior of the graphene layer is also in conjunction with existing literature that shows graphene acts as a p-type material in ambient air. This has been challenged by the single channel device, where the substrate supporting the grapahene-PDMS could be unintentionally doping the graphene, leading to its behaving as an n-type material. Though edge-defects and graphene chirality have been known to play a role in influencing the innate transport properties of monolayer graphene, it has not yet be shown that they lead to an inversion of resistance –behavior. The resistance decrease in the single channel sensor is however consistent with existing reports (39) (143), where organic solvent vapor molecules serve as electron-donors to the n-type graphene sheet in this case.

It is to be noted however, that in both the devices, the signal recovery is rapid when the sensor is flushed with pure N_2 between analyte gas phases, suggesting no covalent bonding of the gas molecules is occurring with the graphene surface. The recovery is spontaneous, without subjecting the sensor to heating, annealing or exposure to UV-light. Repetitive analyte-gas/N_2 exposure cycles show consistent performance by the sensor without any signal degradation. The reproducibility of these sensors was investigated over a period of 16 weeks (for single channel) and over a period of 21 weeks (for dual channel device). The results indicate stable electrical characteristics which is a desired trait in sensors applications.

CHAPTER VI

CONCLUSIONS AND FUTURE WORK

The work discussed in this dissertation has shown that carbon based nanomaterials are excellent as sensing elements. As the building block of carbon materials of all dimensions, graphene exhibits specific electronic structure, properties and physiochemistry. It shows amazing performance as a resistive chemical sensing element (here, for the detection of organic vapor solvents). As a competitor to carbon nanotubes, graphene has exhibited superior performance in these applications. However, the development of graphene-based materials/devices at a low cost to the manufacturer is still in its infancy. The current manufacturing techniques are limited in their flexibility and cost effectiveness of the materials being used. This work has addressed the pressing need to provide an inexpensive way to manufacture/package graphene based sensor devices. With acrylic as the packaging material, and CVD grown monolayer graphene as the sensing element, each individual laser cut sensor packaging chip can be manufactured at less than $2. This is much lower than the present expenses being incurred by manufacturers in packaging a graphene based sensor device. However, to further bring down the cost, bulk production methods for pristine monolayer graphene have to be developed so as to reduce the overhead costs in manufacturing.

With the sole aim of keeping the manufacturing costs low, the design for these sensors incorporated KCl solution (essentially salt water) as contacts between the

platinum wire probes and the graphene layer. The AC signal was capacitively coupled through the double layer at the electrode interface, through the resistive solution, to the double layer at the graphene-salt interface. (Could use a schematic of this showing it as a circuit diagram, and should discuss this point earlier in the text) However, to carry out comparative studies on the sensor performance with electro-deposited gold electrodes, dual channel sensor devices were prepared. The design involved coating the electrode ports with a thin film of gold on the top plate and then bonding the chips together (as described in chapter IV). A second improvement on this design involved a second layer of patterning gold into the electrode ports after chip bonding process. However, owing to poor contact between the patterned electrodes and the graphene layer, the performance of the devices was poor. This concept however, can be slightly modified to incorporate a gold coated electrode that when bonded, is pushed into contact with the enclosed graphene layer (much like a weighted plunger), to ensure good contact. Slight modifications to the electrode design can therefore lead to lower power consumption. A portable sensor can be designed by modifying the setup and incorporating a DC power source (Alkaline 9V batteries).

Further, owing to the un-functionalized surface of the monolayer graphene, the lowest detection limit of these devices is seen to be around 7-8% of vapor concentration. It is possible to lower the detection limit by enhancing the surface properties of graphene – by either depositing functionalized gold nanoparticles or by intentionally doping the pristine graphene with heteroatoms (nitrogen, boron etc.,) to probe the shift in sensing mechanism. As the studies done on carbon nanotubes have yielded immense data on the

improvement of electrocatalytic activity of the carbon atoms, similar studies on graphene should be pursued.

REFERENCES

1. *Chemical Sensors Definitions and Classifications.* **A.Hulanicki, S. Glab and F. Ingman.** 9, 1991, Pure & Appl. Chem., Vol. 63, pp. 1247-1250.

2. **Pennsylvania Department of Environmental Protection.** [Online] 1969. http://www.dep.state.pa.us/earthdaycentral/97/air_teachers/TAB1.htm.

3. *Industrial Sensor Technologies and Market.* s.l. : BCC Inc. Report, GB-200R, 2002.

4. *Gas Sensors Status and Future Trends for Safety Applications.* **T.Shigemori.** 2012. The 14th International Meeting on Chemical Sensors. p. 49.

5. **G.Sberveglieri.** *Gas Sensors: principles, operation, and development.* s.l. : Springer, 1992.

6. **J.Chou.** *Hazardous gas monitors: a practical guide to selection, operation and applications.* s.l. : McGraw-Hill Professional, 2000.

7. *Solid State Gas Sensors: State of The Art and Future Activities.* **S.Capone, A.Forleo, L.Francisco, R.Rella, P.Siciliano, J.Spadavecchia, D.S.Presicce, A.M.Taurino.** 5, 2003, Journal of Optoelectronics and Advanced Materials, Vol. 5, pp. 1335-1348.

8. *An Account of an Invention for Giving Light in Explosive Mixtures of Fire-Damp in Coal Mines, by Consuming Fire-Damp.* **Davy, Humphry.** 1816, Phil.Trans.R.Soc.Lond., Vol. 106, pp. 23-24.

9. **RKI Instruments.** RKI/Riken Keiki History. [Online] http://www.rkiinstruments.com/pages/history.htm.

10. **B.M.Oliver, J.M.Cage.** Electronic Measurements and Instrumentation. s.l. : McGraw-Hill, 1971, 9, p. New York.

11. *Highly accurate resistance deviation to frequency converter with programmable sensitivity and resolution.* **C.D.Johnson, H.Al Richeh.** 1986, IEEE. Trans. Instrum. Meas.,, Vols. IM-35, pp. 178-181.

12. Arthurs Science and Technology. [Online] http://arthursclipart.org/sciencetechnology/page_01.htm.

13. *A new detector for gaseous components using semiconductive thin films.* **T.Seiyama, A.Kato, K.Fujiishi, M.Nagatani.** 11, 1962, Anal.Chem., Vol. 34, pp. 1502-1503.

14. *Investigation of structure and properties of N-doped TiO2 thin films grown by APCVD.* **Y.Guo, X.W.Zhang, G.R.Han.** 2, 2006, Mater.Sci.Eng, Vol. 135, pp. 83-87.

15. *Development of ultra-low-power consumption MOX sensors with ppb-level VOC detection capabilities for emerging applications.* **I.Elmi, S.Zampolli, E.Cozzani, F.Mancarella, G.C.Cardinali.** 1, 2008, Sens.Actuat.B-Chem, Vol. 135, pp. 342-351.

16. **P.Grundler.** *Chemical Sensors: An Introduction for Scientists and Engineers.* Berlin : Springer, 2007.

17. *Array based vapor sensing using chemically sensitive, carbon black-polymer resistors.* **M.C.Lonergan, E.J.Severin, B.J.Doleman, S.A.Beaber, R.H.Grubbs, N.S.Lewis.** 9, 1996, Chem. Mater, Vol. 8, pp. 2298-2312.

18. *Monitoring space shuttle air quality using the Jet Propulsion Laboratory electronic nose.* **M.A.Ryan, H.Zhou, M.G.Buehler, K.S.Manatt, V.S.Mowrey, S.P.Jackson, A.K.Kisor, A.V.Shevade, M.L.Homer.** 3, 2004, IEEE Sens.J, Vol. 4, pp. 337-347.

19. *B.C.Munoz, G.Steinthal, S.Sunshine.* **nose, Conductive polymer-carbon black composites-based sensor arrays for use in an electronic.** 4, 1999, Sensor Review, Vol. 19, pp. 300-305.

20. *Single- and multi-wall carbon nanotube field-effect transistors.* **R.Martel, T.Schmidt, H.R.Shea, T.Hertel, Ph.Avouris.** 17, 1998, Appl.Phys.Lett, Vol. 73, pp. 2447-2449.

21. *Electric field effect in atomically thin carbon films.* **K.S. Novoselov, A.K. Geim, S.V. Morozov, D.Jiang, Y. Zhang, S.V. Dubonos, I.V. Gregorieva and A.A. Firsov.** 5696, 2004 йил, Science, Vol. 306, p. 666.

22. *Chemical system miniaturization.* **R.W.Wegeng, C.J.Call, M.K.Drost.** 1996. Proceedings of Sping National Meeting AIChE. p. 1.

23. **S.Kona.** *Synthesis of carbon nanotube arrays and diverging conical structures in a capillary microreactor.* Electrical and Computer Engineering, University of Louisville. 2008.

24. *Low-temperature growth of carbon nanotubes by plasma-enhanced chemical vapor deposition.* **S.Hofmann, C.Ducati, J.Robertson, B.Kleinsorge.** 2003, Appl.Phys.Lett, Vol. 83, p. 135.

25. *Microplasmas and applications.* **K.H.Becker, K.H.Schoenbach, J.G.Eden.** 2006, J.Phys.D:Appl.Phys, Vol. 39, pp. R55,.

26. *Carbon nanotube growth studies using an atmospheric, microplasma reactor.* **S.Kona, J.H.Kim, C.K.Harnett, M.K.Sunkara.** 2009, IEEE Trans. Nanotechnol., Vol. 8, p. 286.

27. *Microplasma synthesis of metal nanoparticles for gas-phase studies of catalyzed carbon nanotube growth.* **W.-H.Chiang, R.M.Sankaran.** 2007, Appl.Phys.Lett., Vol. 91, p. 121503.

28. *Two dimensional gas of massless Dirac fermions in graphene.* **K.S.Novoselov, A.K.Geim, S.V.Morozov, D.Jiang, M.Katsnelson, I.V.Grigorieva, S.V.Dubonos and A.A.Firsov.** 2005, Nature, Vol. 438, p. 197.

29. *The electronic properties of graphene.* **A.H.C.Neto, F.Guinea, N.M.R.Peres, K.S.Novoselov and A.K.Geim.** 2009, Rev.Mod.Phys, Vol. 81, p. 109.

30. *Intrinsic and extrinsic performance limits of graphene devices on SiO2.* **J.-H.Chen, C.Jang, S.Xiao, M.Ishigami and M.S.Fuhrer.** 2008, Nat.Nanotechnol., Vol. 3, p. 206.

31. *Fine Structure Constant Defines Visual Transparency of Graphene.* **R. R. Nair, P. Blake, A. N. Grigorenko, K. Novoselov, T. J. Booth,T. Stauber, N. M. R. Peres and A. K. Geim.** 2008, Science, Vol. 320, p. 1308.

32. *Universal Optical Conductance of Graphite.* **A.B.Kuzmenko, E.V.Heumen, F.Carbone and D.V.D Marel.** 2008, Phys.Rev.Lett, Vol. 100, p. 117401.

33. *Fractional quantum Hall effect and insulating phase of Dirac electrons in graphene.* **X. Du, I. Skachko, F. Duerr, A. Luican and E. Y. Andrei.** 2009, Nature, Vol. 462, p. 192.

34. *Experimental observation of the quantum hall effect and berry's phase in graphene.* **Y.Zhang, Y.-W.Tan, H.L.Stormer, P.Kim.** 2005, Nature, Vol. 438, p. 201.

35. *Approaching ballistic transport in suspended graphene.* **X. Du, I. Skachko, A. Barker and E. Y. Andrei.** 2008, Nat.Nanotechnol., Vol. 3, p. 491.

36. *Measurement of the Elastic Properties and Intrinsic Strength of Monolayer Graphene.* **C. Lee, X. Wei, J. W. Kysar and J. Hone.** 2008, Science, Vol. 321, p. 385.

37. *Superior Thermal Conductivity of Single-Layer Graphene.* **A.A.Baladin, S.Ghosh, W.Bao, I.Calizo, D.TeweldebrhanF.Ming, C.N.Lau.** 2008, Nano Lett, Vol. 8, p. 902.

38. *A tight-binding approach to uniaxial strain in graphene.* **V.M.Periera, A.H.Castro Netro, N.M.R.Peres.** 2009, Phys.Rev.B, Vol. 80, p. 045401.

39. *Detection of individual gas molecules adsorbed in graphene.* **F.Schedin, A.K. Geim, S.V.Morozov, E.W.Hill, P.Blake, M.I Katsnelson and K.S.Novoselov.** 2007, Nat.Mater, Vol. 6, p. 652.

40. *The growth and morphology of epitaxial multilayer graphene.* **J.Hass, W.A.de Heer and E.H.Conrad.** 2008 йил, J.Phys.:Condens.Matter, Vol. 20, p. 323202.

41. *Lattice Constants of Graphite at Low Temperatures.* **Y.Baskin, L.Mayer.** 1955, Phys.Rev, Vol. 100, p. 544.

42. *Structural properties of the multilayer graphene/ 4H-SiC(0001̄) system as determined by surface x-ray diffraction.* **J, Hass, R.Feng, J.E.M.-Otoya, X.Li, M.Sprinkle, P.N.First, C.Berger, W.A.de Heer and E.H. Conrad.** 2007, Phys.Rev.B, Vol. 75, p. 214109.

43. *Fabrication and electric-field-dependent transport measurements of mesoscopic graphite devices.* **Y.Zhang, J.P.Small, W.V.Pontius and P.Kim.** 2005, Appl.Phys.Lett, Vol. 86, p. 073104.

44. *Band Structure of Rhombohedral Graphite.* **Haering, R.R.** 1958, Can.J.Phys, Vol. 36, p. 352.

45. *Energetics of interplanar binding in graphite.* **M.C.Schabel, J.L.Martins.** 1992, Phys.Rev.B, Vol. 46, p. 7185.

46. *The Band Theory of Graphite.* **P.R.Wallace.** 1947, Phys.Rev., Vol. 71, p. 622.

47. *Graphene: carbon in two dimensions.* **Katsnelson, M.I.** 2007, Mat.Today, Vol. 10, p. 20.

48. *Ultrathin Epitaxial Graphite: 2D Electron Gas Properties and a Route toward Graphene-based nanoelectronics.* **C.Berger, Z.Song, T.Li, X.Li, A.Y.Ogbazghi, R.Feng, Z.Dai, A. N. Marchenkov, E.H.Conrad, P.N.First and.** 2004 йил, J.Phys.Chem.B, Vol. 108, p. 19912.

49. *Graphene: Status and Prospects.* **A.K.Geim.** 2009, Vol. 324, p. 1530.

50. *Preparation and characterization of graphene oxide paper.* **D.A.Dikin, S.Stankovich, E.J.Zimney, R.D.Piner, G.H.B.Dommett,G.Evmenenko, S.T.Nguyen, R.S.Ruoff.** 2007, Nature, Vol. 448, p. 457.

51. *Wafer-scale reduced graphene oxide films for nanomechanical devices.* **J.T.Robinson, M.Zalalutdinov, J.W.Baldwin, E.S.Snow, Z.Wei, P.Sheehan, B.H.Houston.** 2008, Nano Lett., Vol. 8, p. 3441.

52. *Electromechanical resonators from graphene sheets.* **J.S.Bunch, A.M.van der Zande, I.W.Frank, D.M.Tanenbaum, J.M.Parpia, H.G.Craighead, P.L.McEuen.** 2007, Science, Vol. 315, p. 490.

53. *Energy gaps in graphene nanoribbons.* **Y.W.Son, M.L.Cohen, S.G.Louie.** 2006, PRL, Vol. 97, p. 216803.

54. *Performance projections for ballistic graphene nanoribbon field-effect transistors.* **G.C.Liang, N.Neophytou, D.E.Nikonov, M.S.Lundstrom.** 2007, IEEE Trans.Electron.Dev, Vol. 54, p. 677.

55. *Chemically Derived, Ultrasmooth Graphene Nanoribbon Semiconductors.* **X.Li-, X.Wang, L.Zhang, S.Lee, H.Dai.** 2008, Science, Vol. 319, p. 1229.

56. *Chaotic Dirac billiard in graphene quantum dots.* **L.A.Ponomarenko, F.Schedin, M.I.Katsnelson, R.Yang, E.W.Hill, K.S.Novoselov, A.K.Geim.** 2008, Science, Vol. 320, p. 356.

57. *Operation of Graphene Transistors at Gigahertz Frequencies.* **Y.-M.Lin, K.A.Jenkins, A.V.Garcia, J.P.Small, D.B.Farmer, P.Avouris.** NewYork : s.n., 2009, Nano Lett, Vol. 9, p. 422.

58. *Macroscopic Graphene Membranes and Their Extraordinary Stiffness.* **T.J.Booth, P.Blake, R.R.Nair, D.Jiang, E.W.Hill, U.Bangert,A.Bleloch, M.Gass, K.S.Novoselov, M.I.Katsnelson, A.K.Geim.** 2008, Nano Lett, Vol. 8, p. 2442.

59. *Large-scale pattern growth of graphene films for stretchable transparent electrodes.* **K.S.Kim, Y.Zhao, H.Jang, S.Y.Lee, J.M.Kim, K.S.Kim, J.H.Ahn, P.Kim, J.-Y.Choi, B.H.Hong.** 2009, Nature, Vol. 457, p. 706.

60. *Organic solar cells with solution-processed graphene transparent electrodes.* **J.Wu, H.A.Becerril, Z.Bao, Z.Liu, Y.Chen, P.Peumans.** 2008, Appl.Phys.Lett, Vol. 92, p. 263302.

61. *Transparent, conductive graphene electrodes for Dye-sensitized solar cells.* **X.Wang, L.Zhi, K.Müllen.** 2008, Nano Lett., Vol. 8, p. 323.

62. *Transport in chemically modified graphene in the presence of adsorbed moelcules.* **E.H.Hwang, S.Adam, S. Das Sarma.** 2007, Phys.Rev.B, Vol. 76, p. 195421.

63. *Scattering mechanisms and Boltzmann transport in graphene.* **S.Adam, E.H.Hwang, S. Das Sarma.** 2008, Physica E, Vol. 40, p. 1022.

64. *Measurement of scattering rate and minimum conductivity of graphene.* **Y.W.Tan, Y.Zhang, K.Bolotin, Y.Zhao, S.Adam, E.H.Hwang, S.Das Sarma, H.L. Stormer, P.Kim.** 2007, Phys.Rev.Lett, Vol. 99, p. 246803.

65. *Adsorption of formaldehyde molecule on the intrinsic and Al-doped graphene: a first principle study.* **M.Chi, Y.P.Zhao.** 2009, Comput.Mater.Sci, Vol. 46, p. 1085.

66. *Paramagnetic adsorbates on graphene: a charge transfer analysis.* **O.Leenaerts, B.Partoens, F.M.Peeters.** 2008, Appl.Phys.Lett, Vol. 92, p. 243125.

67. *Improving gas sensing properties of graphene by introduicing dopants and defects: a first-principles study.* **Y.H.Zhang, Y.B.Chen, K.G. Chou, C.H.Liu, J.Zeng, H.L.Zhang, Y.Peng.** 2009, Nanotechnology, Vol. 20, p. 185504.

68. *Molecular doping of graphene.* **T.O.Wehling, K.S.Novoselov, S.V.Morozov, E.E.Vdovin, M.I.Katsnelson, A.K.Geim, A.I.Lichtenstein.** 2008, Nano Lett., Vol. 8, p. 173.

69. *Adsorbates on graphene: impurity states and electron scattering.* **T.O.Wehling, M.I.Katsnelson, A.I.Lichtenstein.** 2009, Chem.Phys.Lett, Vol. 476, p. 125.

70. *Binding mechanisms of molecular oxygen and moisture to graphene.* **Y.Yang, R.Murali.** 2011, Appl.Phys.Lett, Vol. 98, p. 093116.

71. *Adsorption of ammonia on graphene.* **H.E.Romero, P.Joshi, A.K.Gupta, H.R.Gutierrez, M.W.Cole, S.A.Tadigadapa, P.C.Eklund.** 2009, Nanotechnology, Vol. 20, p. 245501.

72. *Adsorption of gas molecules on graphene nanoribbons and its implications for nanoscale molecule sensor.* **B.Huang, Z.Y.Li, Z.R.Liu, G.Zhou, S.G.Hao, J.Wu, B.L.Gu, W.H.Duan.** 2008, J.Phys.Chem, Vol. 112, p. 13442.

73. *Electrical transport and low-temperature scanning tunneling microscopy of microsoldered graphene.* **V. Geringer, D. Subramaniam, A. K. Michel, B. Szafranek, D. Schall, A. Georgi, T. Mashoff, D. Neumaier, M. Liebmann, and M. Morgenstern.** 2010, Appl.Phys.Lett., Vol. 96, p. 082114.

74. *Intrinsic response of graphene vapor sensors.* **Y.P.Dan, Y.Lu, N.J.Kybert, Z.T.Luo, A.T.C.Johnson.** 2009, Nano.Lett., Vol. 9, p. 1472.

75. *A LEED study of the deposition of carbon on platinum crystal surfaces.* **B.Lang.** 1, 1975 йил, Surface Science, Vol. 53, p. 317.

76. *Two dimensional atomic crystals.* **K.S. Novoselov, D. Jiang, F. Schedin, T.J. Booth, V.V. Khotkevich, S.V. Morozov and A.K. Geim.** 30, 2005 йил, PNAS, Vol. 102, p. 10451.

77. *Patterning of highly oriented pyrolytic graphite by oxygen plasma etching.* **X.Lu, H.Huang, N.Nemchuk and R.Ruoff.** 2, 1999 йил, Applied Physics Letters, Vol. 75, p. 193.

78. *A Chemical Route to Carbon Nanoscrolls.* **L.M.Viculis, J.J.Mack, R.B.Kaner.** 2003 йил, Science, Vol. 299, p. 1361.

79. *Fabrication and electric-field-dependent transport measurements of mesoscopic graphite devices.* **Y.Zhang, J.P.Small, W.V.Pontius and P.Kim.** 2005 йил, Applied Physics Letters, Vol. 86, p. 073104.

80. *Beyond sticky tape.* **R.V.Noorden.** 2012 йил, Nature, Vol. 483, p. S32.

81. *Graphene made easy:high quality large area samples.* **A.Shukla, R.Kumar, J.Mazher and A.Balan.** 2009 йил, Solid State Communications, Vol. 149, p. 718.

82. *Graphene Calling all chemists.* **R.Ruoff.** 1, 2008 йил, Nature Nanotechnology, Vol. 3, p. 10.

83. *Preparation of graphitic oxide.* **W.Hummers, R.Offeman.** 1958 йил, J.Am.Chem.Soc, Vol. 80, p. 1339.

84. *Sur le poids atomique du graphite.* **B.C.Brodie.** 1860 йил, Ann. Chim. Phys, Vol. 59, p. 466.

85. *Verfahren zur darstellung der graphitsaure.* **L.Staudenmaier.** 1898 йил, Ber Dtsch Chem Ges, Vol. 31, p. 1481.

86. *Intercalation compounds of graphite.* **M.S.Dresselhaus, G.Dresselhaus.** 1981 йил, Adv. Phys., Vol. 30, p. 139.

87. *Functionalized single graphene sheets derived from splitting graphite oxide.* **H.C.Schniepp, J.-L.Li, M.J. McAllister,H.Sai, M.Herrera-Alonso, D.H. Adamson, R.K.Prud'homme, R.Car, D.A. Saville and I.A. Aksay.** 2006 йил, J.Phys.Chem.B, Vol. 110, p. 8535.

88. *Single sheet functionalized graphene by oxidation and thermal expansion of graphite.* **M.J.McAllister, J.-L.Li, D.H.Adamson,H.C.Schniepp,A.A.Abdala, J.Liu, M. Herrera-Alonso,D.L.Milius, R.Car, R.K.Prud'homme and I.A.Aksay.** 2007 йил, Chem.Mater, Vol. 19, p. 4396.

89. **AsburyCarbons.**

90. *Synthesis of graphene-based nanosheets via chemical reduction of exfoliated graphite oxide.* **S.Stankovich, D.A.Dikin, R.D.Piner, K.A.Kohlhaas, A.Kleinhammes, Y.Jia,Y.Wu, S.T.Nguyen and R.S.Ruoff.** 2007 йил, Carbon, Vol. 45, p. 1558.

91. *High-yield production of graphene by liquid-phase exfoliation of graphite.* **Y.Hernandez, V.Nicolosi, M.Lotya, F.M.Blighe, Z.Sun, S.De, I.T. Mcgovern, B.Holland, M.Byrne, Y.K. Gun'Ko, J.J.Boland, P.Niraj, G.Duesberg, S. Krishnamurthy, R.Goodhue, J.Hutchison, V.Scardaci, A.C. Ferrari and J.N.Coleman.** 2008 йил, Nature Nanotechnol., Vol. 3, p. 563.

92. *Synthesis of high-quality graphene with a pre-determined number of layers.* **Z.Wu, W.Ren, L.Gao, B.Liu, C.Jiang and H.Cheng.** 2009 йил, Carbon, Vol. 47, p. 493.

93. *Microwave assisted exfoliation and reduction of graphite oxide for ultra-capacitors.* **Y.Zhu, S.Murali, M.D.Stroller, A.Velamakanni, R.D.Piner, R.S.Ruoff.** 2010 йил, Carbon, Vol. 47, p. 2118.

94. *Single graphene sheet detected in a carbon nanofilm.* **S.Horiuchi, T.Gotou, M.Fujiwara, T.Asaka, T.Yokosawa and Y.Matsui.** 2004 йил, Appl.Phys.Lett, Vol. 84, p. 2403.

95. *Synthesis and characterization of atomically thin graphite films on a silicon carbide substrate.* **E.Rollings, G.H.Gweon, S.Y.Zhou, B.S.Mun, J.L.McChesney, B.S.Hussain, A.V.Fedorov, P.N. First, W.A. de Heer, A. Lanzara.** 2006 йил, J.Phys.Chem.Solids, Vol. 67, p. 2172.

96. *Electronic Confinement and Coherence in Patterned Epitaxial Graphene.* **C.Berger, Z.Song, X.Li, X.Wu, N.Brown, C.Naud, D.Mayou, T.Li, J.Hass, A.N. Marchenkov, E. H.Conrad, P.N. First and W.A. de Heer.** 2006 йил, Science, Vol. 312, p. 5777.

97. *The Rise of Graphene.* **A.K.Geim, K.S.Novoselov.** 2007 йил, Nature Mat., Vol. 6, p. 183.

98. *Morphology of graphene thin film growth on SiC(0001).* **T.Ohta, F.E.Gabaly, A.Bostwick, J.L.McChesney, K.V.Emtsev, A.K.Schmid, T.Seyller, K.Horn and E.Rotenberg.** 2008 йил, New.J.Phys, Vol. 10, p. 023034.

99. *Homogenous large-area graphene growth on 6H-SiC (0001).* **C.Virojanadara, M.Syväjarvi, R.Yakimova, L.I.Johansson, A. A. Zakharov and T. Balasubramanian.** 2008 йил, Phys.Rev.B, Vol. 78, p. 245403.

100. *Towards wafer-size graphene layers by atmospheric pressure graphitization of silicon carbide.* **K.V.Emtsev, A.Bostwick, K.Horn, J.Jobst, G.L.Kellogg,L.Ley, J.L.McChesney, T.Ohta, S.A.Reshanov, J.Röhrl,E.Rotenberg, A.K.Schmid, D.Waldmann, H.B.Weber,T.Seyller.** 2009 йил, Nat.Mater, Vol. 8, p. 203.

101. *Ex-MWNTs: Graphene Sheets and Ribbons Produced by Lithium Intercalation and Exfoliation of Carbon Nanotubes.* **A.G.Cano-Márquez, F.J.Rodríguez-Macías, J.Campos-Delgado, C.G.Espinosa-González, F.Tristán-López, D.Ramírez-González, D.A.Cullen, D.J.Smith, M.Terrones and Y.I.Vega-Cantú.** 2009 йил, Nano.Lett, Vol. 9, p. 1527.

102. *Narrow graphene nanoribbons from carbon nanotubes.* **L.Jiao, L.Zhang, X.Wang, G.Diankov and H.Dai.** 2009 йил, Nature, Vol. 458, p. 877.

103. *Longitudinal unzipping of carbon nanotubes to form graphene nanoribbons.* **D.V.Kosynkin, A.L.Higginbotham, A.Sinitskii, J.R.Lomeda, A.Dimiev,B.K.Price and J.M.Tour.** 2009 йил, Nature, Vol. 458, p. 872.

104. **A.C.Jones, M.L.Hitchman.** *Chemical Vapor Deposition: Precursors, Processes and Applications.* Cambridge : Royal Soc.Chem, 2009.

105. **H.O.Pierson.** *Handbook of Chemical Vapor Deposition.* Park Ridge : Noyes Publications, 1992.

106. **A.Stansfield.** *The electric furnace: its construction, operation and uses.* s.l. : McGraw-Hill Book Company, inc, 1914.

107. *Effect of hydrogen attack on the strength of high purity copper.* **M.Z.Butt.** 1983 йил, J.Mater.Sci.Lett., Vol. 2, p. 1.

108. *A Novel Method of Etching Copper Oxide Using Acetic Acid.* **D.W.Hess, K.L.Chavez and.** 2001 йил, J.Electrochem.Soc, Vol. 148, p. G640.

109. *The Reduction of Copper Oxides by Molecular Hydrogen.* **Y.N.Z.Trehan.** 1962 йил, Z. Anorg. Allg. Chem., Vol. 318, p. 107.

110. *Large-Area Synthesis of High-Quality and Uniform Graphene Films on Copper Foils.* **X.Li, W.Cai, J.An, S.Kim, J.Nah, D.Yang, R.Piner, A.Velamakanni, I.Jung, E.Tutuc, S.K. Banerjee, L.Colombo and R.S Ruoff.** 2009 йил, Science, Vol. 324, p. 1312.

111. *Roll-to-roll production of 30-inch graphene films for transparent electrodes.* **S.Bae, H.Kim, Y.Lee, X.Xu, J.-S.Park, Y.Zheng, J.Balakrishnan, T.Lei, H.R.Kim, Y.I.Song, Y.-J.Kim, K.S.Kim,**

B.Özyilmaz, J.-H.Ahn, B.H.Hong and S.Iijima. 2010 йил, Nature Nanotechnology, Vol. 5, p. 574.

112. *Wafer-Scale Synthesis and Transfer of Graphene Films.* **Y.Lee, S.Bae, H.Jang, S.Jang, S.-E.Zhu, S.H.Sim, Y.I.Song, B.H.Hong and J.-H.Ahn.** 2010 йил, Nano Lett., Vol. 10, p. 490.

113. *Large area few-layer graphene/graphite films as transparent thin conducting electrodes.* **W.Cai, Y.Zhu, X.Li, R.D.Piner and R.S.Ruoff.** 2009 йил, Appl.Phys.Lett, Vol. 95, p. 123115.

114. *Graphene segregated on Ni surfaces and transferred to insulators.* **Q.Yu, J.Lian, S.Siriponglert, H.Li, Y.P.Chen, S.-S.Pei.** 2008 йил, Appl.Phys.Lett, Vol. 93, p. 113103.

115. *Large area, few-layer graphene films on arbitary substrates by chemical vapor deposition.* **A.Reina, X.Jia, J.Ho, D.Nezich, H.Son, V.Bulovic, M.S.Dresselhaus, J.Kong.** 2009 йил, Nano Lett., Vol. 9, p. 30.

116. *ASM Handbook : Alloy Phase Diagrams.* s.l. : ASM International, 2002. Vol. 3.

117. *Ultra-thin epitaxial films of graphite and hexagonal boron nitride on solid surfaces.* **C.Oshima, A.Nagashima.** 1997 йил, J.Phys.: Condens. Matter, Vol. 9, p. 1.

118. *The solubility of C in solid Cu.* **G.A.Lopez, E.J.Mittemeijer.** 2004 йил, Scr.Mater, Vol. 51, p. 1.

119. *Measurement Of The Electronic Density Of States Of Graphene Oxide Using Capacitive Photocurrent Spectroscopy.* **T.Bansal.** 2011 йил, PhD. Thesis.

120. *Raman Spectrum of Graphene and Graphene Layers.* **A.C.Ferrari, J.C.Meyer, V.Scardaci, M.Lazzeri, F.Mauri, S.Piscanec, D.Jiang, K.S.Novoselov,S.Roth, A.K.Geim.** 2006 йил, Phys.Rev.Lett., Vol. 97, p. 187401.

121. *Impact of the electron-electron correlation on phonon dispersions: failure of LDA and GGA functionals in graphene and graphite.* **M.Lazzeri, C.Attaccalite, L.Wirtz, F.Mauri.** 2008 йил, Phys.Rev.B, Vol. 78, p. 081406.

122. *Raman spectroscopy in graphene.* **L.M.Malard, M.A.Pimenta, G.Dresselhaus, M.S.Dresselhaus.** 2009 йил, Phys.Reports, Vol. 473, p. 51.

123. *Determination of LA and TO phonon dispersion relations of graphene near the Dirac point by double resonance Raman scattering.* **D.L.Mafra, G.Samsonidze, L.M.Malard, D.C.Elias, J.C.Brant, F.Plents, E.S.Alves, M.A.Pimenta.** 2007 йил, Phys.Rev.B, Vol. 76, p. 233407.

124. *Group-theory analysis of electrons and phonons in N-layer graphene systems.* **L. M. Malard, M. H. D. Guimarães, D. L. Mafra, M. S. C. Mazzoni, A. Jorio.** 2009 йил, Phys.Rev.B, Vol. 79, p. 125426.

125. *Observation of Raman band shifting with excitation wavelength for carbons and graphites.* **R.P. Vidano, D.B. Fischbach, L.J. Willis, T.M. Loehr.** 1981 йил, Solid State Commun., Vol. 39, p. 341.

126. *Highly uniform 300mm wafer-scale deposition of single and multilayered chemically derived graphene thin films.* **H.Yamaguchi, G.Eda, C.Mattevi,H.Kim, M.Chhowalla.** 2010, ACS Nano, Vol. 4, p. 524.

127. *Transfer of large-area graphene films for high-performance transparent conductive electrodes.* **X. Li, Y. Zhu, W. Cai, M. Borysiak, B. Han, D. Chen, R. D. PinerL.Colombo, R.S.Ruoff.** 2009, Nano Lett., Vol. 9, p. 4359.

128. *Novel Liquid Precursor-Based Facile Synthesis of Large-Area Continuous, Single, and Few-Layer Graphene Films.* **A.Srivastava, C.Galande,L.Ci, L.Song, C.Rai, D.Jariwala, K.F.Kelly, P.M.Ajayan.** 2010, Chem.Mater, Vol. 22, p. 3457.

129. *Nano PMMA and Copolymer-Data Sheet.* **MicroChem.**

130. *A direct transfer of layer-area graphene.* **W.Regan, N.Alem, B.Aleman, B.Geng, C.Girit, L.Maserati, F.Wang, M.Crommie, A.Zettl.** 2010, Appl.Phys.Lett, Vol. 96, p. 113102.

131. *Studies of copper etching in ferric chloride solutions.* **S.Habu, Y.Yoshihiro.** 1982, Ind.Eng.Chem.Process Des.Dev, Vol. 21, p. 511.

132. *Multiply Folded Graphene.* **K.Kim, Z.Lee, B.Malone, K.T.Chan, W.Regan, W.Gannett, B.Aleman, M.F.Crommie, M.L.Cohen, A.Zettl.** 24, 2011, Phys.Rev.B, Vol. 83, p. 245433.

133. *Graphene in plastic packages: A low cost construction method for resistive chemical sensors.* **S.Kona, C.K. Harnett.** 2012. MRS Proceedings. Vol. 1407.

134. **J.F.Watts, J.Wolstenholme.** *An introduction to surface analysis by XPS and AES.* West Sussex : John Wiley & Sons Ltd,, 2003.

135. **Laboratory, National Physical.** X-ray Photoelectron Spectroscopy. [Online] http://www.npl.co.uk/science-technology/surface-and-nanoanalysis/surface-and-nanoanalysis-basics/introduction-to-xps-x-ray-photoelectron-spectroscopy.

136. *Mylar and Teflon-AF as cell culture substrates for studying endothilial cell adhesion.* **C.C.Anamelechi, G.A.Truskey, W.M.Reichert.** 2005, Biomaterials, Vol. 26, pp. 6887-6896.

137. *Towards clean and crackless transfer of graphene.* **X.Liang, B.A.Sperling, I.Calizo, G.Cheng, C.A.Hacker, Q.Zhang, Y.Obeng, K.Yan, H.Peng, Q.Li, X.Zhu, H.Yuan, A.R.H.Walker, Z.Liu, L.-M.Peng, C.A.Richter.** 11, 2011, ACS Nano, Vol. 5, pp. 9144-9153.

138. **W.Kern.** Handbook of semiconductor wafer cleaning technology. Park Ridge, NJ : Noyes Publishing, 1993, chapter 1.

139. **National Instruments.** GPIB Instrument Control Tutorial. [Online] http://www.ni.com/white-paper/2761/en.

140. —. What is LabVIEW? *What is LabVIEW?* [Online] http://www.ni.com/labview/.

141. *Methanol.* **A.Vale.** 12, 2007 йил, Medicine, Vol. 35, pp. 633-634.

142. **Fisher Scientific.** *Ethanol, Absolute - Material Safety Data Sheet.*

143. *Molecular nanosensors based on the inter-sheet tunnelling effect of a bilayer graphene.* **F. Rao, Z. Fan, L. Dong, W.Li.** December 2010. IEEE 4th International Conference on Nano/Molecular Medicine and Engineering. pp. 172-175.

144. *A self-consistent theory for graphene transport.* **S.Adam, E.H.Hwang, M.Galitski, S.D.Sharma.** 47, 2007 йил, PNAS, Vol. 104, p. 18392.

145. *n-Type Behavior of Graphene Supported on Si/SiO2 Substrates.* **H.E.Romero, N.Shen, P.Joshi, H.R.Gutierrez, S.A.Tadigadapa, J.O.Sofo, P.C.Eklund.** 10, 2008 йил, ACS Nano, Vol. 2, pp. 2037-2044.

146. *Electrical transport and low-temperature scanning tunneling microscopy of microsoldered graphene.* **V.Geringer, D.Subramaniam, A.K.Michel, B.Szafranek, D.Schall, A.Georgi, T.Mashoff, D.Neumaier, M.Liebmann, M.Morgenstern.** 8, 2010 йил, Appl.Phys.Lett, Vol. 96, p. 082114.

147. *Evolution of Graphene Growth on Ni and Cu by Carbon Isotope Labeling.* **X.Li, W.Cai, L.Colombo, R.S.Ruoff.** 2009 йил, Nano Lett., Vol. 9, p. 4268.

148. *Carbon nanotube applicaitons in microelectronics.* **W.Hoenlein, F.Kreupl, G.S.Duesberg, A.P.Graham, M.Liebau, R.V.Seidel, E.Unger.** 2004, IEEE Trans.Comp.Packaging Technol., Vol. 27, p. 629.

149. *Epitaxial Graphene.* **W. A. de Heer, C. Berger, X. Wu, P. N. First, E. H. Conrad, X. Li, T. Li, M. Sprinkle, J. Hass, M. L. Sadowski, M. Potemski, G. Martinez.** 2007, Solid State Commun., Vol. 143, p. 92.

150. *Advances in the development and growth of functional nanomaterials:Toward the paradigm of materials by design.* **R.Seshadri, S.L.Brock, A.Ramirez, M.A.Subramanian, M.E.Thompson.** 2012, MRS Bulletin, Vol. 37, p. 682.

151. **R.Saito, G.Dresselhaus, M.S.Dresselhaus.** *Physical Properties of Carbon Nanotubes.* London : Imperial College Press, 1998.

152. *Trends in graphene research.* **M.Taghioskoui.** 10, 2009, Materials Today, Vol. 12, p. 34.

153. *Observation of higher-order infrared modes in solid C60 films.* **K.-A.Wang, A.M.Rao, P.C.Eklund, M.S.Dresselhaus, G.Dresselhaus.** 1993, Phys.Rev.B:Condens.Matter Mat.Phys., Vol. 48, p. 11375.

154. *Carbon nanotubes: Synthesis, integration, and properties.* **H.Dai.** 2002, Acc.Chem.Res, Vol. 35, p. 1035.

155. *Double Resonant Raman Scattering in Graphite.* **C.Thomsen, S.Reich.** 2000, Phys.Rev.Lett., Vol. 85, p. 5214.

156. *A review of chemical vapor deposition of graphene on copper.* **C.Mattevi, H.Kim, M.Chhowalla.** 2011 йил, J.Mater.Chem, Vol. 21, p. 3324.

157. **Perkin Elmer instruments.** *Technical Notes on Lock-in Amplifier.*

158. *Interpretation of certain characteristics in raman spectra of graphite and glassy carbon.* **A.V.Baranov, A.N.Bekhterev, Y.S.Bobovich, V.I.Petrov.** 1987, Opt.Spektrosk., Vol. 62, p. 1036.

159. *Electronic structure of atomically resolved carbon nanotubes.* **J.W.G.Wildoer, L.C.Venema,A.G.Rinzler, R.E.Smalley, C.Dekker.** 1, Nature, Vol. 391, pp. 59-62.

CURRICULUM VITAE

SILPA KONA

SUMMARY

Materials scientist with over 5 years of post-masters research experience in the area of chemical vapor sensors and chemical reactor control and design. Expertise in the chemical vapor deposition (CVD) synthesis of carbon based nanomaterials such as carbon nanotubes, graphene and carbon thin films

EDUCATION

Ph.D Electrical and Computer Engineering — August 2007-November 2012
University of Louisville, Louisville, KY
Advisor: Dr. Cindy K Harnett

M.S. Electrical and Computer Engineering — July 2007
University of Louisville, Louisville, KY
Advisors: Dr. Cindy K Harnett and Dr. Mahendra K. Sunkara

B. Tech Electrical and Electronics Engineering — May 2005
Jawaharlal Nehru Technological University, Hyderabad, India

ACCOMPLISHMENTS

- **Designed and fabricated** a low cost packaging method for graphene based resistive chemical sensors
- **Designed and assembled** an atmospheric pressure thermal CVD microscale reactor for the synthesis of carbon nanotubes and carbon thin films inside a micro capillary (700μm diameter) substrate
- **Designed and assembled** an RF plasma CVD microreactor for low temperature ($90^{O}C$) synthesis of carbon nanotubes inside micro capillary (150 through 700μm diameter) substrates at atmospheric pressure
- **Proposed a growth mechanism** for the morphology of diverging conical carbon nanotubes synthesized in a microreactor environment

RESEARCH EXPERIENCE

Graduate Research (PhD) — August 2007- Present

- Design and fabrication of low cost graphene based device for vapor sensing applications
- Experienced in chemical reactor control and design of a novel thermal CVD microreactor with computer control for the synthesis of carbon nanomaterials
- Synthesis of carbon thin films and carbon nanotubes via catalytic thermal CVD in microreactor environment

Graduate Research (MS) — August 2005 - August 2007

- Designed and assembled a complete microscale CVD reactor for the synthesis of nanomaterials
- Developed a microscale RF plasma CVD system for low temperature synthesis of nanomaterials
- Synthesized and studied the growth mechanisms of carbon nanotubes in a microscale reactor environment for both thermal and plasma CVD systems

Engineering Training (B.Tech) January 2005 - April 2005

- Electronic Corporation of India Limited (ECIL), Hyderabad, India
  Assisted in the design and training of an Instrumented Channel Monitoring System

WRITING EXPERIENCE

- A comprehensive Master's Thesis detailing the 'Synthesis of carbon nanotube arrays and diverging conical structures in a capillary microreactor'
- A detailed Doctoral dissertation on carbon nanomaterials as sensing elements, with emphasis on current techniques in construction of sensors, comparison and contrast of cost effectiveness and shortcomings of the designs and detailing a new and improved low cost construction method for graphene based vapor sensors
- Co-authored a book chapter 'Carbon Microtubes and Conical Carbon Nanotubes' published in Smart Materials, CRC Press/Taylor and Francis Group, 2008

TEACHING EXPERIENCE

- Assisted the department of Electrical and Computer Engineering grading the course "Introduction to Electrical Engineering"
  August 2005 - August 2006
- Math tutor in Resources for Academic Achievement (REACH), University of Louisville, to high school students September 2007- November 2007

PEER REVIEWED PUBLICATIONS AND BOOK CHAPTERS

- **S.Kona**, C.K.Harnett, A review paper on current techniques and trends in Graphene based applications, December 2012, Review Manuscript in preparation
- **S.Kona**, C.K.Harnett, "Carbon nanomaterial based vapor sensors", November 2012, Manuscript in preparation
- **S.Kona**, C.K. Harnett, "Graphene in plastic packages: A low cost construction method for resistive chemical sensors", 2012, MRS Proceedings, Vol. 1407, mrsf11-1407-aa20-29
- **S.Kona,** J.H.Kim, C.K.Harnett, M.K.Sunkara, "Carbon Nanotube Growth Studies Using an Atmospheric, Microplasma Reactor", 2009, IEEE Trans. on nanotechnology, Vol.8, Issue 3, Page 286
- S.Dumpala, G.Bhimarasetti, S.Gubbala, P.Meduri, **S.Kona** and M.K.Sunkara, "Carbon Microtubes and Conical Carbon Nanotubes", 2008, Smart Materials edited by Mel Schwartz CRC Press/Taylor & Francis Group, Chapter 22, Page 22-1

CONFERENCE PRESENTATIONS

ORAL :

- "Graphene on plastic : A low cost substrate for vapor sensors", May 2012, 17th Annual KY EPSCoR, Lexington, KY **(Invited Talk)**
- "A low cost construction method for graphene based resistive chemical sensors", March 2012, American Physical Society (APS), Boston MA
- "In-situ growth of carbon nanotubes in microreactor environment", March 2010, American Physical Society (APS), Portland, OR
- "Catalyst Aided Nanomaterial Growth in Microreactor Chamber Under Extreme Conditions", October 2008, First Annual Nanotechnology Symposium, Sullivan University College of Pharmacy, Louisville, KY
- "Catalyst Aided Nanomaterial Growth in Microreactor Chamber Under Extreme Conditions", November 2007, American Institute of Chemical Engineers (AIChE) annual meeting, Salt Lake City, UT

POSTER :

- "Graphene on plastic : A low cost substrate for vapor sensors", May 2012, 17th Annual KY EPSCoR, Lexington, KY

- "Graphene in plastic packages: A low cost construction method for resistive chemical sensors", November 2011, Materials Research Society (MRS) , Boston, MA
- "Synthesis of CNT Arrays at Temperatures Below 90°C Using Microplasma Reactor", March 2008, KYNanoMat, Louisville, KY

EQUIPMENT / INSTRUMENTS / TECHNIQUES/APPLICATION SOFTWARE

Chemical Vapor Deposition (CVD) in micro-scale environment, Horizontal Tube Furnace Chemical Vapor Deposition, RF Plasma Enhanced Chemical Vapor Deposition (PECVD), Scanning Electron Microscopy (SEM), X-Ray Diffractometer (XRD), Energy Dispersive X-ray Spectroscopy (EDX), X-ray Photoelectron Spectroscopy (XPS), Raman and UV-Vis Spectroscopy, 2 point and 4 point probe measurement techniques. Softwares: Igor, LabView, Fortran, P-Spice, L-Edit, Photoshop, PeakFit

AFFILIATIONS / AWARDS

- Materials Research Society (MRS), American Physical Society (APS)
- Doctoral Dissertation Completion Award (May 2012– August 2012)
- Graduate Student Assistant Award (August 2005 – August 2006)
- Graduate Research Assistantship (September 2006 – August 2007)
- Grosscurth Fellowship, University of Louisville (August 2007 – August 2009)
- First Prize, InfoQuest, National Level Technical Symposium, Hyderabad, India (2004)